DISSERTATION

Spectrally Flexible Opto-Electronic Terahertz Light

eingereicht von

Dominik THEINER

an der Technischen Universität Wien
Fakultät für Elektrotechnik und Informationstechnik

zum Zwecke der Erlangung des akademischen Grades
eines Doktors der Naturwissenschaften

unter der Anleitung von

Univ.Prof. Mag.rer.nat. Dr.rer.nat. Karl UNTERRAINER
und Univ.Ass. Dipl.-Ing. Dr.techn. Juraj Darmo

Wien, September 2023

Gutachter:

Dr. Martin Hofmann, Professor, Ruhr-Universität Bochum

Dr. Oliver H. Heckl, Associate Professor, Universität Wien

Abstract

The terahertz (THz) region is a part of the electromagnetic spectrum with increasing scientific interest due to the recent progress in the development of terahertz sources, detectors and modulators and its potential applications are vast. Examples of these include spectroscopy and imaging, both of which are used to gain increased knowledge and understanding of the world around us. Especially in times of climate change and consequently changed environmental influences to the human body, the terahertz domain may provide an important insight due to the huge amount of molecular fingerprints coming from rotational transitions, which lie in this spectral region and are relevant for environmental monitoring and medical diagnostics. Any application comes with its unique set of requirements regarding the brightness, tunability, linewidth and frequency spectrum of the light source to reach different goals. There are various possibilities to generate terahertz radiation including resonant tunneling diodes, optically pumped gas lasers and quantum cascade lasers. Most of them struggle when it comes to precise frequency tunability and partially require cryogenic cooling. In this sense, the approaches based on difference frequency generation (or photomixing) offer a suitable solution for tunable room-temperature terahertz sources. Nonetheless, all of them fail when it comes to on-demand spectral synthesis.

The main effort of this work is the development of a terahertz source with great flexibility to meet various application relevant requirements, all with a single tunable system. This goal is achieved by the combination of two mature technologies. Photomixers are convenient room-temperature terahertz sources, which generate light at the difference frequency of two near-infrared lasers driving the mixer with their optical beating. Thereby, they enable broad frequency tunability via the simple adjustment of one of the driving lasers wavelength. Additional, the telecommunication field offers efficient modulators in the near-infrared. When a phase or intensity modulation is applied to a carrier frequency, optical sidebands are generated on both sides of the carrier with a frequency spacing defined by the RF signal used to drive the modulators. In this sense, a huge spectral flexibility can be achieved, which is utilized in the terahertz domain by implementing them on the driving lasers of the photomixers.

When it comes to spectroscopy, the optical frequency comb has left an indelible mark in the last decades. A frequency comb is a spectrum of phase-coherent, equally spaced, narrow lines that act as a precise ruler in the frequency domain, and thus, providing excellent accuracy. Generating combs in the terahertz range is still quite challenging, and the most common

approaches all rely on an optical cavity that defines a frequency grid to which the comb teeth are restricted. Consequently, hardware modifications are necessary to alter the spectral content of these combs. In this thesis, an alternate approach is successfully introduced by applying the photomixing principle, for the efficient down-conversion to the terahertz domain, to electro-optic frequency combs, which provide electronic control of the comb spectral content in the near-infrared. This terahertz opto-electronic frequency comb light source comes with huge flexibility regarding the number of comb lines - reaching up to 40 teeth, their spacing - adjustable beyond 20 GHz, and its position within the terahertz window - tunable over 3.5 THz. Moreover, its comb teeth linewidth is found to be below 10 MHz and its spectral brightness on the microwatt range, which are suitable parameters for chemical sensing under ambient conditions, which is demonstrated by the measurement of an absorption line of ammonia (NH_3).

Furthermore, a highly versatile platform for molecular gas sensing in the terahertz range is developed by combining this spectrally adaptable light source with a novel generation of miniaturized gas cells based on the latest waveguide technology. The so-called substrate-integrated hollow waveguide (iHWG) consists of a solid substrate with integrated reflective light-guiding channel that provides large design flexibility of the optical channel, thus enabling extended optical path lengths which increase the sensitivity of gas sensors while maintaining a robust and compact device. These waveguides have already proven their potential for advanced gas sensing in the mid-infrared and in the ultraviolet regions. Here, their first implementation in a terahertz system is demonstrated. The frequency agile light source enables an optical sideband tuning method that substantially exceeds a standard wavelength tuning method in terms of speed and accuracy, which is testified by the measurement of several rotational transitions of the crucial greenhouse gas nitrous oxide (N_2O) with an estimated detection limit of $\sim$600 nanomol.

Kurzfassung

Der Terahertzbereich (THz) ist ein Teil des elektromagnetischen Spektrums, der aufgrund der jüngsten Fortschritte bei der Entwicklung von Terahertz-Quellen, -Detektoren und -Modulatoren von zunehmendem wissenschaftlichem Interesse ist und dessen Anwendungsmöglichkeiten enorm sind. Beispiele hierfür sind die Spektroskopie und die Bildgebung, die beide dazu dienen, die Welt um uns herum besser kennen und verstehen zu lernen. Insbesondere in Zeiten des Klimawandels und der damit einhergehenden veränderten Umwelteinflüsse auf den menschlichen Körper kann der Terahertz-Bereich wichtige Erkenntnisse liefern, da in diesem Spektralbereich eine große Anzahl molekularer Fingerabdrücke, aus Rotationsübergängen bestehend, zu finden sind, die für die Umweltüberwachung und die medizinische Diagnostik von Bedeutung sind. Jede Anwendung stellt ihre eigenen Anforderungen an die Helligkeit, die Durchstimmbarkeit, die Linienbreite und das Frequenzspektrum der Lichtquelle, um unterschiedliche Ziele zu erreichen. Es gibt verschiedene Möglichkeiten Terahertzstrahlung zu erzeugen, darunter sind resonante Tunneldioden, optisch gepumpte Gaslaser und Quantenkaskadenlaser. Die meisten von ihnen haben Probleme mit der präzisen Frequenz Durchstimmbarkeit und erfordern teilweise kryogene Kühlung. In diesem Sinne bieten die auf Differenzfrequenzerzeugung (oder Photomischung) basierenden Ansätze eine geeignete Lösung für durchstimmbare Terahertz-Quellen bei Raumtemperatur. Allerdings versagen sie alle, wenn es um zielgerichtete Spektralsynthese geht.

Das Ziel dieser Arbeit ist die Entwicklung einer Terahertz-Quelle mit großer Flexibilität, um verschiedene anwendungsrelevante Anforderungen zu erfüllen, und das alles mit einem einzigen durchstimmbaren System. Dieses wird durch die Kombination von zwei ausgereiften Technologien erreicht. Photomischer repräsentieren bequeme Terahertz-Quellen, die bei Raumtemperaturen funktionieren. Sie erzeugen Licht mit der Differenzfrequenz zweier Nahinfrarot-Laser, die den Photomischer mit ihrem optischen Interferenzsignal antreiben. Dadurch ermöglichen sie eine breite Frequenz Durchstimmbarkeit, da die Wellenlänge eines der treibenden Laser relativ einfach angepasst werden kann. Darüber hinaus bietet der Telekommunikationsbereich effiziente Modulatoren im nahen Infrarot. Wenn eine Phasen- oder Intensitätsmodulation auf eine Trägerfrequenz angewendet wird, werden auf beiden Seiten des Trägers optische Seitenbänder erzeugt, deren Frequenzabstand durch das zur Ansteuerung der Modulatoren verwendete HF-Signal definiert ist. Auf diese Weise wird eine enorme spektrale Flexibilität erreicht, die im Terahertz-Bereich genutzt werden kann, indem solche Modulatoren als Teil der

Treiberlaser für die Photomischer implementiert werden.

Dem Gebiet der Spektroskopie hat der optische Frequenzkamm in den letzten Jahrzehnten deutlich seinen Stempel aufgedrückt. Ein Frequenzkamm ist ein Spektrum aus phasenkohärenten, gleichmäßig verteilten, schmalen Linien, die als präzises Lineal im Frequenzbereich fungieren und somit eine ausgezeichnete Genauigkeit bieten. Die Erzeugung von Kämmen im Terahertzbereich ist nach wie vor recht schwierig, und die gängigsten Ansätze beruhen alle auf einem optischen Resonator, der einen Satz an Frequenzen vordefiniert, auf den die Kammzähne beschränkt sind. Folglich sind physische Modifikationen an diesen Resonatoren erforderlich, um die spektrale Form dieser Kämme zu verändern. In dieser Arbeit wird ein alternativer Ansatz erfolgreich vorgestellt, indem das Prinzip der Photomischung für die effiziente Abwärtskonvertierung in den Terahertz-Bereich auf elektro-optische Frequenzkämme im nahen Infrarot angewandt wird, deren spektrale Form sich elektronisch kontrollieren lässt. Diese opto-elektronische Terahertz-Frequenzkamm-Lichtquelle bietet eine enorme Flexibilität in Bezug auf die Anzahl der Kammlinien - bis zu 40 Zähne -, ihren Abstand - einstellbar über 20 GHz - und ihre Position innerhalb des Terahertzbereichs - durchstimmbar über 3,5 THz. Darüber hinaus ist die Kammzahn-Linienbreite schmäler als 10 MHz und die spektrale Helligkeit im Mikrowatt-Bereich. Dies sind geeignete Parameter für chemische Messungen unter Umgebungsbedingungen, wie die Messung einer Absorptionslinie von Ammoniak (NH_3) zeigt.

Darüber hinaus wird durch die Kombination dieser spektral verstellbaren Lichtquelle mit einer neuen Generation von miniaturisierten Gaszellen, die auf der neuesten Wellenleitertechnologie basieren, eine äußerst vielseitige Plattform für die molekulare Gassensorik im Terahertzbereich entwickelt. Der so genannte substratintegrierte Hohlwellenleiter (iHWG) besteht aus einem massiven Substrat mit integriertem reflektierendem Lichtleitkanal, der eine große Flexibilität bei der Gestaltung des optischen Kanals bietet und so größere optische Weglängen ermöglicht, die die Empfindlichkeit der Gassensoren erhöhen und gleichzeitig ein robustes und kompaktes Mess-Instrument darstellen. Diese Wellenleiter haben bereits ihr Potenzial für die fortschrittliche Gassensorik im mittleren Infrarot und im Ultraviolettbereich unter Beweis gestellt. Hier wird ihre erste Umsetzung in einem Terahertz-System demonstriert. Die frequenzagile Lichtquelle ermöglicht eine optische Seitenband-Durchstimmmethode, die eine klassische Wellenlängen-Durchstimmmethode in Bezug auf Geschwindigkeit und Genauigkeit deutlich übertrifft, was durch die Messung mehrerer Rotationsübergänge des wichtigen Treibhausgases Distickstoffoxid (N_2O) belegt wird. Eine beachtliche Nachweisgrenze von $\sim$600 nanomol N_2O kann für das bestehende System in Aussicht gestellt werden.

Contents

1 Introduction

Hertz (Hz) is the unit of frequency describing one cycle per second, expressed in SI base units 1 Hz equals 1 s^{-1}. It is named after Heinrich Rudolf Hertz who first demonstrated the existence of electromagnetic waves. The terahertz (THz) region describes a part of the electromagnetic spectrum with boundaries varying in literature extending from 0.1 THz to 30 THz [1]. It lies a few orders of magnitude below visible light (∼400-790 THz) and in-between the microwave and the infrared spectral regime. It is equivalent to wavelengths ranging from 3 mm to 0.001 mm, corresponding to wavenumbers between 3.33 cm^{-1} and 1000 cm^{-1} and possesses photon energies in the range of 0.41 meV to 124 meV. According to its wavelength range, terahertz radiation is often referred to as sub-millimeter radiation and due to its overlap with the infrared region on the high frequency side it is also partially called the far infrared. It offers quite unique properties relevant for a wide range of potential applications. In terms of imaging, terahertz light provides (sub-)mm resolution, and thus, surpasses microwave systems due to its shorter wavelengths. Furthermore, many materials that are opaque in the visible range - such as clothing, plastics or paper - become transparent for terahertz waves, which can be utilized for revealing hidden objects. Additionally, chemical fingerprints consisting of molecular rotational transitions are also located in this frequency domain, enabling the combination of imaging with chemical composition analysis. Another advantage is the low photon energy that comes with a non-invasive character. All these properties collectively make terahertz radiation equally interesting for medicine, biology, industry, security and numerous other fields.

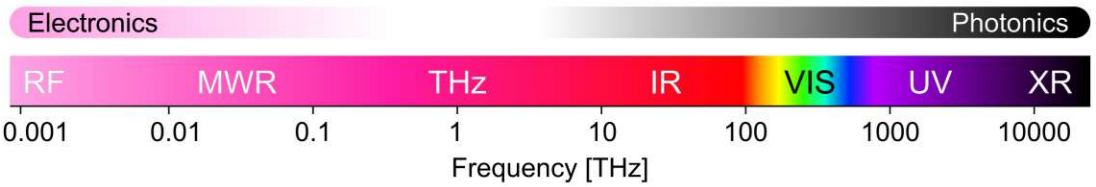

Figure 1.1: Located between microwaves and infrared light lies the terahertz spectral range. Electronic and photonic applications do not fully cover that part of the spectrum yet, which framed the name "THz gap".

The prefix tera (T) in terahertz stands for a multiplication by 10^{12}. Dealing with high frequencies of 10^{12} Hz is quite challenging for electronic devices coming from the microwave

technology side. Photonic technologies are efficient in generating high frequency radiation, however, the standard concepts rely on electron-hole recombinations in semiconductors that reach physical limitations at low energies such as those of terahertz photons. Since photonics and electronics failed so far to provide efficient generation and detection techniques in the terahertz domain, that part of the electromagnetic spectrum has been termed the 'Terahertz Gap'. Figure 1.1 shows the location of the terahertz region within the electromagnetic spectrum and depicts the corresponding gap that exists between electronics and photonics. The technological progress in this field has increasingly diminished the terahertz gap in recent years. There are various approaches, based on different techniques, that are used to generate and detect terahertz light. Nevertheless, the search for reliable and flexible sources as well as fast and sensitive detectors is still ongoing.

Many state-of-the-art terahertz sources suffer from several drawbacks, such as bulky and expensive devices, limited frequency tunability, or come with the need for cryogenic cooling. Furthermore, none of the currently available systems offer the possibility for precise on-demand spectral synthesis suitable for high quality terahertz generation that is adjustable to various application dependent requirements.

1.1 Outline

The major focus of this thesis is the development of a spectrally highly flexible terahertz source built with state-of-the-art technologies. Terahertz generation based on photomixing is among the most promising solutions for real-world applications in terms of room-temperature operation, tunability and straight-forward handling. It relies on difference frequency generation of two near-infrared lasers in an ultrafast opto-electronic device and presents a mature technique already utilized in commercially available single-colour systems. When it comes to spectral synthesis, electro-optic modulation offers significant flexibility through the generation of optical sidebands, however, achieving this modulation in the terahertz is highly challenging. On the other hand, in telecommunication systems, such modulators have become essential components, driving their development in the near-infrared in the last decades. The primary objective of this work is the combination of these two mature technologies, namely photomixing and electro-optic modulation, with the aim to effectively exploit this modulation technique in the terahertz domain. The goal is to demonstrate its impact onto the flexible generation of terahertz frequency combs and the development of a versatile molecular gas sensing platform.

The thesis is structured as follows: Chapter 2 presents the current status quo of terahertz

technologies and introduces its main application fields. In chapter 3, the fundamental principles for the understanding of this work are explained. This includes photomixing devices as terahertz sources, rectangular metallic hollow waveguides that can be used as miniaturized gas cells and the theory of vibrational-rotational transitions in molecules to demonstrate the sensing possibilities in the terahertz range. A rigorous discussion of optical frequency combs is given in chapter 4 focusing onto the principles based on electro-optic modulation, essential for the development of an opto-electronic light source with large flexibility, which is shown in chapter 5. The presentation of this novel terahertz source includes the analysis of its key parameters - brightness and linewidth - and the exploration of the available parametric space for the generation of terahertz frequency combs. Chapter 6 establishes a versatile molecular gas sensing platform that combines the spectrally flexible terahertz source with the latest waveguide technology. Robust substrate-integrated hollow waveguides resolve the major drawbacks of conventional gas cells, such as demanding fabrication, bulkiness and susceptibility to mechanical vibrations and temperature drifts. Finally, first measurements of molecules in gas phase demonstrate the potential of this system for precise spectroscopic applications relying on well-defined small probing volumes and fast measurement times.

2 Terahertz Technologies - State of the Art

This chapter introduces the most promising application fields for terahertz technologies and provides an overview of the current state-of-the-art of available terahertz emitters and detectors.

2.1 Terahertz Applications

With the continuous development of THz sources and detectors, the attention given to THz applications has increased in recent years, slowly catching up in numbers of real-world technologies compared to its neighboring frequency domains. The potential of THz radiation opens completely new possibilities in a wide range of application fields.

2.1.1 Spectroscopy and Sensing

THz radiation is a unique tool for studying physical and chemical phenomena. Its photon energies lie in the proper range for probing and manipulating different states of matter via the interaction with low-energy excitations, charge carrier dynamics in electronic materials, or rotational and vibrational transitions in molecules for chemical fingerprinting. There is a wide range of spectroscopic and sensing techniques suited for a variety of applications.

Fourier transform infrared (FTIR) spectroscopy is a widely used method with successful applications in both laboratory and industrial settings. These systems are commercially available and can measure optical properties from the near-infrared to the terahertz. In the standard configuration, FTIRs consist of a Michelson interferometer, a broadband source, a sample under investigation, and a broadband detector. The movable mirror in one of the two interferometer arms is scanned to measure an interferogram, which is then Fourier transformed to obtain the corresponding frequency spectrum. Compared with a reference measurement, this spectrum can be used to investigate the transmittance and reflectance of the sample, shining light onto its optical properties. One limitation of FTIR spectrometers is the associated noise generated by the moving arm of the interferometer. Nevertheless, FTIRs are instruments with high accuracy that are used for precision metrology [2, 3].

When the radiation source delivers a frequency comb, the signal-to-noise ratio of FTIR spectrometers can be enhanced significantly [4]. Frequency combs, with their precision and

accuracy, serve as ruler in the frequency domain, making them ideal sources for spectroscopy [5]. An in-depth discussion of frequency combs is presented in chapter 4 since they play a key role in this work. A powerful alternative spectroscopic technique based on frequency combs is dual comb spectroscopy, which offers high resolution measurements at a faster rate and does not require any moving parts [6–8]. The method is based on two interfering, slightly detuned combs on a fast detector, giving rise to an RF comb composed of distinguishable heterodyne beats between pairs of comb teeth. This RF comb contains the relevant spectral information of the original comb spectra, enabling the sample's response to be encoded onto the comb light and subsequently recovered through heterodyne detection. Essential for this method is the mutual coherence of both combs, which can be significantly increased when both combs originate from a single laser cavity, and thus, share their noise characteristics [9].

Another famous spectroscopic technique in the terahertz range represents time domain spectroscopy (TDS) [10]. A TDS system is based on the generation and detection of broadband THz pulses with femtosecond optical laser pulses. The optical pulse is divided into two distinct pulses; the first pulse is used to create a broadband THz pulse (e.g. via a photoconductive antenna), while the second probe pulse is used for the coherent detection of the propagating THz pulse. With the help of a variable time delay between the short optical and the longer THz pulse, the time-resolved THz electric field, consisting of amplitude and phase information (i.e. the THz pulse waveform), can be recorded. The complex frequency dependent refractive index of a sample inserted into the THz beam path can be studied by the comparison of the waveform with and without sample. TDS provides high-resolution measurements of the THz amplitudes and phases, due to the coherent detection technique that eliminates the interference from incoherent radiation including ambient light or room temperature blackbody radiation. Such systems are used to investigate carrier dynamics in semiconductors [11], the optical gain in THz quantum cascade lasers [12], nonlinear effects [13] and molecular absorption features of gases, liquids and solids [14]. Standard TDS systems are rather bulky and expensive due to the femtosecond laser source, but there are configurations aiming to replace them with convenient photomixer sources [15,16].

Molecular absorption lines can also be analyzed with a tunable narrowband THz source. The source emits THz radiation that is transmitted through a sample and recorded by a detector. By tuning the emission frequency, the shape of the absorption feature can be measured. This high-resolution spectroscopic approach has been realized utilizing different kinds of THz sources. When a THz source struggle to provide sufficient tunability in a certain frequency range, laser sideband spectroscopy can be applied. It relies on the mixing of the radiation of

a fixed THz laser with a tunable microwave source, which generates sidebands that can be tuned through an absorption region [17]. A similar technique can be realized with difference frequency generation, where the optical beating of two lasers, operated with an frequency offset lying in the terahertz range, gives rise to an electromagnetic wave with the difference frequency of the original light sources. The desired frequency tunability for spectroscopy is contributed by one of the two mixing lasers operating in a spectral domain, such as the infrared or the visible range, where many wavelength tunable devices are available [18,19].

Heterodyne spectrometers for remote sensing applications also rely on a mixing process, although utilized at the detection side. A tunable THz source is used as local oscillator, which is combined with the signal to be measured at a mixer element. This transfers the THz spectrum to the GHz range, centered at the intermediate frequency, thereby making it more easily accessible to electronic measurement equipment. This high resolution technique is widely used in astronomical and atmospheric investigations for the identification of molecules, the exploration of chemical compositions, the evolution and the dynamical behavior of star forming regions and molecular clouds, and general processes in interstellar medium. Famous examples of THz heterodyne spectrometers include the receiver on the Aura satellite that observes atmospheric constituents such as HCl, ClO and OH [20], the HIFI system on the Herschel space observatory investigating planetary atmospheres, galactic and extra-galactic objects [21] and the GREAT instrument on SOFIA for studying the fine-structure lines of ionized nitrogen, carbon and oxygen [22].

2.1.2 Wireless Communication

In recent years, the use of wireless data has seen a dramatic increase, mainly due to the popularity of services such as interactive gaming and video streaming, as well as the availability of faster wireless transmission rates. This trend is projected to continue, necessitating even higher rates to meet the demands of more advanced and data-intensive future applications. The currently most widely used 2.4 and 5 GHz frequency bands as well as today's 5G standard above 24 GHz are not suited for such tasks, since they are bandwidth limited with transmission rates up to 20 Gbit/s due to the allocation in the electromagnetic spectrum, which covers already all frequency bands up to 300 GHz [23].

The development of the next generation 6G wireless systems faces the challenges of fast, energy-efficient, ultra-reliable communication with minimal latency to enable technologies using the Internet of Everything (IoE) that connects millions of people and billions of devices. IoE services might include augmented/mixed/virtual reality systems, brain-computer inter-

faces, autonomous driving, connected robotics, digital twins, holographic radio, to name just a few [24]. The essential movement to higher frequencies comes with the drawback of increased free-space path loss and the added difficulty of water absorption lines [25]. Using the existing optical fiber communication infrastructure might prevent the necessity of long range wireless transmission. The current systems operate in the near-infrared and show the ability to achieve high transmission rates up to 1 Tbit/s over long distances [26]. Thus, high-speed wireless links to optical fiber hubs are of particular interest for bridging the last meters to the user. Besides offering high-rate transmission, THz bands have the potential to support the development of joint sensing and communication systems. All communication blockages represent sensing opportunities, and vice versa, which brings the advantage of mutual feedback to achieve joint objectives [27].

2.1.3 Terahertz Imaging

Terahertz radiation offers several advantageous properties that are especially beneficial for a huge amount of imaging applications [28]. A small part of the background radiation lies in the THz range and is used for passive imaging in astronomy [29]. For most other applications the amount of THz light in the background radiation is not sufficient, nevertheless there are examples of research and commercial applications as well [30, 31]. Other imaging methods require the use of dedicated emitters to illuminate the object and record its reflection or transmission.

In general, THz waves provide superior spatial resolution than imaging methods based on lower frequencies like microwaves, due to their shorter wavelengths. At higher frequencies, such as infrared radiation, materials including paper, cardboard, plastic, and clothing are often opaque, whereas, THz light has the unique ability to penetrate through these materials. Combined with its non-ionizing nature, due to its corresponding low photon energies, it is useful for non-destructive testing and screening in various industrial, security and medical applications. The practical use of its non-invasive character can be shown by many examples [32]. To name just a few specific applications, it is utilized in the investigation of artwork, historical artifacts and architectural buildings [33–35], the study of polymers and ceramics in the plastics industry [36], the detection of defects in insulating panels used by the NASA [37], the thickness measurements of automotive paint [38] and the quality control of packaged integrated circuits [39]. Contrary to the transparency of packaging and clothing materials, metallic objects are highly reflective in the THz domain, providing a beneficial combination for security applications such as body scanners at airports to reveal hidden weapons [40, 41]. Moreover, the

combination of imaging with spectroscopy has an additional advantage, as many molecules exhibit chemical fingerprints in the THz range. Thus, not only metallic objects can be detected, but also forbidden substances like explosives or drugs can be found and identified [42, 43].

THz radiation experiences high attenuation by water, which is challenging for communication and other setups in environments with ambient air. However, this property is beneficial for medical and biological tasks, as it allows for the detection of small differences in hydration, which enables in vivo and ex vivo studies of human tissue. Medical applications include the investigation of blood disorders, diabetes, breathing conditions, skin burn, different types of cancer, corneal diseases, caries in teeth and many more [44–46]. The quality control both in agricultural and in food industries benefits from THz imaging of biological samples as well [47, 48].

2.2 Generating Terahertz Light

All of the discussed applications depend on a matching light source full-filling specific application dependent requirements regarding the emission wavelength, the brightness, the frequency tunability, etc. There are various approaches for generating terahertz light.

2.2.1 Thermal Sources

The thermal emission of any object can be described as black-body radiation in first approximation. Its characteristic continuous frequency spectrum is solely defined by its temperature according to Planck's law. The most famous black-body in nature is the sun and terahertz light can already be detected as part of the cosmic background radiation [49]. A technical application of this principle is found in the Globar, a cylindrical rod of silicon carbide that is electrically heated to temperatures of 1350-1500 K [50]. Its broadband, incoherent emission has a peak in the mid-infrared and a weak tail reaching into the terahertz regime. Globars are commonly used as light source in far-infrared spectrometers.

Another thermal source for terahertz light represents the emission from the hot gas plasma in a mercury lamp that can produce useful intensities in the terahertz [51]. The radiation is a combination of the mercury arc itself operating at $\sim$5000 K and the quartz envelope that reaches $\sim$1000 K. The terahertz emission is equal or even superior compared to that of a Globar. However, the relatively uniform output spectrum of the Globar is more beneficial for spectroscopic applications.

2.2.2 Vacuum Electronic Sources

Vacuum electronic devices are among the most powerful sources for terahertz radiation covering a broad spectral range [52]. All of them rely on electron beams propagating through a vacuum environment under well controlled conditions. Thereby, a modulating signal interacts with the electron beam converting the kinetic energy of the electrons into electromagnetic field energy. The trade-off of such sources is usually the high requirements in form of bulky devices, vacuum-tight enclosures, or strong magnetic fields for electron beam control and confinement.

Traveling-wave tubes (TWTs) were developed for the power amplification of RF frequencies. The electromagnetic waves travel parallel to the electron beam that provides the energy for the amplification, which requires the phase velocity of the RF signal and the speed of the electrons to be similar. This is achieved by a metal grating serving as slow-wave structure that can be specially designed to introduce a feedback mechanism resulting in an oscillating system and resembles the basic principle of backward wave oscillators (BWOs) [53]. BWOs exhibit a broad wavelength tuning range and are simply controlled by the voltage of the electron gun defining the speed of the electrons. They reach frequencies up to $\sim$1.3 THz with power levels of milliwatts above 1 THz and watts at 100 GHz [52]. Their broad, continuous frequency coverage and large output powers make them particularly suited for molecular spectroscopy and especially allow to capture broad absorption features typically occurring in solid-state systems [54].

When the electron beam reaches relativistic velocities, synchrotron radiation can be generated accelerating the electrons vertical to their movement [55]. Bunches of electrons moving together emit coherent radiation in phase with high intensities [56]. Such sources provide stable and collimated radiation ranging from terahertz to ultraviolet in form of short pulses corresponding to broad frequency spectra.

The principle of synchrotron radiation is also the basis for the functioning of free electron lasers (FELs) [57]. A periodic transverse magnetic field is generated by an arrangement of magnets in a so-called undulator, which forces the electrons into oscillation. An optical cavity collects the emitted photons and enables coherent emission. FELs are tunable over a broad range of frequencies ranging from microwaves to x-rays [58] due to their strong wavelength dependence on the electron energy. They offer very high output powers scaling linearly with the number of involved electrons.

2.2.3 Solid State Electronic Sources

Another attempt to realize terahertz sources comes from microwave technologies. High speed electronics keep adapting their concepts to push their frequency limits towards the terahertz regime. The transit time and RC time constants of these devices often limits the maximum operating frequencies to the sub-terahertz with power levels dramatically decreasing with increasing frequencies.

III-V-based materials outperform the standard Si-based complementary metal-oxide-semiconductor (CMOS) technology in terms of high electron mobility due to lower effective electron mass values. This led to InP- and GaN-based high electron mobility transistors (HEMTs) and heterojunction bipolar transistors (HBTs) with oscillation frequencies around 1 THz [59–61].

Sources based on high power driven multiplier chains (mostly frequency doublers and triplers) are also extending the microwave field towards the terahertz range. There, the high harmonic generation relies typically on the non-linearity of GaAs Schottky barrier diodes. In spite of low conversion efficiencies, room temperature systems based on two or three cascaded frequency triplers are reported with more than 1 mW output power at 0.9 THz [62] and operation up to 2.75 THz delivering still over 1 µW [63]. Spectrometers based on multiplier-chains were the first to be used in the terahertz domain [64].

Resonant tunneling diodes (RTDs) pave another way to the terahertz domain. RTDs feature a so-called negative differential resistance (NDR) region, where an increase of the driving voltage leads to a decrease in current. This effect enables terahertz frequency oscillators to achieve frequencies close to 2 THz [65] and provides output power levels of 0.7 mW in an array configuration [66]. Other potential terahertz sources based on the NDR effect include Gunn diodes [67], impact ionization avalanche transit-time (IMPATT) diodes [68] and tunnel-injection transit-time (TUNNETT) diodes [69].

2.2.4 Terahertz Lasers

Photonic technologies rely on radiative transitions between electronic states to generate light. Adapting these concepts for terahertz generation proved to be difficult due to the low THz photon energies comparable to the thermal background. Thus, it is challenging to maintain the population inversion between the closely spaced electronic states essential for the terahertz optical transition.

For many years optically pumped gas lasers have been the state of the art solution for coherent CW terahertz generation. Almost any transition between rotational states of molecules

with permanent electrical dipoles can be utilized, thus a broad frequency range is covered. However, the dependence on distinct transition lines prevents a continuous tunability [70]. The gas molecules are optically excited traditionally by a bulky CO_2 pump laser, although nowadays there are more compact alternatives including harmonic generators or quantum cascade lasers [71]. Gas lasers cover frequencies from 0.1 to 8 THz with output powers up to several 100 mW.

Stimulated emission in the terahertz range is also achieved in p-doped bulk germanium with crossed electric and magnetic fields enabling a population inversion between light-hole and heavy-hole subbands [72]. Such lasers provide frequency tunability via the strength of the applied magnetic field and deliver watt-level powers [73].

Terahertz quantum cascade lasers (QCLs) rely on a rather different lasing concept compared to regular diode lasers that are based on the recombination of electron hole pairs between the conduction band and the valence band of a semiconductor. In QCLs solely electrons participate in the lasing process that takes place in form of intersubband transitions in the conduction band of a periodic semiconductor heterostructure [74,75]. The emission wavelength can be designed by precisely adjusting the layer thicknesses and compositions of the alternating semiconductor materials that build an artificially engineered discrete energy level structure. The flexibility of THz QCL designs led to emission frequencies ranging from 0.63 to 5.4 THz [76, 77] with power levels exceeding 2 W [78]. Their main drawbacks are the restriction to low operation temperatures $\leq$ 250 K [79] and the inflexible spectral output, which is defined and fixed by the chosen optical cavity. Tuning of the emission spectrum can only be achieved to a small extend through adjustment of the driving current or the operation temperature, which still shows the potential for spectroscopic applications [80].

2.2.5 Difference Frequency Generation

A workaround for the current difficulties in developing light sources emitting directly in the THz range presents difference frequency generation (DFG). DFG is a down-conversion process based on lasers with frequencies f_1 and f_2 operating in a high frequency range compared to the THz (e.g. the NIR). New light is generated determined by the initially defined frequency offset $f_{THz}=f_2-f_1$ lying in the THz range.

Various nonlinear optical crystals like GaSe, GaP, DAST and $LiNBO_3$ exhibit the ability for DFG [81, 82], when illuminated with two input frequencies. The amount of generated output power and its frequency tuning range depend on their second-order nonlinear coefficients and the degree of achievable phase matching. Also quantum cascade structures of QCLs provide

a large optical nonlinearity, which led to the utilization of mid-IR QCLs delivering THz light on the basis of DFG coming with the advantage of room temperature operation compared to THz QCLs [83]. Such sources cover a range of 1 to 6 THz and reach output powers of almost 2 mW in pulsed operation, while continuous wave driven, they are still limited to microwatts [84].

Besides nonlinear crystals, ultrafast electronic devices can also be used for DFG, which is called photomixing in this context. An optical beating signal with f_{THz} is created by the overlap of high frequency laser beams. The combined light illuminates a photomixer, which generates a photocurrent in the device following the incident time-varying optical intensity. This photocurrent modulation drives a resonant antenna structure integrated into the photomixer, emitting THz light. Commonly used devices generating sufficient output powers include uni-travel-carrier photodiodes (UTC-PDs [85]) and photoconductive antennas (PCAs) based on semiconductors with short carrier lifetimes [86]. Typical output powers lie in the microwatt range and their tunability reaches up to 3.8 THz [87]. Besides their tunability, their main advantages are room temperature operation and low production costs. They are very compact devices easy to use since they can be packaged with optical fibers delivering the driving light, bias lines for electrical connection and a silicon lens facilitating THz light outcoupling. The driving lasers greatly influence the quality of the THz output, which inherits their common coherence, and thus, linewidth as well. To overcome the major drawback of photomixers - rather low output powers - array configurations have been realized, utilizing their mutual coherence length as long as the CW source light is delivered to all THz emitters equally [88]. When the driving lasers are stabilized by modern locking techniques, they pass on this stability to the THz radiation, which enables excellent linewidths [89]. Besides two independent laser sources, also a single two-colour laser source can be used for driving the photomixer, further simplifying the optical setup [90]. This brings the additional advantage that the mixing colours origin from the same laser system, and thus, share their noise characteristics, which will narrow the terahertz linewidth as well. It should be mentioned that the non-linear gain medium of a two-colour laser can be used itself for the difference frequency generation process instead of an external photomixing device [91].
All in all, the above mentioned advantages make CW photomixers convenient and reliable THz sources that are utilized in various systems all over the field of application of terahertz technologies, which was introduced at the beginning of this chapter. This work relies on a photomixer as room temperature THz source as well, therefore a detailed description of the photomixing principle based on PCAs is given in chapter 3.1. An in-depth review of CW terahertz photomixing systems and applications can be found in Refs. [92, 93].

2.3 Detecting Terahertz Light

A THz detector is a transducer with the ability to convert incoming THz radiation into a convenient, usually electrical, signal that can be recorded and analyzed. Detection of THz light faces similar problems to those discussed regarding its generation, centered around the issue of non-existent band gaps in this frequency domain, necessitating alternative concepts in comparison to the standard photodetectors used in the visible and NIR domains. A wide range of physical effects can be utilized in detection systems and its majority is discussed in the following. A rigorous comparison of present THz detectors can be found in the recent review of R. A. Lewis [94].

2.3.1 Thermal Detectors

In thermal detectors the incoming THz photons are absorbed by the detector material, consequently producing heat, which causes a change of any measurable physical property. In general, they provide broad spectral coverage, but on the other hand they are usually comparatively slow.

Bolometers are the most widely used kind of thermal THz detectors relying on a change in resistance of an absorbing element that is heated up by the incoming radiation [95, 96]. The absorbing element is connected to a thermal reservoir of constant temperature, and the detection speed is defined by the ratio of the absorber's heat capacity and the thermal conductance to the reservoir. Cooling down such devices enables faster detection up to the kHz level. Further increase of the detection speed up to MHz can be achieved with hot electron bolometers (HEBs) that come with the necessity of cryogenic cooling [97].

In pyroelectric materials (e.g. deuterated triglycine sulfate - DTGS), heating and cooling causes the material's lattice spacing to alter leading to a temporary surface charge. Detectors based on the pyroelectric effect measure a change of this in-built electrical charge that is proportional to the change in temperature [98]. Since the principle is based on the variation of the temperature, only time varying radiation can be measured, which prohibits the detection of continuous wave signals. Despite this limitation, such detectors come with the advantage of compact size and room temperature operation.

A Golay cell consists of a cell containing a flexible membrane that is filled with gas. Heating that gas by incident radiation leads to expansion, resulting in deformation of the membrane, which is measured with an optical system (i.e. deflection of a laser and detection by a photodiode) [99]. The Golay cell is advantageous in terms of sensitive, broadband, and room

temperature detection, while the slow gas expansion and membrane deformation limits its response time to a few 10s of milliseconds. Besides, its delicate construction and optical read out make the detector fragile to mechanical vibrations.

The thermoelectric effect is used in thermopile detectors, which are constructed with two different metals connected in series. The first metal absorbs the radiation, while the second acts as a heatsink, resulting in a voltage drop that depends on the absolute temperature [100]. Thermopiles have the benefit of low production costs, the ability to operate at room temperature and to detect continuous wave radiation. However, they are subject to thermal drifts and are relatively slower compared to other types of sensors.

2.3.2 Photodetectors

The principle of photodetectors is based on the interaction of the incoming THz photons with electrons in the detector material. Thereby, a measurable resistance change is produced, which can be read out. Only at frequencies >10 THz the photons have energies high enough to make use of an intrinsic electron transition between the valence band and the conduction band across a semiconductor's band gap.

For lower frequencies, extrinsic electron transitions can be realized between shallow impurity states localized within the band gap and the conduction or valence band. In general, such extrinsic detectors are very fast, since solely electrons are involved in the detection process and they exhibit a sharp cut-off frequency. Typically, these detectors require cooling close to liquid helium temperatures in order to prevent thermal ionization. Different materials can be used to generate the required impurity states. The very first THz photoconductor was based on p-doped germanium using antimony as dopant (Ge:Sb) [101]. Gallium doped devices (Ge:Ga) are among the most widely used THz photodetectors [102] covering a frequency range from 1.5 THz to 8 THz with a detectivity peak around 3 THz providing response times about 2 ns [103]. The sensitivity above 6 THz can be increased using beryllium as dopant (Ge:Be) [104]. Due to its lower effective electron mass, indium antimonide (n-InSb) is a more suitable semiconductor material for applications in the low THz range with response times typically about 300 ns [105]. Applying an external magnetic field results in a Landau level splitting. The magnetic field strength can be used for adjusting the optical transition energies between the newly generated levels leading to tunable narrowband detectors covering almost the whole THz range [106].

Schottky photodiodes are based on electron trapping at a metal-semiconductor interface forming a potential barrier. Incident THz radiation provides the energy for releasing those electrons, resulting in a measurable current. They can be used at ambient and cryogenic

temperatures, with applied voltage or with zero bias to reduce the shot noise. Schottky diodes cover a narrow band of 0.1-1.7 THz with a fast response up to 80 MHz [107,108]. For higher sensitivities, resonant tunneling diodes can be used instead [109].

The principle of electron transition by THz photon absorption is also employed in semiconductor heterostructure devices that create quantum wells with artificially designed electron states and transition energies. Adapting the structures of quantum well infrared photodetectors (QWIPs) enabled the absorption of THz photons by the excitation of an electron from the ground state into an upper state. With an applied bias, the electrons can escape, leading to a measurable current [110]. Cascading a sequence of quantum wells results in a quantum cascade detector (QCD), which supports efficient extraction of the excited electrons by transitions to the ground state of the neighbouring well [111]. The short lifetimes of the excited electrons in THz QWIPs and QCDs enable very fast THz detectors operating at GHz speed [112].

2.3.3 Plasmonic Detectors

THz light can also interact with plasmons (i.e. the quasiparticle of collective electron motion) in field effect transistors (FETs). The plasmons are confined between the source and the drain of the FET forming a plasma wave that is altered by the incident THz radiation leading to a photovoltage that can be measured. The most commonly used plasmonic detectors are Si FETs [113], but other approaches are used as well including Si metal oxide semiconductor FETs (MOSFETs) [114], high electron mobility transistors (HEMTs) based on GaAs [115] and InAlAs/InGaAs [116] and alternative concepts like graphene [117] and nanowire based FETs [118]. In general, plasmonic detectors are suitable for imaging applications due to their small size and typically room temperature operation. The advantages of standard complementary metal-oxide-semiconductor (CMOS) technology enables low power consumption of about 100 µW and on-chip integration. However, their limited spectral range renders them unsuitable for spectroscopy applications, and their detectivity is limited by noise in the electronics.

2.3.4 Heterodyne Detection

In a heterodyne system, the detector acts as a mixer, combining the signal to measure and a local oscillator (LO) operating close to the signal frequency. The result is the generation of the difference frequency, which lies within the device's optimized working range, typically a few GHz. This process is known as mixing or down-conversion. Due to the down-conversion, amplifiers can be utilized, something which would not be possible directly at the high signal

frequencies since there are no available high speed amplifiers. Various devices with nonlinear I-V curves can be used as mixers including Schottky diodes [119] and superconductor-insulator-superconductor (SIS) mixers. SIS mixers are composed of two superconductors separated by a thin insulating layer. Their principle is based on photon-assisted tunneling of quasiparticles through the insulating layer [120]. LO powers on the μW level are sufficient for operation, while Schottky mixers require ∼1 mW. On the other hand, Schottky mixers are more robust against LO fluctuations. Alternatively, very fast bolometers can also be employed as mixers. High heat conductivity and small heat capacitance are required to reach proper bandwidths up to 10 GHz, such as in superconducting HEBs [121]. Among the described mixers, SIS devices are the most sensitive ones, while HEB mixers are still significantly more sensitive than Schottky mixers. Beyond ∼1.3 THz NbN HEB mixers are most widely used in heterodyne systems due to their sensitivity [122].

3 Fundamentals

The aim of this chapter is to provide an overview about the basic principles needed to comprehend the methods and results of this thesis. It will give a brief introduction to the relevant topics, namely the generation of continuous terahertz radiation via the photomixing approach, the theory of wave guiding in rectangular metallic hollow waveguides and the fundamentals of vibrational-rotational transitions in molecular systems.

3.1 Photomixing for Continuous Wave Terahertz Generation

Photomixers present a combination of electronic and optical technologies to generate coherent continuous wave (CW) terahertz radiation. Although their output powers are moderate (usually limited to a few microwatts), their large tuning range and room temperature operation make them very appealing.

Photomixing involves two single-frequency, adjustable diode lasers to create a THz frequency difference in a photoconductive material, such as low-temperature-grown gallium arsenide (LTG GaAs) [86]. The output frequency can be changed by detuning the wavelength of the laser diodes via operation temperature or driving current adjustments. The principle relies on the modulation of the photoconductance of the mixer with the optical beating between those two lasers, and the THz output power is drawn from the source providing a DC bias at the photoconductor electrodes. In that sense, photomixing is substantially different from other difference frequency generation approaches based on $\chi^{(2)}$ processes (i.e. a nonlinear effect proportional to the second order component of the susceptibility χ) in materials like zinc telluride (ZnTe) or lithium niobate ($LiNbO_3$) [82]. There, each low energy THz photon arises from a pair of high energy optical photons leading to an efficiency penalty at lower THz frequencies, which favours the photomixing process in terms of efficiency and output power. For frequencies above several THz, $\chi^{(2)}$ mixing becomes more efficient due to parasitic impedances in photomixers, which results in a bandwidth limitation [123].

Figure 3.1 displays a common CW THz photomixing setup based on a photoconductive antenna as mixing element. Two laser diodes (LD1 and LD2) with slightly different frequencies ($f_1 = \omega_1/(2\pi)$ and $f_2 = \omega_2/(2\pi)$) generate an optical beating signal that modulates the

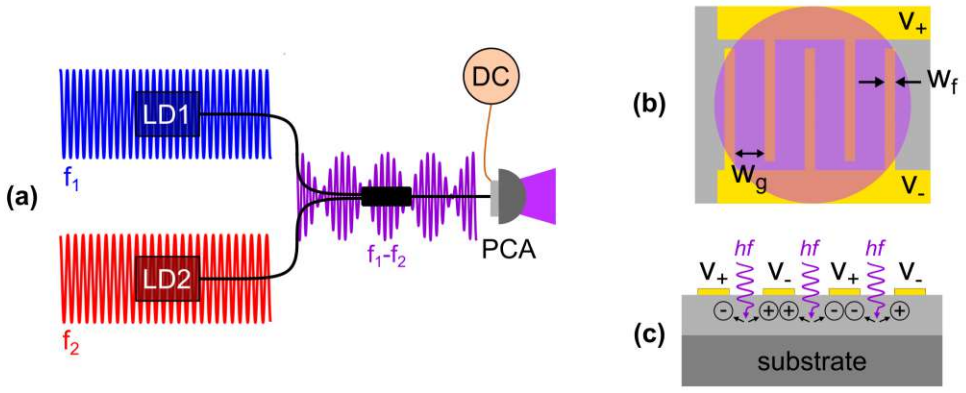

Figure 3.1: CW terahertz photomixing setup. (a) The combination of laser 1 (LD1) at frequency f_1 and laser 2 (LD2) at frequency f_2 create the optical beating signal at $f_1 - f_2$ that drives the photoconductive antenna (PCA) and emits terahertz radiation into free space via the attached silicon lens. (b) Top view of the illuminated interdigitated electrodes of the resonant antenna structure with gap width w_g and finger width w_f. (c) Side view of the electrodes constructed onto the photoconductive material. The incident photons of energy hf generate carriers that are collected as photocurrent by the applied DC bias.

photomixer's carrier density. This translates into a modulated photocurrent, coupled out as CW THz radiation by means of a resonant antenna structure (e.g. bow-tie or log-spiral geometry). With help of an attached silicon lens the generated THz wave is focused and forms a Gaussian beam. The frequencies of the two diode lasers are slightly above the band gap of the used photoconductive material, thus, they are able to generate photocarriers. Their light is combined in a single-mode fiber and aligned to illuminate the interdigitated electrodes manufactured on the active layer of that material. In first approximation, the electric field applied between the electrode fingers is described by

$$E_{DC} = \frac{V_B}{w_g}, \tag{3.1}$$

with the bias voltage V_B and the gap width w_g between the electrode fingers. It collects the carriers generated by the incident light leading to a photocurrent

$$I_{ph} = e\tau_c\mu_e E_{DC} N_e, \tag{3.2}$$

defined by the elemental electron charge e, the electron mobility μ_e and the carrier lifetime τ_c of the photoconductive material, as well as the number of photo-generated carriers N_e that

follows the generation rate

$$\frac{dN_e(t)}{dt} = \eta_{ext}\frac{P_B}{hf}. \tag{3.3}$$

It is composed by the product of incident photons per unit time $P(t)/(hf)$ - described by the optical power $P(t)$ and the photon energy hf - and the external quantum efficiency η_{ext}, which depends on the absorption and reflectivity coefficients of the material.

The incident optical beating signal at the photomixer is generated by the joint optical field of the two driving lasers LD1 and LD2. At the excitation point, it is given by

$$E(t) = E_1 e^{-i\omega_1 t} + E_2 e^{-i\omega_2 t}, \tag{3.4}$$

with the electric field amplitudes E_1 and E_2, respectively. For the optical intensity follows

$$I = \frac{cn\epsilon_0}{2}|E(t)|^2, \tag{3.5}$$

where c marks the speed of light in vacuum, n the refractive index, and ϵ_0 the vacuum permittivity. Its expanded expression reads

$$\begin{aligned} I(t) &= \frac{cn\epsilon_0}{2}[E_1^2\cos^2(\omega_1 t) + E_2^2\cos^2(\omega_2 t) + 2E_1E_2\cos(\omega_1 t)\cos(\omega_2 t)] \\ &= \frac{cn\epsilon_0}{2}[E_1^2/2 + E_2^2/2 + E_1^2/2\cos^2(2\omega_1 t) + E_2^2/2\cos^2(2\omega_2 t) \\ &\quad + E_1E_2\cos^2((\omega_1+\omega_2)t) + E_1E_2\cos^2((\omega_1-\omega_2)t)]. \end{aligned} \tag{3.6}$$

The photomixer device is not able to follow the fast oscillating frequencies $2\omega_1$, $2\omega_2$ and $\omega_1+\omega_2$, due to its relatively slow response. In the following, the corresponding terms will be discarded, so only the DC terms and the difference frequency term $\Delta\omega = \omega_1 - \omega_2$ remain

$$I(t) = I_1 + I_2 + I_B(t) = I_1 + I_2 + 2\sqrt{I_1 I_2}\cos(\Delta\omega t). \tag{3.7}$$

Here, the total intensity consists of I_1 and I_2 - the intensities of the two driving lasers - along with a time-varying beating intensity $I_B(t)$. The incident optical power at the photomixer is calculated by integrating over the beam cross section $P_i(t) = \int cn\epsilon_0 E_i^2/2 \, \mathrm{d}S$, and thus, can be expressed as [124]

$$P(t) = \int cn\epsilon_0 I(t)\mathrm{d}S = P_1 + P_2 + P_B(t) = P_1 + P_2 + 2\sqrt{mP_1P_2}\cos(\Delta\omega t), \tag{3.8}$$

with P_1 and P_2 the average power of laser 1 and laser 2 that accompany the beating power $P_B(t)$. The mixing ratio m ranges from 0 to 1 and describes the spatial overlap between

the two laser beams. The THz radiation power P_{THz} can be found via the solution of the current-continuity equation in the small signal approximation [124, 125]

$$P_{\mathrm{THz}} = \frac{I_{ph}^2 R_A}{2[1+(\Delta\omega\tau_c)^2][1+(\Delta\omega R_A C_A)^2]}, \tag{3.9}$$

with the antenna radiation resistance R_A, the carrier lifetime of the photoconductive material τ_c, the capacitance of the photomixer C_A and the photocurrent I_{ph} flowing through the antenna structure. The latter is described by equation 3.2, leading to a THz power

$$P_{\mathrm{THz}} \propto E_{\mathrm{DC}}^2 P_B^2, \tag{3.10}$$

where it becomes evident that the power increases not solely with the optical power of the beating fields P_B, but also with the applied bias field E_{DC}.

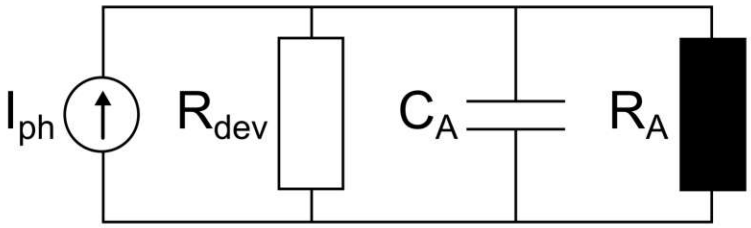

Figure 3.2: Equivalent circuit of a THz photoconductive antenna with the device resistance R_{dev}, the antenna capacitance C_A and its radiation resistance R_A.

Figure 3.2 displays the equivalent circuit of a photoconductive antenna photomixer. The electrical device as a whole exhibits a resistance R_{dev}, while the antenna has a radiation resistance R_A and the metal electrode structure induces a parasitic capacitance

$$C_A = \epsilon \frac{A}{d}, \tag{3.11}$$

which can be defined via the permittivity ϵ of the material, the cross section area of the electrodes A and the electrode distance d. This capacitance hinders the modulation of the photocurrent for high frequencies leading to the frequency dependent RC roll-off for THz emission, which can be described by the coefficient [126]

$$\eta_{RC} = \frac{1}{1+(\Delta\omega R_A C_A)^2}. \tag{3.12}$$

Another limitation for high frequency terahertz generation comes from destructive interference. The individual carriers of the photocurrent are generated at various positions within

the material and subsequently travel different distances to reach the next electrode leading to varying phases that contribute to the photocurrent. To avoid destructive interference, the carrier lifetime τ_c should be short. The lifetime roll-off is described by the coefficient [92]

$$\eta_{LT} = \frac{1}{1 + (\Delta\omega\tau_c)^2}. \tag{3.13}$$

Although a short carrier lifetime adversely impacts the photocurrent generation according to equation 3.2. Therefore, the search for efficient photoconductive materials for CW terahertz generation requires a balance between short τ_c values for a decreased lifetime roll-off and the resulting reduced photocurrent generation rate.

The emitted terahertz power of the photomixer can be expressed in terms of the roll-off coefficients via equation 3.9 leading to

$$P_{\mathrm{THz}} = \frac{1}{2} I_{ph}^2 R_A \eta_{RC} \eta_{LT}. \tag{3.14}$$

The coefficients limit the high frequency performance of the device since both roll-offs decrease the emitted power P_{THz} with $\Delta\omega^2$.

Besides the limitations regarding the optical bandwidth, Figure 3.2 can also be used to discuss the electrical bandwidth of PCA photomixers. The device resistance under illumination is usually R_{dev} $\geq$10 kΩ and typical values for C_A lie in the fF range [92]. Consequently, the electrical cut-off frequencies are in the range of a few GHz, which qualifies these devices for fast modulation and heterodyne detection [127]. The final electrical bandwidth is certainly further influenced by the high frequency performance of the whole system, usually including cables, striplines, amplifiers or filters.

3.2 Rectangular Metallic Hollow Waveguide Theory

Electromagnetic waves can be confined within a waveguide structure, which prevents them from spreading and incurring losses, and essentially transmits a signal from one point to another. Rectangular waveguides are among the most common types of waveguides and are constructed from a hollow conducting tube with a rectangular cross-section. These waveguides permit light guiding and are typically used for signal transmission. Electromagnetic waves traveling through a rectangular waveguide are reflected of the conducting walls, resulting in either an electric or magnetic field component in the direction of transmission. There is no transverse electromagnetic (TEM) mode that can propagate in rectangular waveguides. Instead, the modes of propagation are transverse electric (TE) and transverse magnetic (TM) modes,

which need to fulfill the Helmholtz equations and the boundary conditions. The latter involves the tangential components of the electric field and the normal derivative of the tangential components of the magnetic field being equal to zero at the conducting walls of the waveguide. An in-depth description and derivation of the solutions for the modes in a metallic rectangular hollow waveguide can be found in Ref. [128]. Here, the most important findings are presented.

3.2.1 Transverse Electric Modes

Transverse electric (TE) waves are defined by components $E_z = 0$ and $H_z \neq 0$, when z represents the propagation direction through the waveguide. In a rectangular waveguide of cross section $a \times b$, with $0 < x < a$, $0 < y < b$ and $b < a$, the electromagnetic fields for TE-waves are determined by solving the Helmholtz equation for the longitudinal component (H_z)

$$\nabla^2 H_z + k^2 H_z = 0, \tag{3.15}$$

where k denotes the wavenumber. H_z also needs to satisfy the boundary conditions

$$\frac{\partial H_z}{\partial x}(0, y, z) = \frac{\partial H_z}{\partial x}(a, y, z) = \frac{\partial H_z}{\partial y}(x, 0, z) = \frac{\partial H_z}{\partial y}(x, b, z) = 0. \tag{3.16}$$

One finds, an infinitely number of solutions for TE_{mn} waves traveling in z direction through the waveguide, which can be expressed by

$$H_{zmn}(x, y, z) = h_{mn} \cos\left(\frac{m\pi x}{a}\right) \cos\left(\frac{n\pi y}{b}\right) e^{-ik_z z}, \tag{3.17}$$

where h_{mn} is the propagation amplitude, while m and n are integers numbering the solutions. All pairs of $(m, n) \neq (0, 0)$ are allowed in general. The remaining transverse electric and magnetic fields are calculated via Maxwell's equations. Their spatial dependencies read as

$$\begin{aligned} E_x &\sim \cos\left(\frac{m\pi x}{a}\right) \sin\left(\frac{n\pi y}{b}\right) e^{-ik_z z} \\ E_y &\sim \sin\left(\frac{m\pi x}{a}\right) \cos\left(\frac{n\pi y}{b}\right) e^{-ik_z z} \\ H_x &\sim \sin\left(\frac{m\pi x}{a}\right) \cos\left(\frac{n\pi y}{b}\right) e^{-ik_z z} \\ H_y &\sim \cos\left(\frac{m\pi x}{a}\right) \sin\left(\frac{n\pi y}{b}\right) e^{-ik_z z}. \end{aligned} \tag{3.18}$$

All of them fulfill the Helmholtz equation and the boundary conditions as well. The z component of the wave vector k_z is given by

$$k_z = \sqrt{k^2 - \left(\frac{m\pi}{a}\right)^2 - \left(\frac{n\pi}{b}\right)^2}, \tag{3.19}$$

for a given angular frequency $\omega = ck$. From equation 3.19, one finds the condition for wave propagation such that

$$k^2 - \left(\frac{m\pi}{a}\right)^2 - \left(\frac{n\pi}{b}\right)^2 > 0, \tag{3.20}$$

which implies that only the solutions (m, n) that fulfill this condition lead to real values for k_z, and thus, to a propagating TE_{mn} mode. With this, a cut-off frequency can be defined

$$f_{\mathrm{cut}} = \frac{c}{2\pi}\sqrt{\left(\frac{m\pi}{a}\right)^2 + \left(\frac{n\pi}{b}\right)^2}. \tag{3.21}$$

Electromagnetic waves with frequencies $f \leq f_{\mathrm{cut}}$ can not propagate through the waveguide. The mode with the lowest cut-off frequency is called the fundamental mode of the waveguide and is the TE_{10} mode with the smallest cut-off frequency $f_{\mathrm{cut}} = c/2a$.

3.2.2 Transverse Magnetic Modes

The solutions for transverse magnetic (TM) waves with components $H_z = 0$ and $E_z \neq 0$, are found in an analogous way. The electromagnetic fields are obtained from

$$\nabla^2 E_z + k^2 E_z = 0, \tag{3.22}$$

whith the boundary conditions

$$E_z(0, y, z) = E_z(a, y, z) = E_z(x, 0, z) = E_z(x, b, z) = 0. \tag{3.23}$$

The infinitely number of solutions for TM_{mn} waves are expressed by

$$E_{zmn}(x, y, z) = e_{mn} \sin\left(\frac{m\pi x}{a}\right) \sin\left(\frac{n\pi y}{b}\right) e^{-ik_z z}. \tag{3.24}$$

Again, the corresponding transverse electric and magnetic field components are obtained from the Maxwell equations and exhibit the same spatial dependencies given in equation 3.18. Also the cut-off frequencies for TM modes are the same as for TE modes (equation 3.21), with the additional restriction that $m \neq 0$ and $n \neq 0$.
The electric field distributions of the first few TE and TM modes developing in a rectangular metallic hollow waveguide are depicted in Figure 3.3.

When the fundamental mode TE_{10} is used for signal transmission in a waveguide, the waveguide geometry can be designed, such that all higher order modes are suppressed due to their higher cut-off frequencies. This might be important, since higher order modes propagate at different speeds as will be shown below, which distorts the phase of the travelling wave.

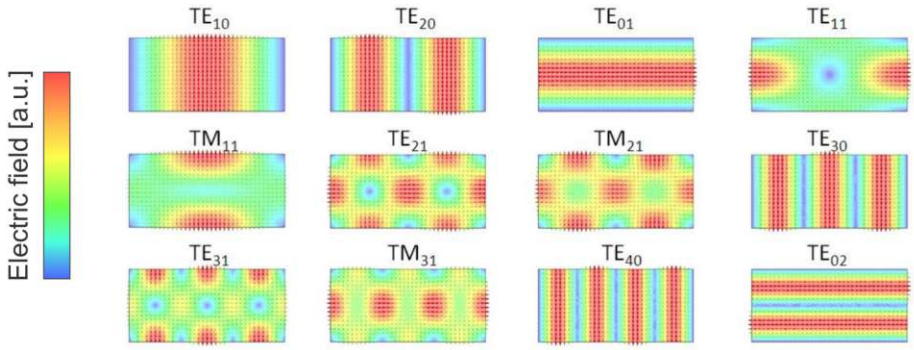

Figure 3.3: Electric field distributions of the first few modes in the transverse plane of a rectangular waveguide with dimensions $a = 2b$. Figure adapted from [129].

3.2.3 Phase and Group Velocity

The speed at which the phase fronts of light move through a waveguide is known as the phase velocity v_{ph}, while the speed at which energy (or signal information) travels through a waveguide is referred to as the group velocity v_g. For a plane wave developing in vacuum, v_{ph} and v_g are both equal to the speed of light c. In waveguides on the other hand, it turns out that the phase and the group velocity are both frequency dependent and not the same anymore. The phase velocity is defined by

$$v_{ph} = \frac{\omega}{k_z}, \tag{3.25}$$

while the group velocity is calculated via

$$v_g = \left(\frac{\mathrm{d}k_z}{\mathrm{d}\omega}\right)^{-1}. \tag{3.26}$$

The z component of the wave vector k_z is given by equation 3.19, together with the identity $k = \omega/c$, this leads to an expression for the phase velocity [128]

$$v_{ph} = \frac{\omega}{k_z} = \frac{\omega}{\sqrt{k^2 - \left(\frac{m\pi}{a}\right)^2 - \left(\frac{n\pi}{b}\right)^2}} = \frac{c}{\sqrt{1 - (f_{\mathrm{cut}}/f)^2}}, \tag{3.27}$$

where it becomes evident that $v_{ph} > c$. For the limit $f \to f_{\mathrm{cut}}$, the phase velocity approaches infinity $v_{ph} \to \infty$, while for the limit $f \to \infty$, the phase velocity approaches the speed of light $v_{ph} \to c$.

For the group velocity, one finds [128]

$$v_g = \left(\frac{\mathrm{d}k_z}{\mathrm{d}\omega}\right)^{-1} = c\frac{k_z}{k} = c\sqrt{1-(f_{\mathrm{cut}}/f)^2}, \tag{3.28}$$

with the characteristic property of $v_g < c$. In the limit of $f \to f_{\mathrm{cut}}$, the group velocity vanishes $v_g \to 0$, while in the limit of $f \to \infty$, the group velocity approaches the speed of light $v_g \to c$. Figure 3.4 illustrates the relationship of v_{ph} and v_g with the normalized frequency f/f_{cut}. It becomes immediately clear that no modes of frequencies below the cut-off frequency can propagate within the waveguide and that for frequencies much larger than the cut-off, the waveguide behaves like free space regarding the propagation of modes with $v_{ph} = v_g = c$.

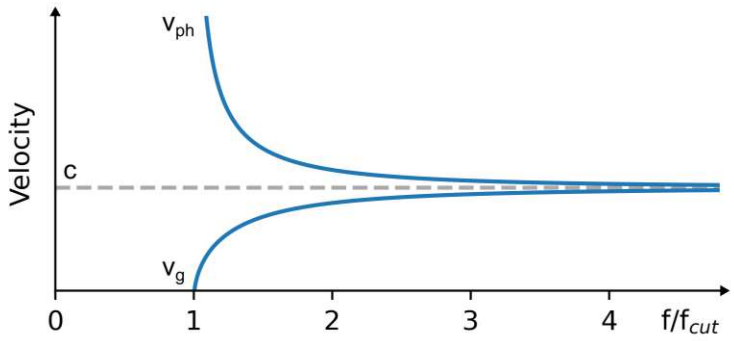

Figure 3.4: Phase velocity v_{ph} and group velocity v_g depending on the frequency ratio f/f_{cut}, both approaching the speed of light c for an increasing ratio.

3.3 Vibrational-Rotational Transitions in Molecules

Vibrational-rotational spectroscopy presents a mature technique to correlate physical properties of materials to their molecular structure more accurately than any other analytical method. Every molecule exhibits a characteristic fingerprint spectrum consisting of vibrational and rotational modes, which are slightly different from all other molecules and also change with their state of aggregation. Therefore, the molecular spectrum of a given substance is unique and identifies that molecule precisely. This type of analysis provides far more detailed information than just the presence or absence of a certain substance. Applications range about various fields including the quantification of complex mixtures, biomedical and biologi-

cal spectroscopy, microspectroscopy and hyperspectral imaging, the exploration of dynamic systems, and the examination of a variety of interfacial phenomena [130].

Molecular spectra are generated by transitions between quantized energy states. Molecules containing N atoms have in general 3N degrees of freedom regarding their motion. Three out of these represent the translational motion in the x, y, and z directions. Other three are for the rotation around the x, y, and z axes (i.e. the rotational modes). The remaining 3N-6 degrees of freedom represent the number of ways that the atoms in a nonlinear molecule can vibrate, commonly known as the vibrational modes. Vibration-rotation spectroscopy is a quite complex theory, which is beyond the scope of this thesis. Here, a brief introduction is provided. An in-depth exposition can be found in the literature, such as in Ref. [131].

3.3.1 Molecular Vibrations

The vibrations of molecules can range from the relatively simple movement of two atoms to the rather complex behaviour of a large polyfunctional molecule, where the motion of each molecule contributes to the vibrational mode. For each mode, the atoms move approximately harmonically away from their equilibrium positions, resulting in a change of the molecule's dipole moment while its center of mass remains unchanged. For each mode i all the atoms vibrate at the characteristic frequency ν_i, leading to the vibrational energy states of the harmonic oscillator

$$V_i = h\nu_i \left(v_i + \frac{1}{2} \right), \tag{3.29}$$

where h denotes the Planck constant and v_i the vibrational quantum number of the mode i.

From the Schrödinger equation one finds the selection rule for vibrational changes for the harmonic oscillator to be $\Delta v_i = \pm 1$. Actual molecules do not follow exactly a simple harmonic motion, it can be more accurately described by an anharmonic (Morse-type) function, which allows transitions $|\Delta v_i| > 1$ as well. It is shown in Figure 3.5 in comparison to the harmonic oscillator potential with the energy states given to a first approximation by [130]

$$V_i = h\nu_i \left(v_i + \frac{1}{2} \right) + h\nu_i x_i \left(v_i + \frac{1}{2} \right)^2, \tag{3.30}$$

where x_i is a dimensionless anharmonicity constant with values usually lying in the range of -0.001 to -0.02.

When a molecule absorbs energy ΔE corresponding to one of its molecular vibrations according to $E = h\nu_i$, the vibration is excited. A fundamental vibration is evoked by a

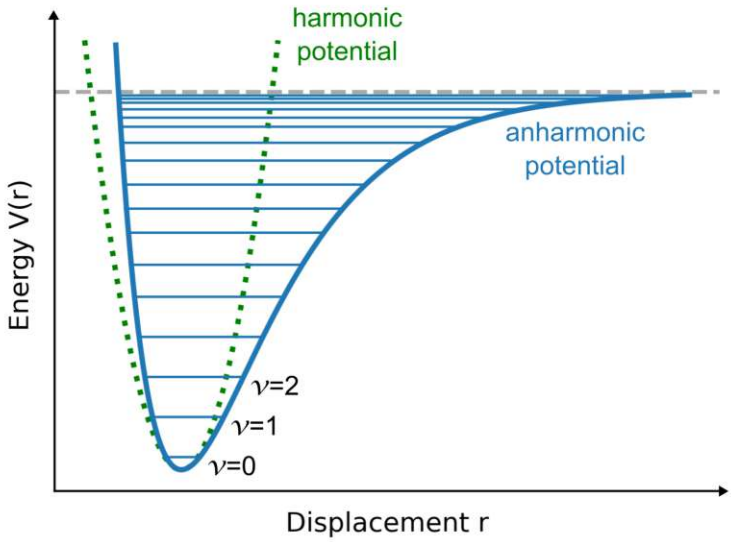

Figure 3.5: Vibrational potential energy $V(r)$ in dependence of the atomic displacement r for a diatomic molecule. The dashed green line illustrates the harmonic oscillator potential and the solid blue line depicts the anharmonic (Morse type) oscillator with discrete energy states v.

quantum number change of $\Delta v_i = \pm 1$, while overtone vibrations correspond to $|\Delta v_i| > 1$. The typical fundamental vibrational frequencies are located in the mid-infrared domain with corresponding wavenumbers 400-4000 cm^{-1} (the unit most commonly used in spectroscopy) and their overtones are partially reaching above 4000 cm^{-1} into the near-infrared (NIR) range. The fundamental vibrations of most pure compounds are generally easy to saturate (resulting in less than 1% signal transmittance thorough the sample), making the overtone bands often more readily accessible, which made NIR spectroscopy a well-established analysing technique.

3.3.2 Molecular Rotations

Besides the vibrations of molecules, also their rotations lead to quantized energy states defined by the Schrödinger equation. For complicated systems, there are hardly general solutions without rigorous approximations. Here, the discussion will be restricted to some straightforward scenarios for the understanding of the basic principles.

The most simple system in that regard is a diatomic molecule (depicted in Figure 3.6) assumed to be a rigid rotor, meaning the bond length does not change regardless of its rotation speed. Then, the rotational energy levels can be characterized by a single rotational

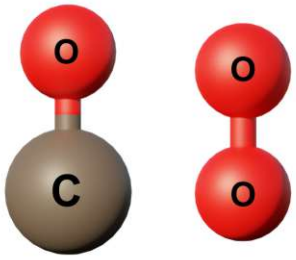

Figure 3.6: Schematics of an asymmetric (CO) and a symmetric (O_2) diatomic molecule.

quantum number J by the expression

$$E_J = BJ(J+1), \tag{3.31}$$

with the rotational constant

$$B = \frac{h}{8\pi^2 Ic}. \tag{3.32}$$

Here, h marks the Planck constant, I the molecule's moment of inertia and c the speed of light. For linear molecules the transitions are restricted by the selection rules to $\Delta J = \pm 1$, leading to transition energies of

$$E_J - E_{J-1} = BJ(J+1) - B(J-1)J = 2BJ. \tag{3.33}$$

Therefore, a pure rotational spectrum of a rigid rotor consists of a sequence of lines with an interval of $2B$ cm^{-1}, which is schematically depicted in Figure 3.7. Again, a change of the molecule's dipole moment is necessary for the transitions to become optically active. This is only the case for asymmetric molecules such as HCl and CO and not for examples like N_2 or O_2. In the majority of molecules, B is small leading to rotational transitions lying in the microwave range. For light molecules, these transitions move to the THz domain.

Diatomic molecules exhibit one fundamental vibrational mode of frequency ν_0. Any permitted vibrational transition of a diatomic molecule in a gaseous state, comes simultaneous with a rotational transition of $\Delta J = \pm 1$. Consequently, the corresponding rotational spectrum of a rigid diatomic molecule consists of a set of equally-spaced lines centered around ν_0. The so called R branch lies above ν_0 with $\Delta J = 1$ and the P branch below with $\Delta J = -1$.

Actual molecules are not rigid rotors, and as the angular velocity of the rotating molecule increases, the centrifugal forces lead to an expansion of the bond length between the two atoms. This phenomenon is known as centrifugal distortion, and it results in an increase in the

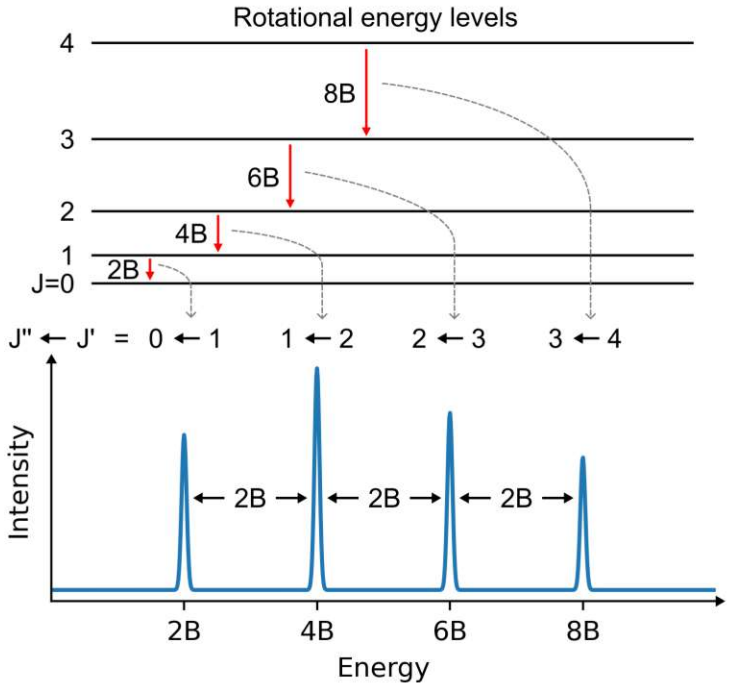

Figure 3.7: Schematic drawing of the rotational energy levels (J) of a rigid rotor and the transitions between them (J"←J') separated by 2B.

moment of inertia, thus reducing the constant B. To account for this, a second term is usually added to equation 3.31 leading to

$$E_J = BJ(J+1) - DJ^2(J+1)^2, \tag{3.34}$$

with the centrifugal distortion constant D. Due to that, the distance between lines in the P branch increases farther away from ν_0 and the distance between lines in the R branch decreases. In general, larger molecules with less symmetry exhibit transition lines with decreasing spacing and may introduce additional quantum numbers, causing the spectra to become more complicated.

3.3.3 Spectral Line Shape

In general, the vibrational-rotational spectral line shapes of a gaseous species depend on the pressure, the temperature, the transition frequency and the molecular mass. Each transition is associated with a certain amount of energy. However, non of this spectral lines is indefinitely sharp due to the following main broadening mechanisms:

- *Lifetime broadening.* Even the natural transition has a certain width defined by the Heisenberg uncertainty principle in energy and lifetime $\Delta E \Delta t \geq h/2\pi$. This effect leads to a Lorentzian line shape.

- *Pressure/collision broadening.* The lifetime Δt of an energy state in a molecule is reduced when it collides with other molecules, resulting in an increased uncertainty ΔE. This effect is determined by the density of the substance (i.e. the gas pressure) and the collision rate depending on the temperature. Generally, this broadening is also represented by a Lorentzian profile.

- *Doppler broadening.* The motion of particles results in a Doppler-shift of the transition frequency (and thus the energy). Due to the fact that the velocity of particles follows a Maxwell distribution, this effect occurs on both frequency sides leading to a broadening of Gaussian shape and is mostly temperature dependent.

The Lorentzian line shape, standardized for spectroscopic purposes, leads in the case of collision broadening to an expression for the absorbance in dependence of the wavenumber $\tilde{\nu} = \nu/c$ and is of the form

$$A_C(\tilde{\nu}) = A_0 \frac{\gamma_C^2}{4(\tilde{\nu} - \tilde{\nu}_0)^2 + \gamma_C^2}. \tag{3.35}$$

Here, A_0 represents the absorbance at $\tilde{\nu}_0$ and γ_C is the full-width at half-maximum for collision broadening, which is proportional to the gas pressure and increases with the polarity of every molecular component. Several different collision broadening mechanisms come with slightly different temperature dependencies (e.g. hard-sphere collisions lead to $\propto 1/\sqrt{T}$ and dipole-dipole interactions lead to $\propto 1/T$).

The Gaussian line shape in standardized form for Doppler broadening results in an absorbance given by

$$A_D(\tilde{\nu}) = A_0 \exp\left(\frac{-4 \ln 2 (\tilde{\nu} - \tilde{\nu}_0)^2}{\sigma_D^2}\right), \tag{3.36}$$

with the full-width at half-maximum for Doppler broadening expressed by

$$\sigma_D = 2\sqrt{\frac{2 \ln 2 kT}{m}} \tilde{\nu}_0, \tag{3.37}$$

where k is the Boltzmann constant, T the temperature and m the mass of the molecule.

If different broadening mechanisms are combined, the resulting line shape is the convolution of the individual broadening profiles. The combination of Doppler and pressure broadening effects are most accurately described by a so-called Voigt profile, and thus, determined by

$$A_V(\tilde{\nu}) = A_C(\tilde{\nu}) * A_D(\tilde{\nu}), \tag{3.38}$$

for which no analytical expression can be given. In a good approximation, its linewidth (i.e. the full width at half maximum) can be defined by [130]

$$\gamma_V = \frac{\gamma_C}{2} + \sqrt{\frac{\gamma_C^2}{4} + \sigma_D^2}. \tag{3.39}$$

Figure 3.8 depicts Voigt profiles for different values of σ_D and γ_C. The special cases of $\sigma_D = 0$ and $\gamma_C = 0$ lead to a pure Lorentzian and a pure Gaussian line shape, respectively.

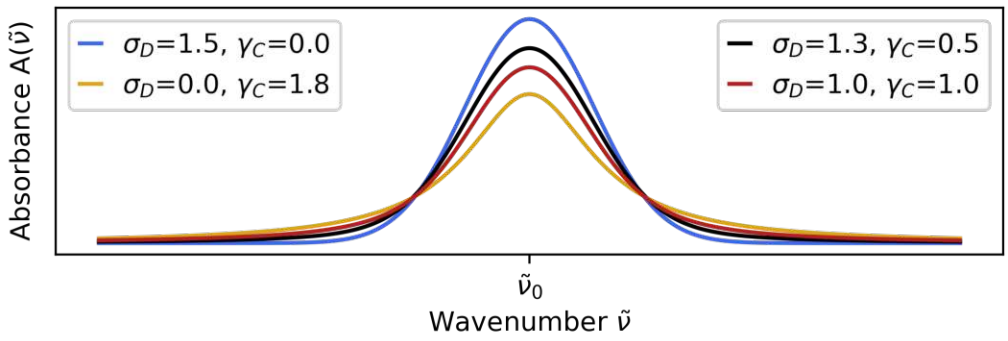

Figure 3.8: Voigt profiles for different σ_D and γ_C values forming the line shape of the absorbance A($\tilde{\nu}$) defined by different broadening mechanisms including the special cases for a pure Gaussian (blue) and a pure Lorentzian (yellow) profile.

Besides the linewidth, the intensity of a transition also determines its observable line shape, which is mainly determined by three factors:

- *Transition probability.* The transition probabilities between two states of a molecular system define how much this transition is pronounced in its measured absorption spectrum. As mentioned earlier, not all transitions between arbitrary energy states are allowed due to their selection rules. The calculation of absolute transition probabilities requires a thorough understanding of the quantum mechanical wave functions of the two states between which the transition occurs and is beyond the scope of this thesis. One should refer to the literature, such as Ref. [132].

- *Population of states.* The number of molecules in the states N_1 and N_2 between which the transition occurs influence the line strength as well. At equilibrium, the ratio of state populations can be expressed by

$$\frac{N_1}{N_2} = \exp\left(-\frac{\Delta E}{kT}\right), \tag{3.40}$$

  with the energy separation between both states $\Delta E = E_1 - E_2$, the temperature T and the Boltzmann constant k.

- *Sample path length.* At a given wavenumber $\tilde{\nu}$, the transmittance $T(\tilde{\nu})$ of a sample is determined by the ratio of the transmitted radiant power $I(\tilde{\nu})$ and the incident power $I_0(\tilde{\nu})$, which is given by the Beer-Lambert law

$$T(\tilde{\nu}) = \frac{I(\tilde{\nu})}{I_0(\tilde{\nu})} = \exp\left(-\alpha c L\right), \tag{3.41}$$

  where α marks the absorption coefficient for the specific transition, c the concentration of the sample and L the optical path length through the sample. The absorbance $A(\tilde{\nu})$ is defined by $A(\tilde{\nu}) = \ln(1/T(\tilde{\nu})) = \alpha c L$, which makes clear that the concentration of a substance is proportional to the absorbance of a sample rather then the transmittance.

3.3.4 Molecular Transitions in the Terahertz Domain

As mentioned above, mainly rotational transitions lie in the THz part of the electromagnetic spectrum. It turns out that most molecules that are relevant for environmental monitoring (such as H_2O or O_3) [135, 136] and medical diagnostics (e.g. CO or NH_3) [137, 138] have chemical fingerprints in the THz region due to their rotational spectra. This is also true for several security related substances like drugs (cocaine or ecstasy) [42] and explosives (e.g. trinitrotoluene - TNT and trinitrobenzene - TNB) [134]. Figure 3.9 presents the THz spectra of some of these important molecules.

Nowadays, molecular sensing is still mostly done in the well-established NIR domain. However, there are two further advantages that are provided by the THz field. Firstly, for some of the cited molecules the spectral line intensities of the vibrational transitions in the NIR are substantially smaller compared to the intensities of the rotational transitions in the THz. Therefore, they offer the potential of higher sensitivity for measurements at those lines. Figure 3.10 demonstrates the huge difference in line intensities in the NIR and in the THz range for water (H_2O) and ozone (O_3).

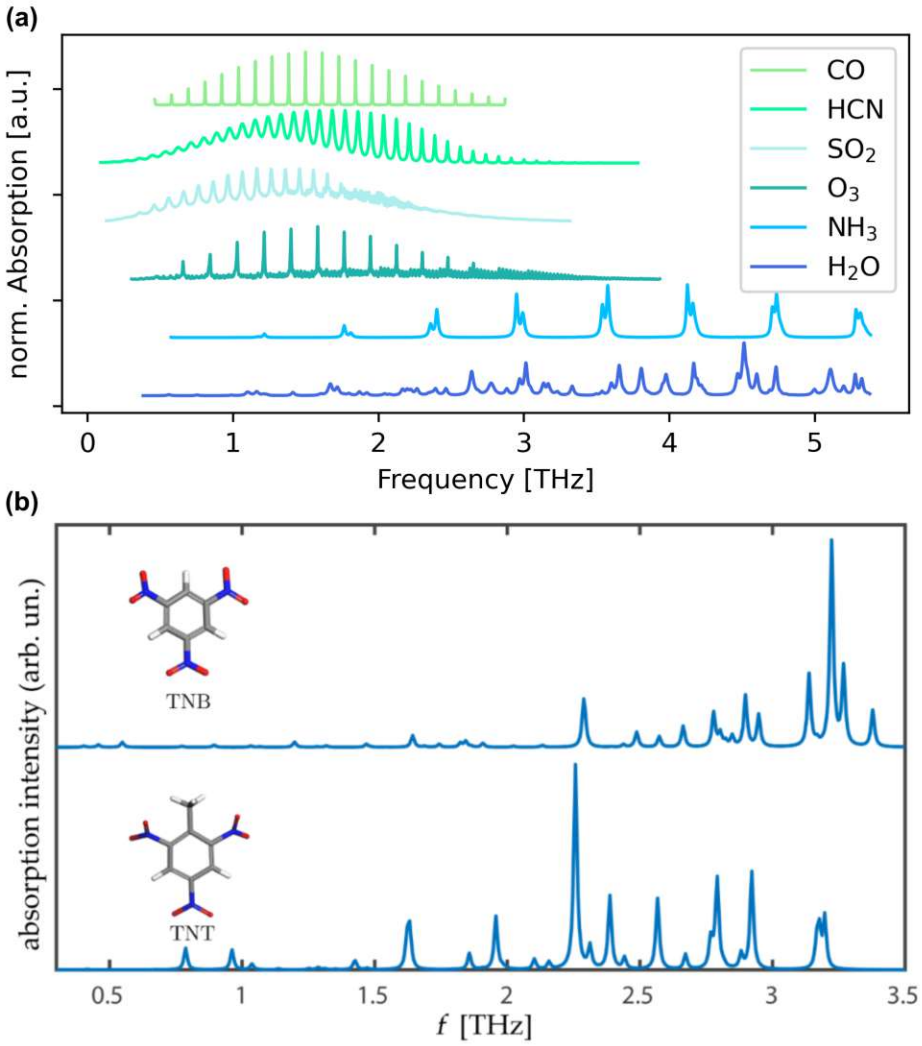

Figure 3.9: THz absorption spectra of a variety of important molecules. (a) Normalized absorption of six molecules calculated via the HITRAN database [133]. The spectra are offset for clarity. (b) THz spectra of two explosives (TNB and TNT), adapted from [134].

Secondly, the THz frequency span is relatively narrow, meaning that most of the relevant rotational transitions, even for different molecules, lie within a frequency window of somewhat ∼5 THz only (as already implied by Figure 3.9). In comparison, the vibrational transitions, especially for different molecules, span over hundreds of THz (indicated by Figure 3.10). Therefore, there is fundamentally no possibility to cover "all" relevant vibrational transitions with

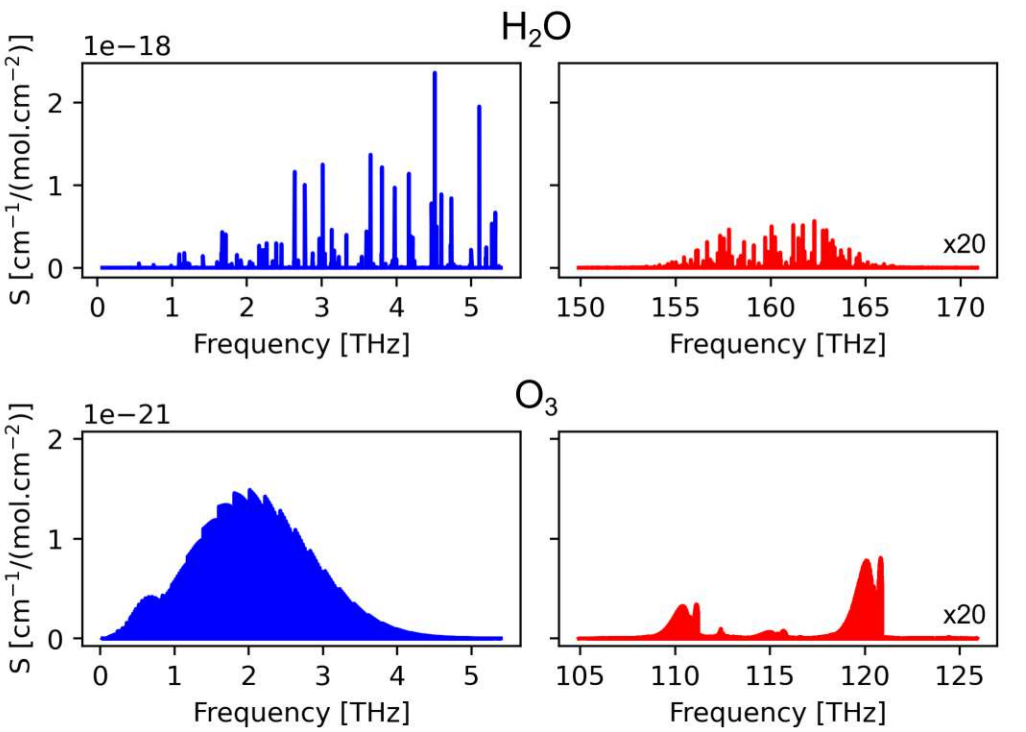

Figure 3.10: Comparison of the spectral line intensities (S) for water (H_2O) and ozone (O_3) in the THz (blue) and NIR (red) domain.

a single device, whereas the tunability over the interval of the rotational transitions is within reach for a single device.

4 Optical Frequency Combs

The development of the mode-locked laser by Hargrove et al. in 1964 [139] had a tremendous impact onto experimental lab work. It showed the emission of pulses in the time domain, which corresponds in the optical frequency domain to a spectrum consisting of numerous equally spaced lines forming a comb like picture. Accordingly, such a spectrum is referred to as optical frequency comb nowadays [140–142]. Its application as ruler in the frequency domain with metrological precision led to the Nobel Prize in physics for T. W. Hänsch and J. L. Hall in 2005 [143, 144]. Since their first demonstration OFCs had a significant impact in a various number of different fields including metrology, spectroscopy and frequency synthesis [140, 145, 146].

This chapter presents the fundamentals of optical frequency combs on the basis of mode-locked lasers, since the first realization of comb emission was achieved in such lasers. Following, the most common techniques for optical frequency comb generation are discussed with particular attention paid to electro-optic approaches. Finally, the current possibilities for comb emission in the terahertz domain are presented.

4.1 Fundamentals of Optical Frequency Combs

The optical field of the emission coming from a mode-locked laser forms a train of ultrashort pulses, as shown in Figure 4.1 (a). This is caused by the interference of myriad resonant longitudinal optical cavity modes. The periodic behaviour of the pulse envelope $A(t+\tau_{rt}) = A(t)$ is determined by the round-trip time $\tau_{rt} = 1/f_r = 2L/v_g$ inside the laser cavity with the length L and the group velocity of the light v_g, while f_r marks the repetition frequency of the pulses. The electrical field $E(t)$ can be described by a carrier frequency f_c (or its angular frequency analogue $\omega_c = 2\pi f_c$) that is modulated by the pulse envelope $A(t)$ and travels at the speed of the phase velocity v_{ph}. The velocities v_{ph} and v_g need not necessarily to be equal, due to dispersion inside the cavity, which lead to different propagation speeds for the pulse envelope and the carrier electrical field. Therefore, a phase shift $\Delta\phi$ between them can be observed considering two consecutive pulses, which is often named the carrier-envelope offset phase. Note that the light intensity and the field envelope both still display periodic waveforms in the time domain, however the electric field itself is not periodic in a general

case of $\Delta\phi \neq 0$. The electrical field can be expressed as a periodic Fourier series of the optical modes $f_n = \omega_n/(2\pi)$ in the form

$$E(t) = A(t)e^{-i\omega_c t} = \sum_n A_n e^{i\phi_n} e^{-i\omega_n t}, \tag{4.1}$$

with the amplitudes A_n and phases ϕ_n of the optical mode with mode number n. The constant relation between all phases ϕ_n is another substantial property of OFCs and is referred to as phase-locking. In the special case of identical phases, one speaks of mode-locking (indicated by the grey dashed lines in Fig. 4.1 (a)), which is the origin of short pulse formation, such as in the mode-locked laser.

Figure 4.1 (b) shows an OFC in the frequency domain with a corresponding spectrum that is composed of a series of equally spaced lines

$$f_n = nf_r + f_0, \tag{4.2}$$

defined by the repetition frequency f_r and the carrier-envelope offset frequency f_0. The latter introduces a common offset $f_0 \leq f_r$ to all optical modes shifting them from exact integer multiples of f_r. The offset frequency f_0 is related to $\Delta\phi$ via the relation

$$f_0 = f_r\Delta\phi/(2\pi), \tag{4.3}$$

and therefore dispersion dependent as well. Equation 4.2 is called the comb equation and describes the completely deterministic spectrum of an OFC. Through the knowledge of one mode's absolute frequency, it is possible to ascertain the absolute frequency of any other mode, regardless of the mode number n (easily reaching up to millions). There are only two degrees of freedom, namely f_r and f_0, which both lie in the microwave range. This unique ability to define optical frequencies in terms of microwave frequencies is what originally marked the success and fame of OFCs in high precision metrological applications [140]. The beauty lies in the control of solely f_r and f_0 to stabilize hundreds, thousands or even millions of OFC lines, which can easily be achieved with mature RF technologies providing excellent accuracy. In the simplest terms, the repetition frequency controls the timing between pulses, hence the regularity of the pulse train. It allows for coarse adjustment of the OFC spectrum and represents a link of the optical to the microwave domain by nf_r. On the other hand, the offset frequency regulates the phase of the pulse train allowing for fine tuning of the frequencies. The measurement of f_r is a rather easy task, two neighbouring modes f_n and f_{n+1} create an optical beating signal at

$$f_{n+1} - f_n = (n+1)f_r + f_0 - nf_r - f_0 = f_r, \tag{4.4}$$

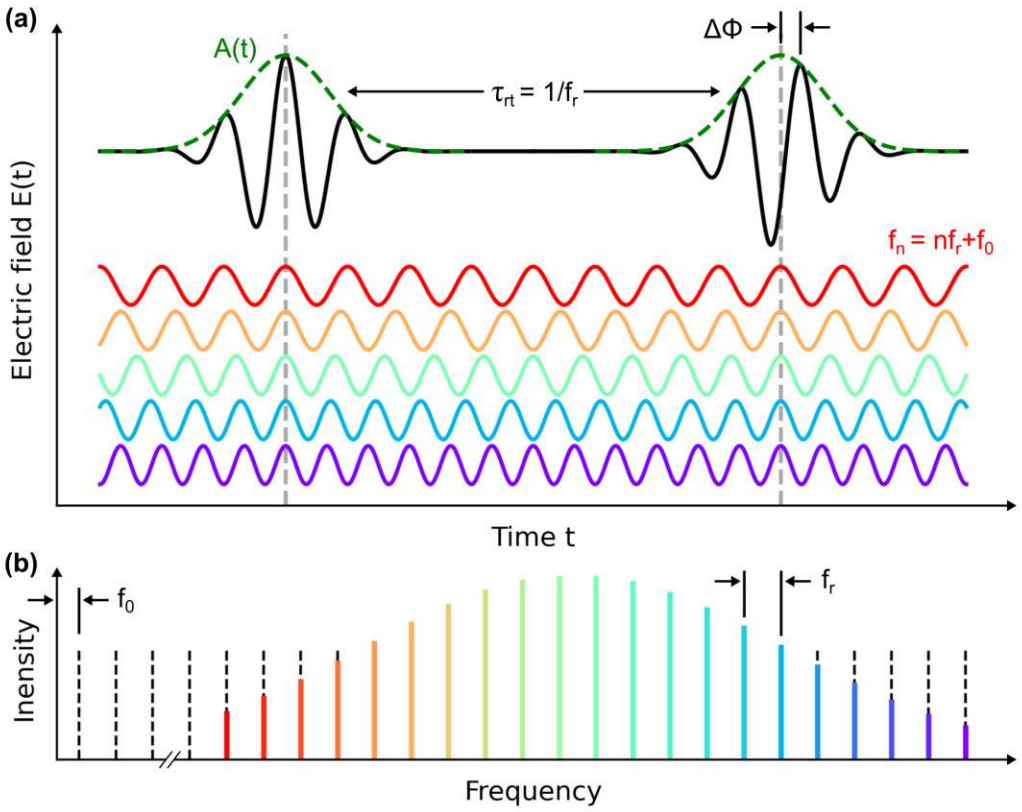

Figure 4.1: Basic principles of optical frequency combs based on mode-locked lasers. In the time domain (a) the interfering cavity modes (colored waveforms f_n) form a train of periodic pulses A(t), separated by the cavity round trip time τ_{rt}. Two consecutive pulses reveal a phase shift $\Delta\phi$ between envelope and electric field due to dispersion. The dashed grey lines indicate identical phases for the individual OFC modes leading to mode-locking. In the frequency domain (b) this translates to a set of modes, each with a corresponding frequency equal to an integer multiple of the repetition frequency f_r and an frequency offset f_0.

that can be measured with a fast photodector providing a bandwidth $\geq f_r$. Such a difference frequency measurement method is crucial for nearly all techniques utilizing OFCs and often called heterodyne optical beating. It permits the determination of the OFC characteristic frequencies f_r and f_0. Although, the direct access of f_0 is more sophisticated, since f_0 is common to each mode, and thus, not covered by the difference frequency measurement as seen in equation 4.4. As solution, the nonlinear self-referencing method, also known as f-2f-technique, was introduced [147, 148]. This involves frequency doubling (e.g. by second

harmonic generation) of the light from a mode at the red end of the comb spectrum $2f_n$ and combining it with a mode at the blue end of the spectrum at twice the frequency f_{2n}. The beating signal between them

$$2f_n - f_{2n} = 2(nf_r + f_0) - (2nf_r + f_0) = f_0 \tag{4.5}$$

yields the carrier-envelope offset frequency. Although the concept is relatively straightforward, the OFC spectrum must cover an optical octave of bandwidth in order to provide frequencies at f_n and f_{2n} as well.

4.2 Mode-Locked Frequency Combs

As mentioned at the beginning of this chapter, the first demonstration of OFCs was based on a mode-locked laser (MML) and since their origin most comb sources still rely on MLLs [149]. The cavity of the MLL sets the phase relationship between all the longitudinal modes defined by the cavity round trip time and consequently determines the repetition frequency of the laser. There are two distinct locking mechanisms in MMLs: active and passive mode-locking. Through active mode-locking, the modulation of the round-trip phase or the resonator losses is implemented via an acousto-optic or electro-optic modulator. Once the modulation is synchronized with the resonator round-trips, a regular pulse train is created. This pulse train passes through the modulator at "low-loss times", allowing to be favored over any other radiation in the cavity that arrives at "high-loss" times. When reaching a steady-state condition, the pulse saturates the laser gain leading to a round-trip gain of zero, other radiation will have a negative round-trip gain and gradually fade away. Additionally, a slight pulse shortening occurs in each round-trip due to the attenuation of the pulse wings. However, this is in balance by other pulse broadening factors, such as chromatic dispersion.

Passive mode-locking still relies on the modulation of the resonator losses, although achieved with an passive element (usually a saturable absorber) rather than an active modulator. In a passively mode-locked laser in the steady state, a short pulse is circulating in the laser cavity. Every time it arrives at the absorber element, the losses are temporarily reduced due to saturation, caused by the large intensity of the pulse. The round-trip gain provided by the laser is sufficient to compensate for these reduced losses. Light of lower intensity that hits the absorber at any other time will experience losses higher than the gain, as it is unable to cause saturation. Therefore, any weaker parasitic pulses are suppressed as well as continuous

background light. It also tends to decrease the pulse duration by reducing the wings of the circulating pulse, if the recovery time of the absorber is fast enough. Again, this pulse shortening effect will be counteracted by other lengthening effects in the steady state. In comparison, the passive locking technique can create much shorter pulses due to the fast recovery times of saturable absorbers that lead to cavity loss modulations at much higher speed than any electronic modulator can provide.

The Kerr-lens mode-locked titanium-sapphire laser (KLM Ti:sapphire) is the most popular MLL [149, 150]. It is passively mode-locked by the optical Kerr effect, which describes the dependence of the Ti:sapphire crystal's refractive index on the light intensity and is a $\chi^{(3)}$ process. This effect becomes relevant only when dealing with intense light fields, such as the pulses of a MLL. Nowadays, OFCs based on erbium or ytterbium doped fiber lasers are the most commonly used systems due to their compact, energy efficient and robust properties [151, 152]. For further information concerning OFCs produced by MLLs, one can refer to Refs. [149, 151, 153, 154].

4.3 Semiconductor and Microresonator Frequency Combs

Investigations have been conducted into various types of semiconductor lasers as sources for optical frequency combs, including mode-locked integrated external-cavity surface-emitting lasers (MIXSELs) [155,156] and quantum cascade lasers (QCLs) [157,158]. MIXSELs are semiconductor lasers with vertical emission characteristics. They are composed of alternating semiconductor layers forming three distinct sections, namely, a multi-layered, high-reflectivity distributed Bragg reflector (DBR) mirror, a gain medium containing multiple quantum wells (QWs) or layers of quantum dots (QDs), and a cap layer. Besides the on-chip mirror, another external spherical mirror is used for optical feedback, which also acts as output coupler. Such devices are driven by either optically or electrically pumping of the active region. The integration of semiconductor saturable absorber mirrors enables mode-locking in MIXELS, which results in a single integrated semiconductor chip for OFC generation.

On the other hand, QCLs make use of stacked quantum-well heterostructures that act like engineered bandgap materials as described in chapter 2.2.4. They exhibit very short upper lasing state lifetimes leading to very fast electron dynamics in QCLs, which enable modulation at frequencies above 20 GHz matching the round-trip frequencies of the involved cavities.

Thus, active mode-locking is achieved via modulating a short section of the QCL active region [158]. The short upper state lifetimes are also responsible for a very broadband four-wave mixing (FWM) process, in which four waves with different frequencies interact, resulting in two distinct cases. In the first, known as non-degenerate FWM, two waves with frequencies f_1 and f_2 translate into a pair of waves with frequencies f_3 and f_4. For the energy to remain conserved, the sum of the input waves must equal the sum of the output waves. In the second, known as degenerate FWM, which is more important for frequency comb operation in QCLs, the conversion of the frequencies follows the relations $f_3 = 2f_1 - f_2$ and $f_4 = 2f_2 - f_1$. High efficiencies can be reached when the generated waves overlap with the laser cavity modes, due to phase matching.

Optically pumped microresonator systems for OFC generation rely on the FWM effect as well [159,160]. The microresonator consists of a material providing a large nonlinearity to seed the FWM process via the optical Kerr effect. A CW single frequency pump is coupled to the microresonator providing a long interaction length for the nonlinear processes due to the high Q factor of the used cavities, which lead to long photon lifetimes within the cavity. This allows for low pump powers to be sufficient to initiate the FWM process. As a result of degenerate and non-degenerate FWM, a single-frequency pump source is converted to a comb of optical frequencies. The repetition frequency is again defined by the round trip time of the involved microresonator.
More details on the here discussed OFC sources can be found in Refs. [156,158,160].

4.4 Electro-Optic Frequency Combs

In 1993, Motonobu Kourogi and his colleagues introduced a very effective comb generation approach based on electro-optic modulation [161]. It was based on the idea of enforcing a grid of sidebands on a CW laser via electro-optic (EO) modulators [162]. The modulator was implemented inside an optical resonator and driven with an RF signal matching the free spectral range of that resonator. In this configuration, the generated sidebands experience a resonant enhancement and create sidebands themselves. Although mode-locked laser based combs eventually replaced electro-optic combs, their simplicity and deterministic nature still made them appealing. With the advancement of lithium niobate waveguide modulators developed for telecommunication purposes, a new approach for electro-optic combs was introduced around 2010 [163–165]. Instead of putting the modulator in an optical resonator, several

EO modulators can be connected in a cascade. Applying proper RF driving with controlled phase leads to the generation of additional comb lines by each modulator, which results in a flat OFC with broad bandwidth.
This thesis is largely based on electro-optic modulation and electro-optic frequency combs, therefore a detailed description is provided in the following.

4.4.1 Electro-Optic Effekt

The electro-optic effect is a type of nonlinear phenomenon that involves various effects. In general, it is a process that alters the refractive index of a material when an electric field is applied. This change of refractive index affects the phase of electromagnetic waves that propagate through the material. It can be thought of as a sort of wave-mixing between the applied electric field and the electromagnetic waves. This discussion will focus on the linear electro-optic effect (another $\chi^{(2)}$ process), since most electro-optic modulators are based on that. It is also known as Pockels effect. Another example would be the Kerr effect, mentioned earlier in the description of other OFC sources, which represents the quadratic electro-optic effect. The Pockels effect describes the linear dependence of the refractive index on an applied electric field [166]. It is only present in noncentrosymmetric materials (e.g. lithium niobate - $LiNbO_3$, the standard modulator material) since it is a second-order nonlinear process. The general relation of the electric displacement field $\mathbf{D}$ to the electric field $\mathbf{E}$ is defined by

$$\mathbf{D} = \varepsilon_0 \varepsilon \mathbf{E}, \tag{4.6}$$

with the vacuum permittivity ε_0 and the relative permittivity ε. In case of an anisotropic, lossless material it can be written via their explicit components in the form

$$D_i = \varepsilon_0 \sum_j \varepsilon_{ij} E_j \iff E_i = \frac{1}{\varepsilon_0} \sum_j \eta_{ij} D_j. \tag{4.7}$$

Here, $\eta_{ij} = (\frac{1}{n^2})_{ij}$ is the inverse tensor of ε, defined by the coefficients

$$\sum_{i=1}^{3} \sum_{j=1}^{3} \left(\frac{1}{n^2}\right)_{ij} x_i x_j = 1 \tag{4.8}$$

that describe the refractive index ellipsoid in any coordinate system x_i. The Taylor expansion of η_{ij} up to the linear order yields

$$\eta_{ij} = \eta_{ij}^{(0)} + \sum_k r_{ijk} E_k + o(E_k). \tag{4.9}$$

The 3x3x3 electro-optic tensor r_{ijk} is symmetric in its first two indices, thus the change of the refractive index can be simplified to

$$\Delta\left(\frac{1}{n^2}\right)_h = \sum_j r_{hj} E_j, \tag{4.10}$$

with the index h running from 1 to 6 in this contracted notation following the index sorting:

h	1	2	3	4	5	6
$\downarrow$	$\downarrow$	$\downarrow$	$\downarrow$	$\downarrow$	$\downarrow$	$\downarrow$
ij	11	22	33	23+32	13+31	12+21

The electro-optic coefficients r_{hj} describe the change of the refractive index related to variations of the applied electric field.

4.4.2 Electro-Optic Modulators

Every type of electro-optic modulator (EOM) relies on a phase change applied to the incident light due to the electro-optic effect. However, depending on the implementation in different setup configurations, the result can lead to various modulation schemes. The induced phase change

$$\Delta\varphi = \pi\frac{V}{V_\pi} \tag{4.11}$$

is defined by the voltage $V = EL$ associated with the applied electrical field E along the electro-optic crystal of length L and the so called half-wave voltage V_π that determines the required power to achieve a phase variation of π. It has quite a complicated dependence on the electro-optic coefficients r_{hj} of the specific crystal material and the involved waveguide structure of the EOM [167,168]. Driving the EOM with time varying RF signals, the magnitude of V_π usually increases with rising RF frequency. To get a feeling for the involved numbers, the standard EOM material $LiNbO_3$ is a good example. It exhibits electro-optic coefficients $r_{33} \sim 30$ pm/V, $r_{13} \sim 10$ pm/V and $r_{22} \sim 5$ pm/V leading to V_π values in the range of $\sim$2-11 V for an RF driving frequency around 10 GHz [168–170]. An ideal EOM should provide both, a low half-wave voltage parameter and the capability of sustaining high RF power.

The description above fits to a phase modulator (PM) and its schematic drawing is presented in Figure 4.2 (a). For the realisation of an intensity modulator (IM) the most commonly used structure is a Mach-Zehnder interferometer resulting in an often called Mach-Zehnder modulator (MZM) [171,172], a sketch can be found in Figure 4.2 (b). Waveguides are printed on an

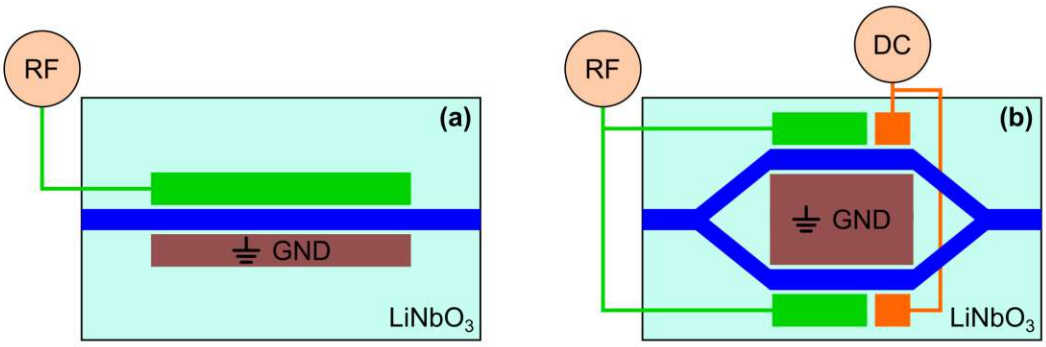

Figure 4.2: Sketch of a phase modulator (a) and an intensity modulator based on a Mach-Zehnder interferometer (b). Both waveguide structures (dark blue) with corresponding electrodes are most commonly realized on lithium niobate ($LiNbO_3$) crystals.

electro-optic material with an appropriate orientation regarding its crystallographic axes. The incident light is guided to a Y-coupler with 50/50 splitting ratio, which creates the two interferometer arms. RF electrodes are implemented so that a RF signal can be applied to both arms with opposite sign, while another set of electrodes is used for applying a static DC voltage (often called bias voltage) for an independent phase change. In both arms the electro-optic effect induces a phase change, which, after recombination by a second Y-coupler, leads to interference between the waves travelling each waveguide arm. The DC voltage is a specific feature of the MZM, which defines its operating point. Figure 4.3 presents the transmission

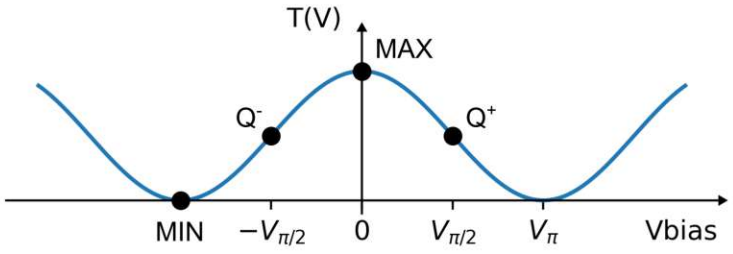

Figure 4.3: Transmission T(V) of an intensity modulator in dependence on the applied bias voltage (Vbias). Important operation points are marked: the minimum (MIN) and maximum (MAX) transmission as well as the quadrature point (Q).

curve T(V) of an IM following the applied DC bias voltage (Vbias). A DC bias of e.g. V_π induces a π phase shift between both interferometer arms minimizing the output signal of the IM. At

the so called quadrature point Q, at $V_{\pi/2}$, the transmission function becomes locally linear in first approximation, which is often used as operating point for telecommunication applications. The degrees of freedom of a MZM can be increased installing individual RF and DC drivings on both interferometer arms resulting in a dual-drive Mach-Zehnder modulator (DDMZM), which combines intensity and phase modulation within the same device [173].

4.4.3 Comb Generation via Electro-Optic Modulation

Applying a phase modulation to a monochromatic laser creates an electro-optic frequency comb (EO FC) via sideband generation. A CW laser at a carrier frequency $f_c = 2\pi\omega_c$ with an amplitude A_0 has an optical field that is described by

$$A(t) = A_0 e^{i\omega_c t}. \tag{4.12}$$

A sinusoidal electrical signal at a modulation frequency $f_m = 2\pi\omega_m$ is used as RF driving for a PM, which results in a time varying voltage

$$V(t) = V_0 \sin(\omega_m t), \tag{4.13}$$

with a peak value of V_0. This adds a time dependent phase to the CW laser signal, which can be written as

$$A(t) = A_0 e^{i\omega_c t} e^{i\Delta\varphi(t)} = A_0 e^{i\omega_c t + i\alpha\sin(\omega_m t)}, \tag{4.14}$$

via the expression for the phase change induced by a PM that is given in equation 4.11 and by defining the modulation amplitude as $\alpha = \pi\frac{V_0}{V_\pi}$. The spectrum $\tilde{A}(\omega)$ of the modulated light $A(t)$ in the frequency domain can be obtained using a Fourier transform FT,

$$\tilde{A}(\omega) = \mathrm{FT}(A(t)) = A_0\delta(\omega-\omega_c) * \left(\int_{-\infty}^{\infty} e^{i\omega_c t + i\alpha\sin(\omega_m t)}\mathrm{d}t\right). \tag{4.15}$$

This expression can be rewritten using the Jacobi-Anger expansion [174], which essentially converts plane waves in cylindrical waves,

$$\begin{aligned}\tilde{A}(\omega) &= A_0\delta(\omega-\omega_c) * \left(\int_{-\infty}^{\infty}\sum_{n=-\infty}^{\infty} J_n(\alpha)e^{it(n\omega_m-\omega)}\mathrm{d}t\right)\\ &= A_0\sum_{n=-\infty}^{\infty} J_n(\alpha)\delta(\omega-n\omega_m-\omega_c),\end{aligned} \tag{4.16}$$

with the Bessel functions of the first kind J_n. Equation 4.16 describes the spectrum of an optical frequency comb with frequencies

$$f_n = nf_m + f_c. \tag{4.17}$$

The carrier frequency f_c can be rewritten in terms of a carrier-envelope offset frequency f_0, such that $f_c = pf_m + f_0$ leading to

$$f_n = (n+p)f_m + f_0. \tag{4.18}$$

In this form, the expression is equivalent to equation 4.2 with f_m representing f_r. However, equation 4.17 is more suited for the description of EO FC, since all involved frequencies are immediately evident. The integer n numbers the generated upper and lower sidebands that are centered around the carrier frequency f_c at $n = 0$.
In expression 4.16, it is evident that the amplitudes of the EO FC lines follow the Bessel functions of the first kind J_n, and that, theoretically speaking, an infinite number of sidebands is produced. The Bessel functions J_n are solely dependent on the modulation amplitude α, thus uniquely determining the comb flatness and the number of comb lines, while the modulation frequency f_m specifies the frequency spacing between the lines.

When an IM is used instead of a PM, the induced phase changes translate to an amplitude modulation of the incident light. The same sinusoidal signal as before (expressed in equation 4.13) is now used for the purpose of an amplitude modulation. Then, the optical field of the modulated carrier wave can be written as

$$A(t) = (1 + V_0 \sin(\omega_m t))\frac{A_0}{2}e^{i\omega_c t}. \tag{4.19}$$

Using the identity for the sine function and $1/i = e^{-i\pi/2}$ yields

$$A(t) = \frac{A_0}{2}e^{i\omega_c t} + \frac{A_0 V_0}{4}e^{-i\pi/2}(e^{i(\omega_c+\omega_m)t} - e^{i(\omega_c-\omega_m)t}). \tag{4.20}$$

Again, the spectral content $\tilde{A}(\omega)$ is calculated via

$$\mathrm{FT}(A(t)) = \frac{A_0}{2}\delta(\omega-\omega_c) + \frac{A_0 V_0}{4}e^{-i\pi/2}(\delta(\omega-\omega_m-\omega_c) - \delta(\omega+\omega_m-\omega_c)). \tag{4.21}$$

In contrast to the former case, this expression includes the first set of sidebands only. Technically speaking, this represents an EO FC as well (equally spaced lines with constant phase

relation). However, three lines are usually not referred to as frequency comb. A simulation of the phase and amplitude modulation applied to a CW incident carrier wave is shown in Figure 4.4. It should be noted that in real devices any phase modulation is accompanied by a residual amplitude modulation and vice versa.

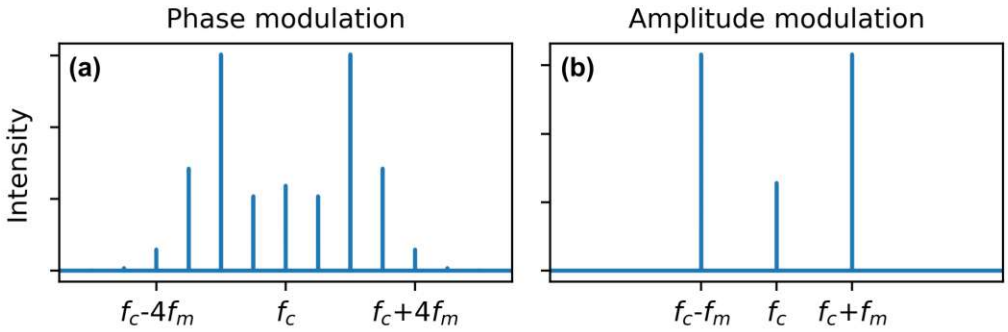

Figure 4.4: Simulation of the sideband generation via phase modulation (a) and amplitude modulation (b) applied to a CW laser.

4.4.4 Phase Noise of Electro-Optic Frequency Combs

In general, the presence of noise in any physical setup is unfavorable for its stability, and thus, for reliable applications. It is particularly problematic for the generation of OFCs, since frequency combs rely on the interference of the participating modes. When the individual modes possess too large a random phase contribution, the phase noise prevents comb formation. The more dominant the noise becomes, the more the comb spectrum will deviate from an ideal set of Dirac lines in the frequency domain. Therefore, the phase noise must be kept low.

In the case of EO FC formation via phase modulation, phase noise arises from the noise of the RF driving signal and can be considered with an adapted expression for the signal

$$V(t) = V_0 \sin(\omega_m t + \psi). \tag{4.22}$$

Here, ψ represent a static noise contribution from the RF source. Following equation 4.16, the optical spectrum of the EO FC changes to

$$\tilde{A}(\omega) = A_0 \sum_{n=-\infty}^{\infty} J_n(\alpha) e^{in\psi} \delta(\omega - n\omega_m - \omega_c), \tag{4.23}$$

where it becomes evident that the n^{th} line exhibits a phase of $n\psi$. Therefore, a linear increase of the accumulated phase noise can be observed with rising line index n. This considerations

can be extended to a non-static phase noise with low time dependency $\psi(t)$, which affects the optical spectrum in the approximation of $e^{in\psi(t)} \approx (1 + in\psi(t))$ via [167]

$$\tilde{A}(\omega) = A_0 \sum_{n=-\infty}^{\infty} J_n(\alpha)(\delta(\omega) + in\tilde{\psi}(\omega)) * \delta(\omega - n\omega_m - \omega_c), \tag{4.24}$$

with $\tilde{\psi}(\omega) = \mathrm{FT}(\psi(t))$. Also this equation shows that the phase of a comb line increases linearly with the index n and additionally is proportional to the phase noise spectrum of the RF source $\tilde{\psi}(\omega)$. It should be noted that the amplitude of the comb lines can also be affected when higher order terms in the expansion of $e^{in\psi(t)}$ are taken into account. The accumulation of phase noise can be detrimental, particularly when the integrated phase noise of each comb line is greater than π radians. This leads to a degradation of the comb's first-order coherence, resulting in the loss of its structure [175,176]. Figure 4.5 illustrates the accumulated phase noise, increasing with higher mode index for an unstabilized comb (red) and a comb with noise suppression (yellow). Both are compared to an ideal stabilized comb (green).

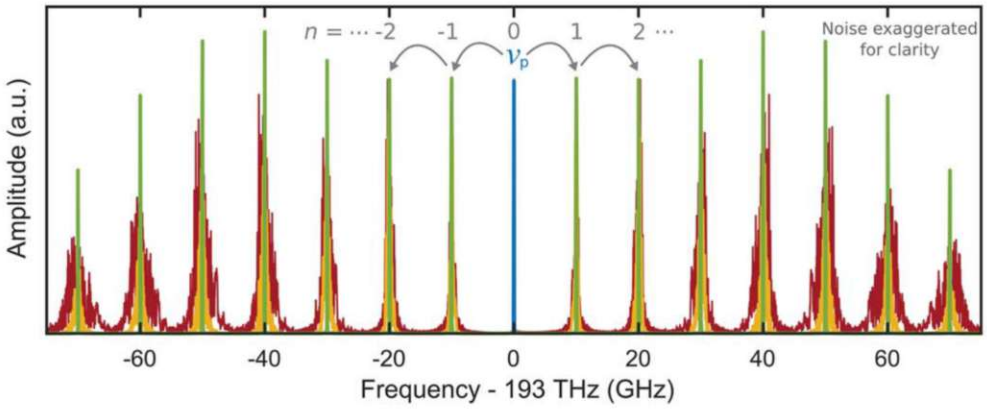

Figure 4.5: Schematic display of the phase noise accumulation on higher order sidebands of an EO FC. An unstabilized comb (red) with increasing phase noise for rising mode numbers is compared to a comb with noise suppression via mode filtering (yellow) and to an ideal stabilized comb with δ lines (green). Figure adapted from [176].

4.4.5 Electro-Optic Frequency Comb Setups

As shown above, the simplest setup for EO FC generation consists of a single EOM, schematically shown in Figure 4.6 (a). Such a setup is limited regarding the modulation depth defined

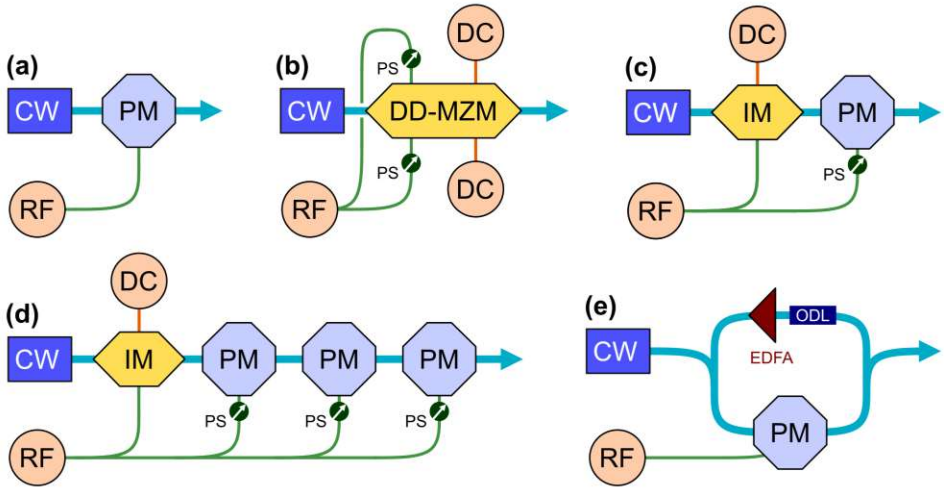

Figure 4.6: Various electro-optic frequency comb setups based on the sideband generation from a single-colour CW laser (CW) utilizing phase modulators (PM), intensity modulators (IM), a dual-drive Mach-Zehnder modulator (DD-MZM), a fiber amplifier (EDFA), an optical delay line (ODL), RF phase shifters (PS), RF and DC sources.

by the maximum RF power the EOM can handle, and also regarding the EOM bandwidth, which defines the frequency spacing of the comb. State-of-the-art lithium niobate modulators exhibit bandwidths around 40 GHz and show the potential to reach >100 GHz operation frequencies [177, 178]. An alternative presents polymer modulators, since they show a very fast electro-optic response and electro-optic coefficients exceeding those of lithium niobate by an order of magnitude [179, 180].

The only commonly used EO FC setups based on a single EOM rely mostly on dual-drive MZMs (DD-MZM) as depicted in Figure 4.6 (b). They come with a high degree of flexibility since the RF and DC signals applied to both interferometer arms can be controlled separately [181, 182]. This can be used for the generation of flat comb spectra, which is not a trivial task when considering that already a single phase modulator is an inherently nonlinear system with a non-monotonic power distribution per comb line following the Bessel functions, which leads to lines with low intensity inside the spectrum (as shown in Figure 4.4 (a)). The concept of using MZMs relies on the adjustment of both, the optical and RF phases of the two interferometer arms appropriately, in a way that produces complementary non-flat spectra, which results in a flat comb when combined at the output. This scenario resembles a joint phase and intensity

modulation at the same time and can also be achieved by placing a PM and an IM one after each other [183], as presented in Figure 4.6 (c). There are several setup configurations for flat comb generation that employ different numbers and kinds of EOMs at various driving condition [167,170].

The concept of cascading multiple EOMs (sketch in Figure 4.6 (d)) comes with additional advantages. In terms of modulation depth, a single EOM is restricted by the highest RF voltage that the modulator can handle. Since the modulation depth defines the number of comb lines, also the comb bandwidth is limited. Placing several PMs in tandem results in an increased modulation depth. In a first approximation, the rise in comb line numbers by implementing N additional PMs driven with a voltage of V is equivalent to an increase of the driving voltage of a single EOM by NV. Particular care must be taken when considering the relative phases between the modulators. In general, every EOM added to a setup increases the degrees of freedom for the spectral comb shaping to achieve different goals, such as short pulse generation or broadband EO FC generation [165,184–186].

Another kind of electro-optic setup used for the generating of EO FCs involves the implementation of an EOM within a cavity of some sort. This can be a Fabry–Perot resonator [162] or a fiber loop cavity [187] as depicted in Figure 4.6 (e). For both approaches there is a need to keep the setup in a resonant condition together with the RF driving signal, which matches the repetition frequency of the resonator. In the case of the fibered cavity, the optical delay line does the job. Although difficult to implement, these setups offer useful characteristics due to the filtering features provided by the involved resonator. Such architectures e.g. prevent the rise in phase noise for sidebands very far away from the carrier [188]. Another type of resonator that can be utilized is the whispering gallery mode resonator. When it is influenced by an electro-optic effect, it generates an EO FC as well [189]. This is especially beneficial, as the RF signal is resonating alongside the optical wave enhancing the electro-optic effect, which results in a V_π voltage significantly lower than that of typical EOMs. Despite the many benefits, cavity based setups can be quite complicated, making them rather rarely used at the moment. However, they might be especially promising for on-chip integrated EO FC solutions [190].

In summary, electro-optic combs possess a variety of advantageous characteristics that make them appealing compared to other OFC sources. First of all, they are usually created using a CW laser that can be tuned to different frequencies, resulting in the comb produced also being frequency tunable. Furthermore, the comb line spacing is adjustable in a simple way as well, since it is defined by an electronic RF signal, allowing to be changed by directly

tuning the electronic device. This large degree of tunability is not found in other comb sources, such as mode-locked lasers or microresonators, where, for the latter, tunability is even almost impossible. Another advantage of this flexibility is that it comes without the necessity of setup adaptions, due to the fact that EOMs are able to generate combs with line spacings matching their electro-optic bandwidth. For standard EOMs, these values are around 40 GHz, which means that the line spacing of EO FCs can cover the range of repetition frequencies provided by almost all other OFC sources, with the exception of microresonators that reach repetition frequencies >100 GHz [159]. Additionally, it is possible to increase the line spacing of EO FC beyond their electro-optic bandwidth limit. When adjusting the driving of the EOMs properly, one can reach the condition, such that just the odd or even number comb modes arise (which means the line spacing is doubled), or even several multiples of the driving RF frequency become possible [191, 192]. Lastly, EOMs provide a large degree of freedom for carving the comb spectral content, which realizes flat-topped OFCs or other application desired shapes.

4.5 Terahertz Frequency Combs

For a long time, there has been no direct source of frequency combs in the terahertz range. Therefore, the focus remained on down-conversion of near-infrared frequency combs by concepts such as photomixing in photoconductive antennas or optical rectification in crystals [193, 194]. The combs produced this way eliminate the carrier-envelope offset due to the difference frequency generation approach, thus, control of the repetition frequency of the near-infrared OFC is sufficient to stabilize the terahertz comb as well. Furthermore, such combs also inherit the line spacing from the original near-infrared combs, but are usually limited in terms of average power to a few microwatts. The development of novel photoconductive emitter designs including plasmonic enhancement techniques may increase this upper bound to the milliwatt level [195]. In general, this method can be applied to all of the previously discussed OFC sources. A comprehensive discussion about the down-conversion of near-infrared electro-optic frequency combs can be found in chapter 5 and presents a cornerstone of this thesis.

Nonetheless, a few strategies exist to create OFC sources emitting directly in the terahertz domain as well. The most powerful alternatives are terahertz quantum cascade lasers (QCLs), which are able to operate in a comb regime [196, 197]. They present a compact electrically pumped semiconductor OFC source that can generate a set of phase-coherent lines through four-wave mixing as mentioned in section 4.3. To realize comb formation, they rely on delib-

erate dispersion compensation techniques leading to almost octave spanning bandwidths and power levels in the milliwatt range [198].

Another semiconductor platform for THz FC generation presents the resonant-tunneling-diode (RTD) oscillator. Controlling the optical feedback that is coupled back to the RTD can lead to passive mode-locking, and therefore to comb formation [199]. Furthermore, external modulation can be used for stabilization of the repetition frequency. In contrast to QCLs, these devices provide THz comb emission at room temperature, but are restricted to $\leq$ 2 THz, so far. Below that, there are also a few Si CMOS technology solutions reaching into the terahertz range. There, THz comb generation is mostly based on multipliers [200] or bipolar CMOS devices [201].

Changing from the micro- to the macro scale, one finds THz FC emission at large-scale facilities as well. Synchrotron radiation in the so-called coherent mode produces THz pulses consisting of two interleaved OFCs [202]. The involved repetition frequencies are defined by the time between two consecutive electron bunches and the revolution period in the storage ring. The OFC nature of the THz pulses was revealed by a heterodyne receiver showing a powerful comb spanning over the frequency range from 0.1 THz to 1 THz.

5 Terahertz Opto-Electronic Light Source

Every optical sensing application relies on the availability of a convenient light source to assess the chemical composition of objects and substances. The majority of environmentally and medically relevant molecules have their fundamental optically active rotational modes in the THz region as seen in chapter 3.3.4. Using photomixing devices as terahertz sources, offers broad frequency tunability as demonstrated in chapter 3.1, which is beneficial for targeting different molecules with a single system. Chapter 4 showed the suitability of optical frequency combs (FCs) for high precision sensing. However, in the THz domain the generation of FCs is still very challenging. The predominant approaches for THz comb generation are semiconductor quantum cascade lasers (QCLs) [158, 196, 197] and down-conversion of NIR optical FCs [193]. The common feature of these approaches is an optical cavity that defines a frequency grid for the THz comb by its effective cavity length. In the case of down-conversion of femtosecond mode-locked lasers, lines are typically spaced by 40 to 250 MHz, while THz QCLs deliver FCs with a line spacing of 6–30 GHz. Due to the dependence on the cavity length, hardware modifications are necessary to change the spectral shape of such combs.

On the other hand, in chapter 4.4.5 it was demonstrated that near-infrared electro-optic frequency combs (NIR EO FC) can be controlled electronically with a large degree of freedom [170], and their parameters are solely determined by the frequency stability and phase noise of the NIR light and the radio frequency (RF) source [203]. Applications based on electro-optic FCs include e.g. self-heterodyne analysis of light sources [204, 205], high resolution spectroscopy of atomic transitions [206], and high-sensitive interference spectroscopy [4].

This chapter presents a novel method for the spectrally versatile generation of THz light and its impact on flexible THz FCs in terms of frequency range, number of comb lines and spacing between these lines. It is based on electro-optic modulation and employs difference frequency mixing in a semiconductor photoconductive antenna. The development of a THz comb source is demonstrated and its flexibility regarding the spectral content and its key parameters, namely the comb linewidth and the spectral brightness, are studied, showing that it meets the needs of chemical sensing under ambient conditions. The results presented in this chapter have been partially published in the peer-reviewed journal article Theiner *et al.*, "Flexible terahertz opto-electronic frequency comb light source tunable over 3.5 THz," Optics Letters **46**, 5715-5718 (2021).

5.1 Opto-Electronic Terahertz Generation

Among the various possibilities to generate THz light, photomixing is a very convenient solution due to the progress in the development of ultrafast opto-electronics in the field of THz photonics [87, 207], which enabled high-resolution spectroscopy of gases for example [208]. It is a mature technology already established in standard terahertz systems, and therefore, mixer devices are commercially available. The most advantageous features are their room-temperature operation, their fiber coupled optics and their frequency tunability, making them overall easy to use.

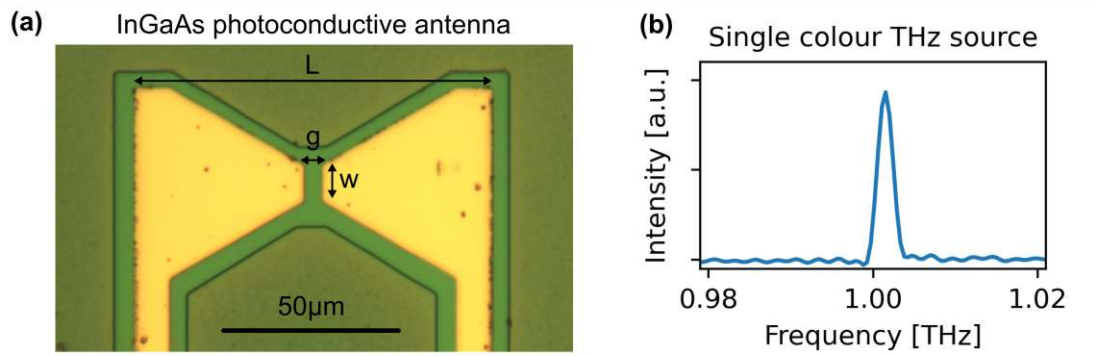

Figure 5.1: (a) Microscope picture of a bare InGaAs photoconductive antenna chip with a gap size (g) of 5 µm, a width (w) of 10 µm and an antenna length (L) of 100 µm. (b) Spectrum of the emission coming from a PCA driven with NIR lasers offset by 1 THz, measured with a Fourier transform spectrometer.

Here, mainly a commercial indium gallium arsenide (InGaAs) photoconductive THz antenna (PCA) is used as photomixing device [207]. It is packaged with bias lines, an optical fiber to guide the light to the chip, and a silicon lens to facilitate beam collimation and outcoupling. The electrodes are arranged in a bow-tie structure similar to the one displayed in Figure 5.1 (a) - a microscope picture of another bare PCA chip. Following the description in chapter 3.1, two near-infrared laser diodes are necessary to drive the PCA. A combined NIR power of 20 mW is used and focused onto the gap between the electrodes resulting in a photo current of ∼10 mA, measured when a bias of -1.5 V is applied. The wavelength offset between the two NIR laser diodes defines the resulting THz frequency by difference frequency generation and the system represents a single-colour CW THz source. Choosing an offset of 1 THz leads to the spectrum shown in Figure 5.1 (b), which is measured at room temperature with a

single scan of a Fourier transform spectrometer with a resolution of 3.0 GHz that is equipped with a deuterated triglycine sulfate (DTGS) detector. The straight-forward pyroelectric detec-

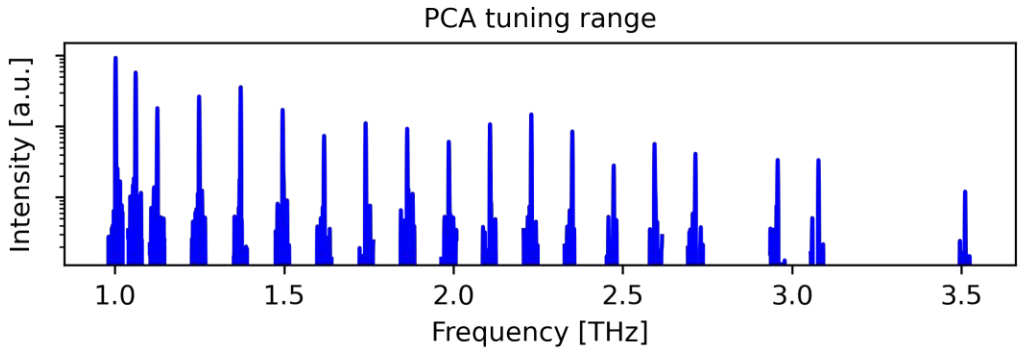

Figure 5.2: Single-colour THz spectra generated with a PCA. The emission frequency is tuned by adjusting the wavelength of one of the driving NIR laser diodes.

tion highlights the excellent quality of the THz source, since the spectrum measurement does not require any (cryogenic) cooling, coherent measurement technique or multiple scan averaging to discriminate the signal from the thermal background. The photomixer delivers a signal on the microwatt level. A continuous frequency tuning up to 3.5 THz is achieved by changing the wavelength of one of the laser diodes, which is demonstrated by a few example spectra summarized in Figure 5.2, where the response of the PCA determines the roll-off on the high frequency side. This tunability offers a great deal of flexibility, beneficial e.g.

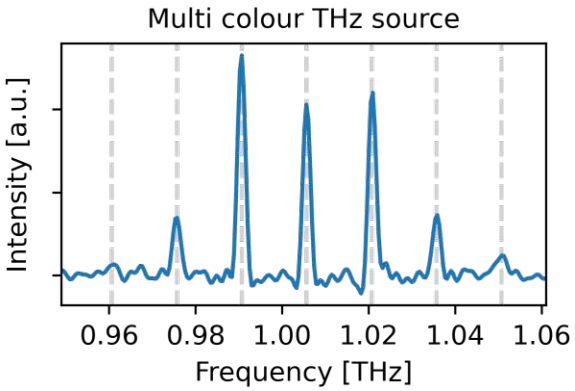

Figure 5.3: Multi-colour THz spectrum generated by difference frequency mixing on a PCA of single-colour NIR light and a multi-colour NIR spectrum generated via phase modulation. The modulation frequency of 15 GHz generates sidebands at multiples of that frequency (indicated by the grey dashed lines).

to align the emission frequency of the THz source to different absorption features within the accessible frequency window. According to chapter 4.4.3, applying a phase modulation to a single-colour laser generates optical sidebands on both sides of the carrier frequency. When such modulation is employed on one of the laser diodes that drives the PCA, the process of difference frequency mixing extends beyond the two laser carrier frequencies. It also involves the mixing of all newly generated sidebands with the single-colour line emitted by the other laser diode, leading to a multi-colour THz output, as shown in Figure 5.3. The offset of the two laser diodes determines the center frequency, while the sideband spacing is defined by the modulation frequency, indicated by the grey dashed lines. Again, changing the laser diode wavelength offset can be used to shift the multi-colour THz spectrum within the accessible frequency window.

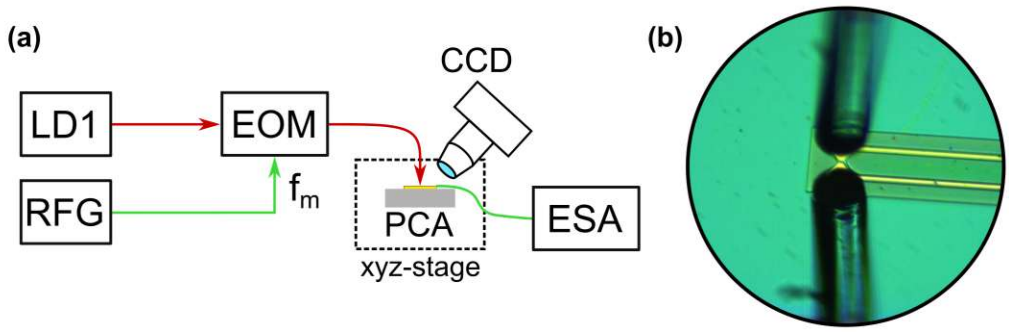

Figure 5.4: (a) Setup for the measurement of the electrical bandwidth of a PCA assembled by a single colour laser diode (LD1), an electro-optic modulator (EOM) driven by an RF generator (RFG), a motorized xyz-stage, a CCD camera and an electrical spectrum analyzer (ESA). (b) CCD picture of the lensed fiber (and its reflection) aligned to the gap of the PCA.

To investigate the electrical bandwidth of such PCA mixers, they can be used to measure the optical beating between the generated NIR sidebands. The setup is displayed in Figure 5.4 (a). The light of a single colour laser diode (LD1) is modulated by an electro-optic modulator (EOM) driven by a RF generator (RFG). A lensed fiber is used to focus the modulated NIR light onto the bare PCA chip, which introduces a modulation of the photo current exactly at the beating frequency (i.e. the modulation frequency f_m used to modulate the NIR light). This beating signal (i.e. the modulated photo current) can be read out via the electrodes and subsequently studied with an electrical spectrum analyser (ESA). A motorized xyz-stage and a CCD camera equipped with a microscope objective (50x magnification) is used to align the fiber to the

gap of the PCA. A CCD picture of the PCA with the aligned fiber (and its reflection) is given in Figure 5.4 (b). For the measurements, the PCA remains unbiased and is connected to the 50 Ω entrance of the ESA. Figure 5.5 depicts the electrical spectra of the modulated photo current signal, which is generated by the optical beating. They are measured with an ESA during a sweep of the modulation frequency f_m. A zoom onto the line around 7.5 GHz reveals a linewidth (FWHM) of 1.4 Hz. Such a narrow beating signal (below the driving laser linewidth) is possible since the optical sidebands share the same noise origins (coming mainly from the laser source and the modulator). In the beating process (i.e. a difference frequency generation) they cancel each other out. In total, an electrical bandwidth of the PCA on the range of 10 GHz can be observed, which qualifies the device for fast modulation processes.

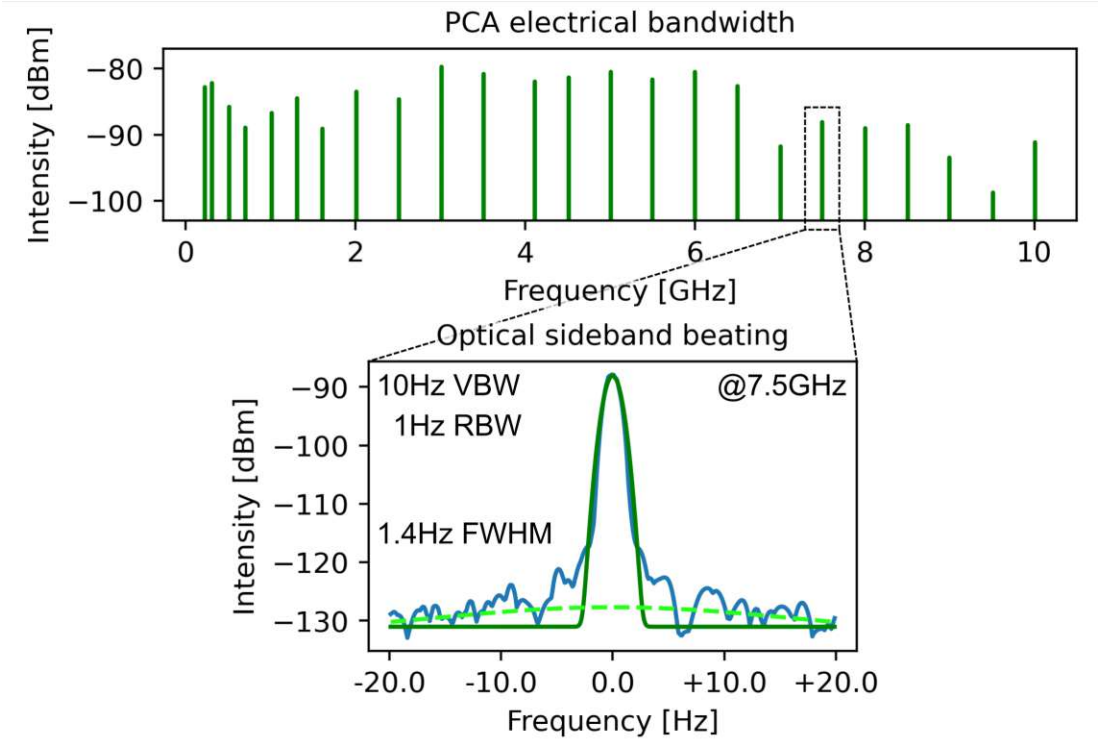

Figure 5.5: Optical beating between NIR sidebands, measured with a PCA and an electrical spectrum analyser for different modulation frequencies. The RF-beating spectra are fitted with two Gaussians to determine the beatnote linewidth (dark green) on the background (light green) as displayed in the zoom-in. The scanning time is set to 1.8s.

5.2 Terahertz Opto-Electronic Frequency Comb Method

When a phase modulation is applied to a single-colour NIR laser of frequency f_1, the newly generated optical sidebands $f_1 \pm if_m$ share by definition a common phase relation, and thus, form a high-quality frequency comb [170]. The spectral characteristics of the newly generated NIR comb follow equations 4.14-4.16. Rewritten, the expression for the modulated signal reads with the identity $\omega = 2\pi f$ as

$$\begin{aligned} A(t) &= A_0 \cos(\omega_1 t + \phi_m \cos(\omega_m t + \varphi')) \\ &= A_0 \left(J_0(\varphi_m) \cos(\omega_1 t) + \sum_{i=1}^{\infty} J_i(\varphi_m) cos(\omega_1 t \pm i\omega_m t \pm i\varphi') \right), \end{aligned} \tag{5.1}$$

where it is evident that the driving parameters of the phase modulation (frequency ω_m, amplitude φ_m and phase φ') completely define the comb's spectral shape via the Bessel functions of the first kind J_i.

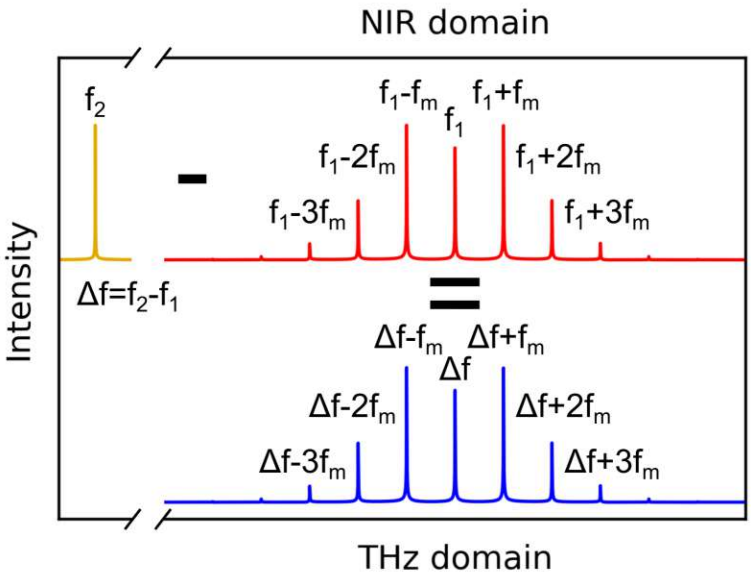

Figure 5.6: Principle of THz electro-optic frequency comb generation. Optical sidebands ($f_1 \pm if_m$) are generated from a single laser line f_1 via phase modulation forming a NIR FC. Difference frequency mixing with a second single mode laser (f_2) translates the NIR FC to the THz domain ($\Delta f \pm if_m$).

The conversion to a THz comb can be done by mixing the NIR EO FC with a second monochromatic NIR laser in a photoconductive THz antenna. The THz spectrum results from the

difference frequency mixing of all involved NIR spectral lines, which is illustrated in Figure 5.6. Therefore, the proposed method for the generation of terahertz opto-electronic frequency comb light (TOFL) is basically a merging of the two mature technologies mentioned above — photomixing of NIR light for the generation of terahertz electromagnetic waves and NIR EO FC generation. In that way, the flexibility of EO FCs can be directly transferred to THz FCs.

5.2.1 Experimental Setup

In Figure 5.7, the setup of a TOFL source is depicted. The signal from a single-mode, fiber-

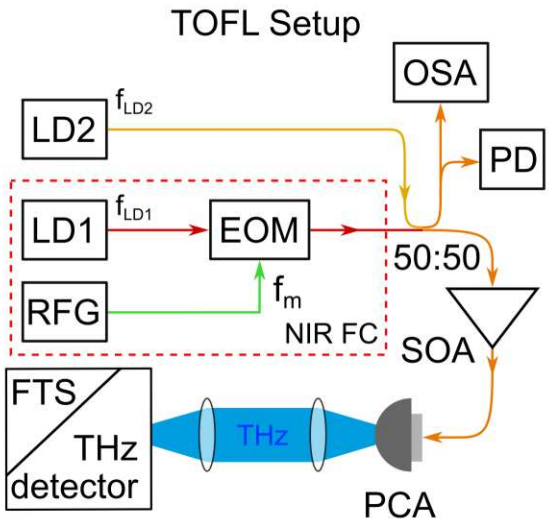

Figure 5.7: Sketch of the THz FC setup. A NIR EO FC source based on a fixed-wavelength diode laser (LD1) and an EO phase modulator (EOM), driven by an RF generator (RFG) and a tunable diode laser (LD2) as well as a 50:50 fiber combiner, a semiconductor optical amplifier (SOA), an optical spectrum analyser (OSA), and a photodiode (PD) are shown. A photoconductive antenna (PCA) acts as NIR to THz converter. The generated THz beam is guided to a THz power detector or a Fourier transform spectrometer (FTS).

coupled, temperature stabilized NIR laser diode (LD1) emitting at 1555 nm (equivalent to f_{LD1}) is fed to a fiber-coupled electro-optic phase modulator (EOM) to generate a custom NIR electro-optic FC with line spacing f_m. The EOM is driven by an RF source (RFG) with adjustable signal parameters (frequency, phase, and output power). By controlling the RF power fed to the modulator, the achievable phase shift is defined. Thereby, the phase and amplitude

of the modulation frequency uniquely determine the final THz comb shape. The wavelength tunability of a second NIR diode laser (LD2) at f_{LD2} enables the shift of the original NIR FC into the THz domain with an adjustable center frequency determined by the offset of the two laser diodes ($\Delta f = f_{LD2} - f_{LD1}$). Both NIR beams are combined in a polarization-maintaining fiber combiner (50:50) and boosted to 20 mW by a semiconductor optical amplifier (SOA). Monitoring of the involved NIR radiation is provided by the photodiode (PD) and the optical spectrum analyser (OSA). The combined NIR radiation is fed to a photoconductive antenna (PCA) acting as opto-electronic converter. There, the optical beating between the NIR spectral lines induces a photo current modulation at THz frequencies, which drives a resonant antenna structure, and thus, emits THz waves into free space. The generated THz FCs are

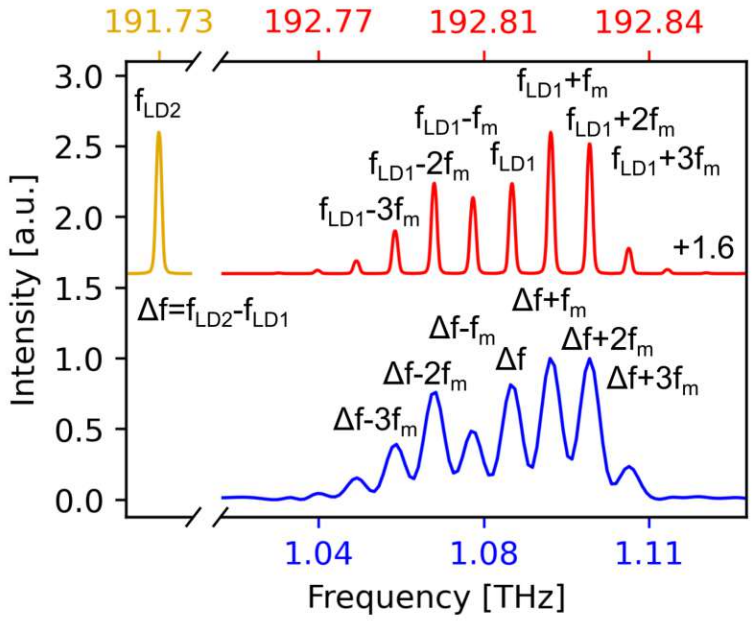

Figure 5.8: Spectra of the NIR light driving the PCA in the TOFL source and spectrum of the output THz FC. The spectra are measured in the NIR with the OSA (1.2 GHz resolution) and in the THz with the FTS (3.0 GHz resolution), they are offset for clarity. The NIR FC is generated with a modulation frequency of 8.0 GHz and a modulation amplitude of 0.68π.

either measured by a Fourier transform spectrometer (FTS) or a Goley cell acting as room temperature THz power detector. Example spectra of the involved NIR and THz beams are shown in Figure 5.8. They verify that the THz FC spectrum, measured with the FTS ($\sim$3.0

GHz resolution), represents an accurate replication of the NIR FC spectrum, measured with the OSA (∼1.24 GHz resolution). It also becomes evident that a simple harmonic RF driving of a single phase modulator already allows for covering a 100 GHz band with several equidistant frequency comb modes.

5.2.2 Spectral Synthesis

The TOFL source provides full electronic control over the spectral content of the THz FC. Since LD2 is tunable in its emission wavelength, the position of the comb within the accessible THz frequency window can be freely chosen. Its spectral coverage is presented in Figure 5.9 cov-

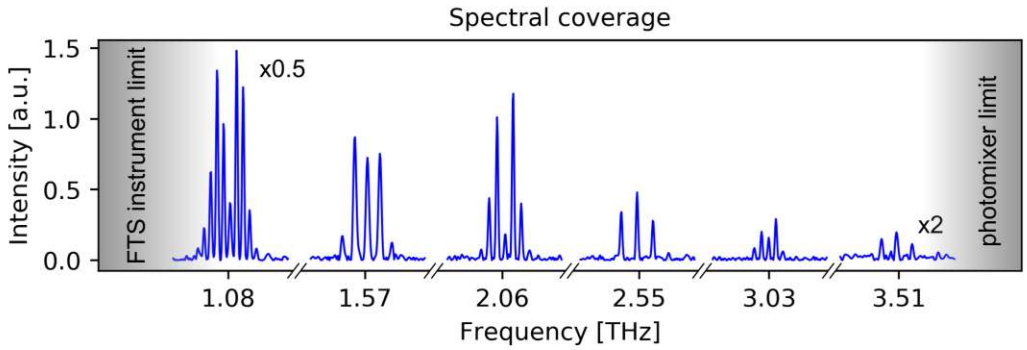

Figure 5.9: Spectral coverage of the opto-electronically synthesized THz FC spectra achieved by detuning the NIR laser diode LD2 and registered by a FTS with a resolution of 3.0 GHz. Phase modulation amplitudes and frequencies used for the comb generation are listed in Table 5.1.

Table 5.1: Parameters for the THz FC generation shown in Figure 5.9.

$f_{LD2} - f_{LD1}$ [THz]	frequency f_m [GHz]	amplitude φ_m [radians]
1.083	9.0	0.66π
1.573	17.0	0.38π
2.062	11.0	0.47π
2.547	22.0	0.19π
3.030	10.0	0.55π
3.507	21.0	0.44π

ering the range of 1.1-3.5 THz, where the limitation on the high frequency side is determined by the response of the utilized photoconductive antenna [207]. The shown spectra are limited on the low frequency side as well, due to the bandwidth of the beamsplitter in the FTS instrument. To demonstrate the flexibility of the comb's spectral content, the THz FCs are generated

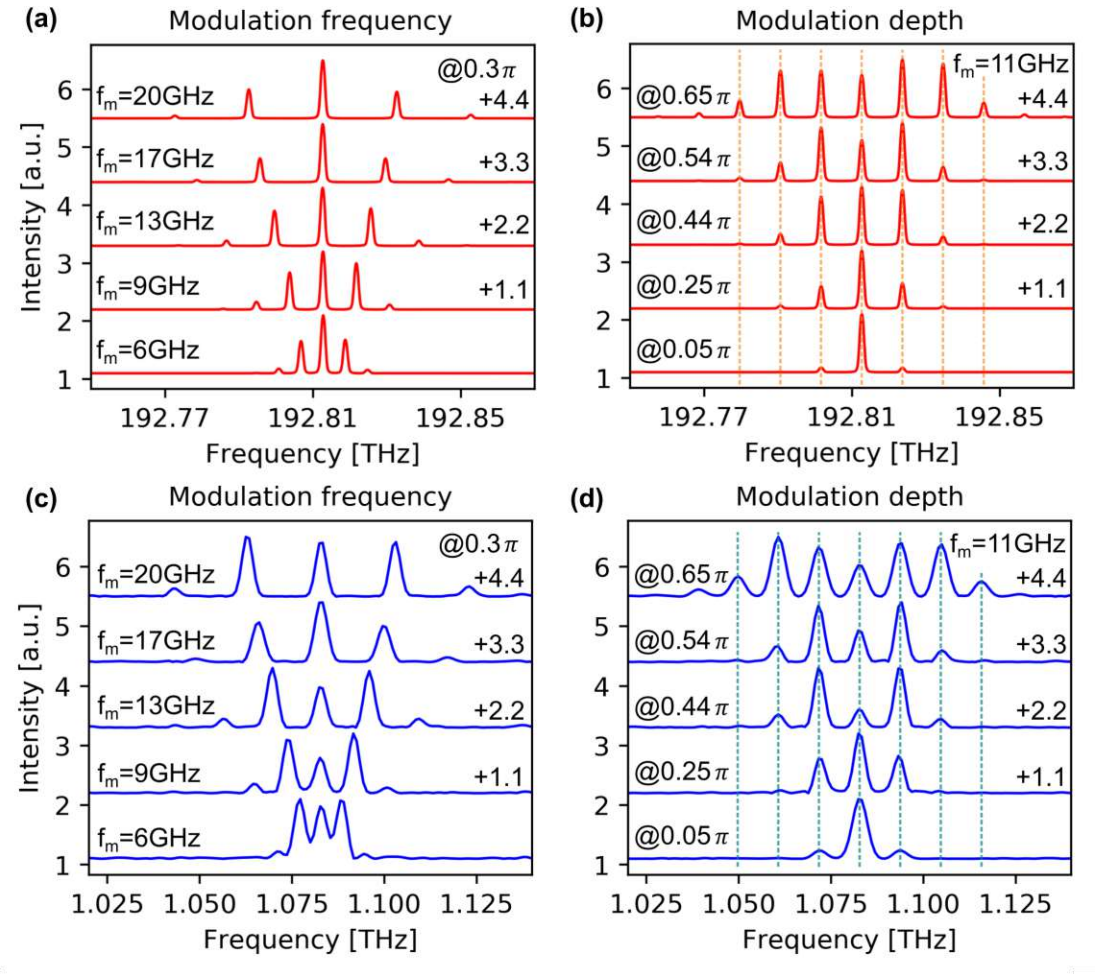

Figure 5.10: Parametric space for the comb generation. The electronic control of the comb design is shown in the NIR (a,b) and in the THz (c,d) range. The spectra are offset for clarity and the dashed lines serve as guide for the eye.

using various combinations of phase modulation conditions (i.e. frequency f_m and amplitude φ_m), while gradually tuning the emission frequency of LD2 by 2.5 THz. An overview of the used modulation parameters is given in Table 5.1. Switching between all these combs can be done almost instantly, the main limitation presents the time required for the wavelength

readjustment of laser diode LD2. The all-electronic, flexible control of TOFL spectra is further illustrated in Figure 5.10 for a fixed frequency offset of ∼1 THz between the laser diodes LD1 and LD2. It summarizes the available parametric space of the modulation parameters that shape the NIR FC in terms of line spacing, number of comb lines and power distribution between the lines that is achievable with a single phase modulator. The efficient transfer of the original NIR combs to the THz region is emphasized by the comparison of the comb spectra in both frequency domains.

5.2.3 Terahertz Source Linewidth Study

Besides the spectral coverage and the design flexibility, the linewidth of the generated THz FC lines (which corresponds to the integrated phase noise) is of significant importance for the practical use of a TOFL source. An actual linewidth measurement requires a detector much faster than the Goley cell or a spectrometer with much better resolution (in the MHz range) than a FTS with typical values on the order of several GHz. However, two approaches are presented in the following to shine some light on the topic. One in the NIR range investigating the optical signals driving the photoconductive antenna. And another one in the THz region examining the THz comb lines directly.

Near-Infrared Domain

Following the theory of driven oscillators, the linewidth of the oscillator frequency corresponds to the phase noise of the driving force. Hence, the linewidth of THz FC lines emitted by the TOFL source should be given by that of the beating NIR frequencies. A NIR EO FC is derived from LD1 by phase modulation and fiber-coupled to an ultrafast InGaAs photodiode (PD) as depicted in the setup schematic in Figure 5.7. Here, the second laser LD2 is turned off to measure solely an intermodal beating between the NIR comb lines. The modulation frequency is chosen, so that all the resulting beating signals fall within the bandwidth of the photodiode with an active area diameter of 80 µm. The photodiode is connected to the 50 Ω entrance of a 30 GHz bandwidth electrical spectrum analyser for signal analysis. Figure 5.11 (a) depicts the optical spectrum of the measured NIR comb and (b) shows the investigation of the intermodal beating between the carrier (i.e. the central comb line) and the first (dark green) and seventh (light green) sideband, respectively. Both reveal a linewidth on the Hz level, which is dominated by the phase noise contributed by the RF equipment and the phase modulator. This demonstrates that the comb lines only marginally deteriorate with increasing line index as described in chapter 4.4.4. Thus, the line broadening that comes with the frequency multiplication via phase modulation is much

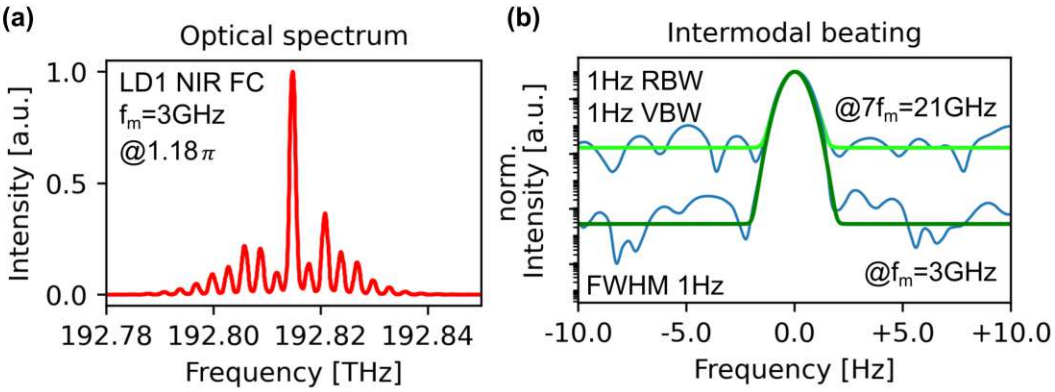

Figure 5.11: (a) Spectrum of LD1 NIR FC formed by a phase modulation frequency of 3.0 GHz and a modulation amplitude of 1.18π. (b) Intensity-normalised intermodal beating of the central comb line with the first (dark green) and seventh (light green) comb sideband. The beating signals are measured with a high speed photodiode and recorded with an electrical spectrum analyser and a scanning time of 1.8s.

smaller than the system phase noise. Since the presented implementation limits the output to somewhat tens of comb lines, this effect is negligible. In a first estimation THz FCs with up to one hundred lines can be generated before this noise source will significantly increase above the system noise. Therefore, it is proven that the phase fluctuations of both, the laser diode LD1 light and the RF source, are coherently transferred to all comb lines. This behaviour guarantees that every THz comb line resulting from the photomixing of the NIR EO FC with the light from the second diode laser will feature similar phase noise characteristics. To estimate the linewidth of the generated THz FC lines themselves, the optical beating of the two laser diodes is measured. Their frequencies were offset by 1 GHz, and the phase modulation frequency f_m was set to 3 GHz as shown in Figure 5.12 (a). Consequently, all resulting optical beatings (i.e. the sub-THz FC lines) fall within the bandwidth of the photodetector. From Figure 5.12 (b), one finds that the three neighbouring comb lines exhibit similar linewidths below 1 MHz, which can be considered as a conservative estimate for the lower bound for the THz comb linewidths, although not the THz but the optical beatnote is measured. This value reflects the phase noise contributions from the diode lasers, the RF generator and the used photodetector signal chain. The electronic noise and frequency response of the opto-electronic converter PCA, as well as the mechanical vibrations of the THz emitter/detector opto-mechanics, can contribute to an excessive phase noise. Therefore, a linewidth study directly in the THz domain is necessary.

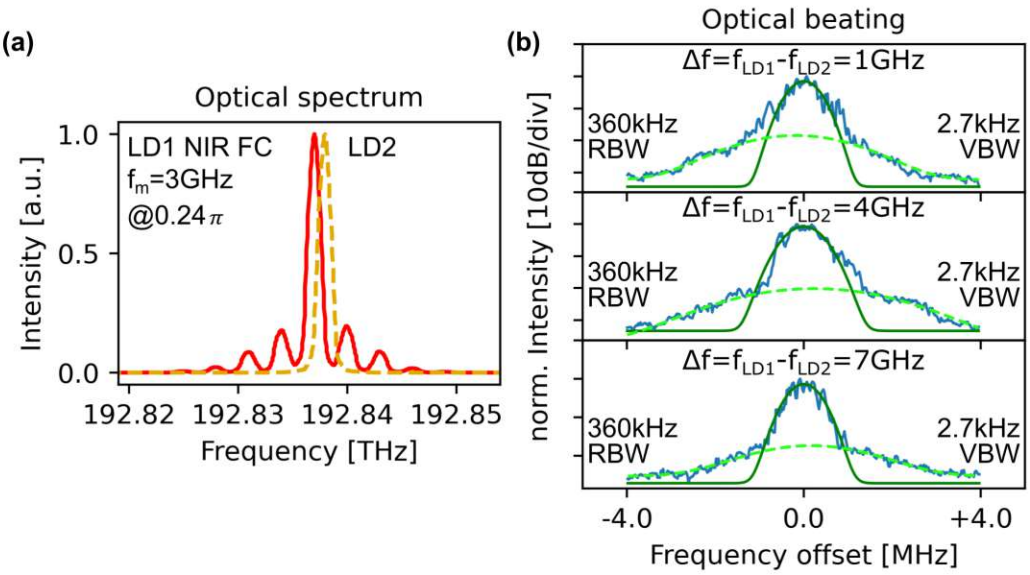

Figure 5.12: (a) Spectrum of the LD1 NIR FC formed by a phase modulation frequency of 3.0 GHz and a modulation amplitude of 0.24π (red) together with the spectrum of the single mode LD2 (yellow). (b) Intensity-normalised optical beating of LD2 with the modulated output of LD1 recorded with an electrical spectrum analyser and a scanning time of 0.2s. The RF-beating spectra are fitted with two Gaussians to determine the beatnote linewidth (dark green) on the background (light green).

Terahertz Domain

As mentioned above, the FTS cannot resolve the true THz comb linewidth. Instead, the linewidth is studied via the tuning of one comb line trough a molecular absorption region as illustrated in Figure 5.13. Scanning of a single THz comb line corresponding to a frequency of $f_{LD2} - f_{LD1} + f_m$ through an absorption line of ammonia (NH_3) is done by sweeping the modulation frequency f_m of the phase modulator (i.e. varying the comb spacing) while keeping the modulation amplitude φ_m constant. For convenience, the phase modulation depth is chosen to concentrate the THz power to the selected comb line. All the other comb lines are kept outside of the chosen absorption frequency window. The optical power of all the comb lines falls on a single THz detector and the experiment relies on the assumption that only the chosen comb line is in resonance with the molecular transition. Therefore, in a transmission measurement only the fraction of the total THz power, corresponding to the specific FC line that interacts with the ammonia transition, is attenuated.

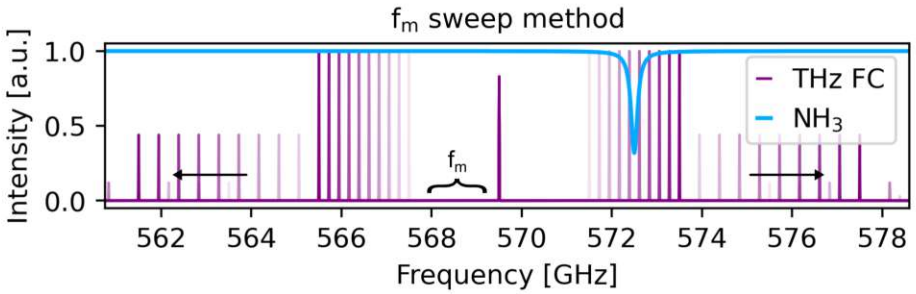

Figure 5.13: Schematic depiction of the f_m sweep method. Adjustment of the RF modulation frequency f_m sweeps a single comb line (purple) through the absorption region of NH_3 (blue).

The far-infrared active rotational transition J=0→1 of the NH_3 molecule at 572.498 GHz (19.09648 cm^{-1}) was chosen for the linewidth study and measured in a 70 mm stainless-steel home-made gas cell with quartz windows. The result of a room temperature (296 K) transmission measurement of pure NH_3 (N3.5 purity) at a gas pressure of 6 mbar is shown in Figure 5.14 (a). A Lorentzian fit (red line) is used to extract the linewidth of 165 MHz of the mainly pressure broadend absorption line. Figure 5.14 (b) summarizes the linewidths extracted from several measurements with rising NH_3 gas pressures up to 20 mbar. The individual measurements can be found in the appendix A.1 of this thesis. As expected, a transition linewidth broadening can be observed with increasing pressure values. All experimentally determined linewidths follow the broadening values obtained from the HITRAN database [133] with somewhat increasing error margins for higher pressure values. From the experimental data a pressure-induced broadening of 30.69±2.65 MHz/mbar can be determined, while the calculations based on the HITRAN database yield a value of 29.65 MHz/mbar, which lies within the error margins of the data.

The experimentally obtained spectral profile of the absorption line, as shown in 5.14 (a), is a result of the convolution of the THz comb line with the collision-broadened rotational transition and their values indicate that the linewidth of the THz FC teeth is well below 10 MHz. Otherwise, additional broadening coming from the convolution would be seen, leading to linewidths deviating from the theoretical values. This marks a conservative number as upper bound for the linewidth of the THz comb line, since the beating of the laser diodes did not exceed 1 MHz at all. Nevertheless, 10 MHz is still a very good value for a system consisting of two completely independent laser sources that use only a temperature stabilisation of the cavity. The observed multi-MHz linewidth of the THz FC teeth is assigned to a residual relative

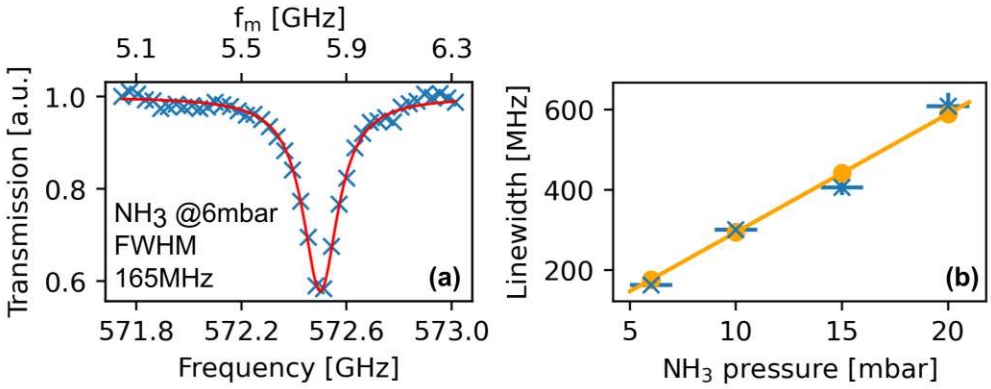

Figure 5.14: NH_3 molecular rotational transition at 572.498 GHz (19.09648 cm^{-1}). (a) Transmission (blue crosses) measured at a pressure of 6 mbar and a temperature of 296 K (red line - Lorentzian fit used for linewidth determination). (b) Measured pressure broadening of the absorption line (blue crosses) compared to the linewidth values (yellow dots) obtained from the HITRAN database [133].

frequency drift of the semiconductor diode lasers during scanning through the frequency window of the molecular transition. Indeed, a maximum 10 MHz broadening of the optical beating signal between both laser diodes can be observed with the RF signal analyser during a time window of a minute (which corresponds to the maximum cumulative frequency error during the transmission data acquisition as well). A linewidth of <10 MHz is already attractive for many sensing applications. However, there are a few possibilities to achieve a deep sub-MHz frequency precision that include locking the diode lasers to a reference absorption line [209] or to a NIR FC [210, 211], electro-optical frequency shifting [212] and mode filtering [213]. It should be noted that even Hz level frequency precision can be reached with THz generation based on NIR FCs [210, 211, 213, 214]. This precision comes with large complex setups and is not required for the majority of potential THz sensing scenarios.

5.3 Frequency Comb Parametric Space Expansion

The above presented synthesized THz FCs exhibit elementary spectral designs due to the restriction to a single EO phase modulator driven by a simple harmonic RF signal. Complex comb spectra can be realized applying more advanced modulation schemes including a chirped RF waveform driving a phase modulator [206] or optimizing the driving parameters of a dual-

parallel Mach-Zehnder modulator [215]. In the following, a few examples mainly based on the discussion in chapter 4.4.5 are presented to get a feeling for the flexibility that comes with a modular TOFL setup using different kinds and numbers of EO modulators in various configuration.

5.3.1 Cascading Electro-Optic Modulators

One approach to extend the spectral design flexibility represents the implementation of multiple EO modulators in tandem with different driving conditions [167,170]. Generally speaking,

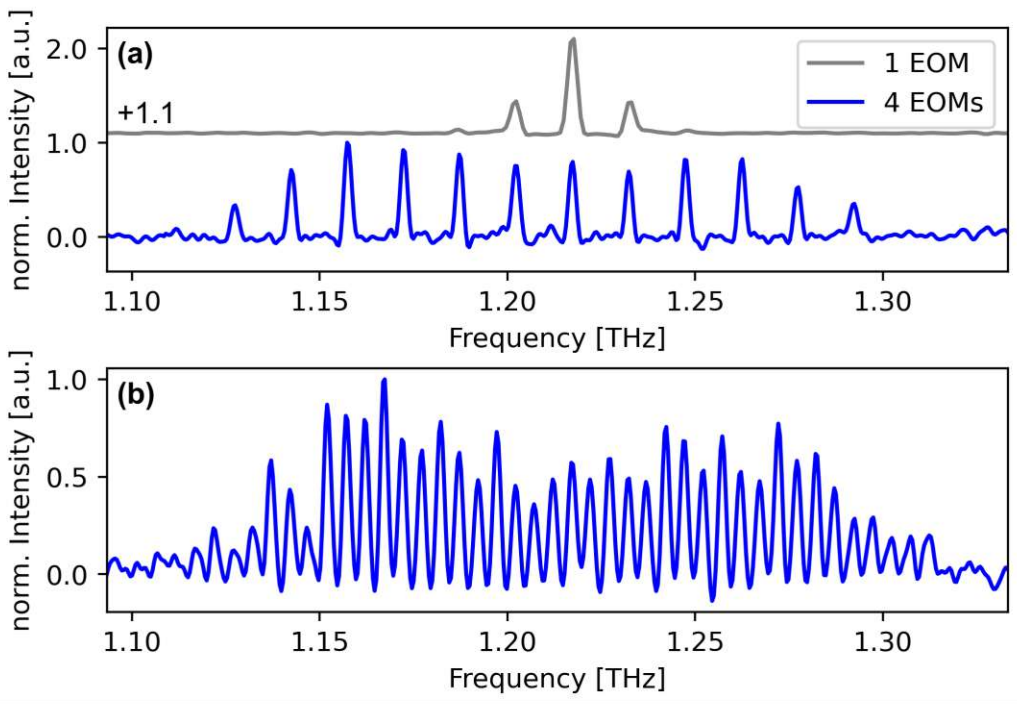

Figure 5.15: (a) Comb broadening and flattening shown by the comparison of THz FC spectra generated with a single phase modulator (grey) and 2 phase and intensity modulators (blue), respectively. The spectra are offset for clarity. (b) Example of a broad THz FC covering 200 GHz with a line spacing of 5 GHz generated with 2 phase modulators and 2 intensity modulators implemented in series.

the (harmonic) RF frequency applied to an EO phase modulator defines the basic line spacing of a THz comb generated with a TOFL setup. Implementing a second EO phase modulator

driven at the same frequency can be used to increase the total modulation depth leading to broader comb spectra. Intensity modulators are either applied to effectively flatten the comb when driven at the same frequency as the phase modulators or employed to change the comb spacing when the driving signals are subharmonics of the phase modulator signals. When dealing with multiple modulators, it is crucial to take care of the relative phases between them. Figure 5.15 (a) presents a comparison of the THz FC spectra generated with a 15 GHz line spacing, once with the elementary version of the TOFL setup based on a single EO phase modulator (grey) and another one with the expanded setup implementing two phase and intensity modulators in series (blue). Both spectra are recorded using the same RF driving parameters applied to all modulators. In the multi modulator case, the relative RF phases are carefully adjusted resulting in a substantially broadening and flattening of the comb compared to the single modulator spectrum.

Another example of a broad and relatively flat THz FC is given in Figure 5.15 (b). It consists of >40 comb teeth spaced by 5 GHz all within a 10 dB intensity variation and covers a band of 200 GHz. Four EO modulators are used for its generation. Two phase modulators and one intensity modulator driven are driven at 15 GHz to form a FC with a 15 GHz basic line spacing with increased modulation depth and comb flattening. Another intensity modulator driven at 5 GHz adds subharmonic bands to each FC line resulting in the total comb spacing of 5 GHz.

In chapter 3.3.2, it was specified that the rotational spectrum of light molecules usually consists of a set of equally-spaced transition lines. Therefore, the increased flexibility for generating THz combs offered by cascaded EO modulators opens the possibility to synthesize THz spectra that match chemical fingerprints of those molecules. Several comb teeth can be aligned to different rotational transitions simultaneously. In the view of sensing applications, targeting a whole series of spectral lines of an analyte instead of single transitions, promises a huge increase in sensitivity and accuracy. Figure 5.16 displays a few examples of THz FC spectra designed for specific potential sensing scenarios. The spectrum in (a) is synthesized with 2 phase and intensity modulators driven at 12.133 GHz, which represents the basic frequency spacing between rotational transitions of carbonyl sulfid (OCS), a biomarker for human breath diagnostics. A comb spectrum below 1 THz cannot be measured due to the FTS limitations. For demonstration purposes, the spectrum was generated and measured around 1 THz and subsequently aligned to the OCS fingerprint spectrum (calculated from the HITRAN database [133]) in the data processing. For any real experimental application, the comb center can be easily shifted from 1 THz to 0.5 THz via adjustment of the LD2 wavelength as described before, which will not alter the spectral shape of the comb at all. A similar scenario is presented in (b), where

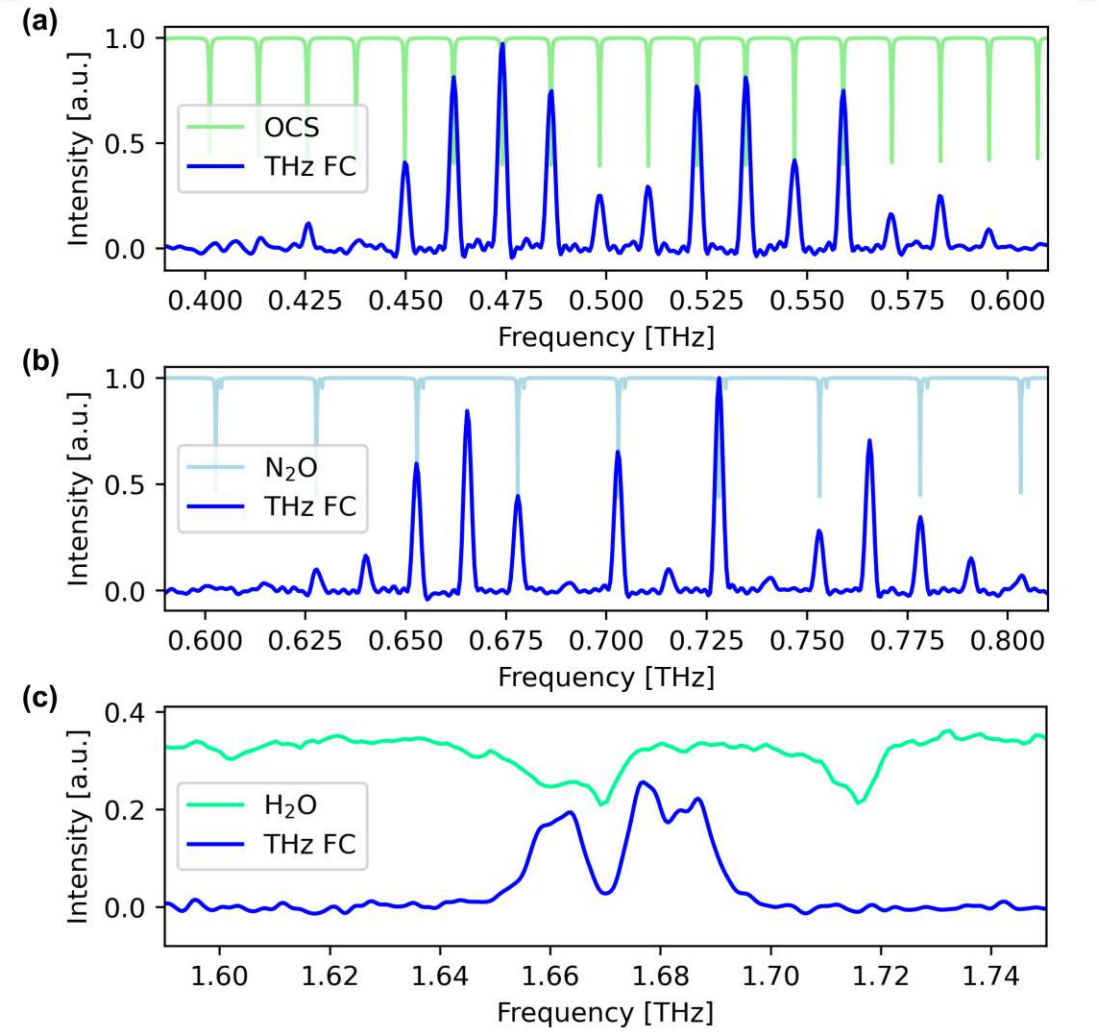

Figure 5.16: THz FCs (blue) designed to match the chemical fingerprint spectra of OCS (a) and N_2O (b) and to locate H_2O absorption lines (c), respectively.

the comb is aligned to nitrous oxide (N_2O), an important greenhouse gas. The rotational lines of N_2O are separated by $\sim$25 GHz, which is beyond the bandwidth of the used RF equipment. Nevertheless, alignment of the comb teeth to the fingerprint spectrum (again calculated from HITRAN) can be achieved by driving the EOMs at 12.535 GHz and adjusting the DC bias of the intensity modulators (i.e. changing its working points). The zero transmission point as well as the maximum transmission point result in combs with doubled repetition frequency, since just the odd or even numbered comb teeth are generated, as was mentioned in chapter 4.4.5. Here, the spectrum deviates from the perfect theoretical scenario, as not all odd numbered comb

teeth are suppressed due to unwanted subharmonics generated by the RF signal generators used. Still, most of the THz power is distributed over several rotational transitions of N_2O and the plot serves as demonstration of the concept and emphasizes another degree of freedom that comes with multiple modulators. Again, this spectrum was recorded around 1 THz and frequency shifted in the data processing.

In Figure 5.16 (c), a different approach is chosen. The generation of a dense spectrum with a line spacing of 1.5 GHz, which lies below the resolution of the FTS instrument ($\sim$3 GHz), results in a broad THz spectrum, in which the single comb teeth cannot be resolved. Such a broad spectrum can be utilized to identify the position of absorption lines, like the one displayed for water (H_2O) around $\sim$1.67 THz. The water spectrum is recorded with the internal Globar source of the FTS instrument, measuring the water vapor content in the ambient air. It would also be possible to conduct a proper investigation of absorption lines that are broader than the resolution of the spectrometer. All this together highlights the flexibility of the system and its potential for different sensing methods and scenarios.

5.3.2 Dual Frequency Comb Generation

In chapter 2.1.1 it was mentioned, when it comes to sensing with frequency combs, the generation of dual combs is of high interest due to the emerging, fast and efficient dual comb spectroscopy technique. Two NIR frequency combs with slightly different line spacing can be

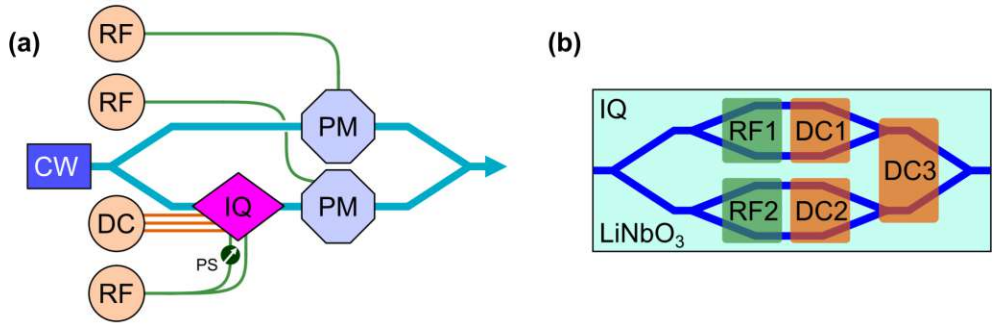

Figure 5.17: (a) Near-infrared dual frequency comb setup based on a CW laser diode, an IQ modulator, two phase modulators (PM) and RF and DC drivings. (b) Schematic structure of an IQ modulator.

generated with the electro-optic architecture displayed in Figure 5.17 (a). The light of a CW laser diode is split into two arms, each equipped with a phase modulator (PM) generating the

two combs. For a proper application scenario, a frequency offset between them need to be introduced, resulting in distinguishable heterodyne beatnotes between the pairs of comb teeth in the RF domain, as will be shown in the following. For this purpose an IQ modulator is installed in the setup, which is schematically shown in Figure 5.17 (b). It is based on a dual-parallel Mach-Zehnder interferometer (MZI) structure in order to allow modulation of both the phase and amplitude of a carrier signal and is commonly used for advanced optical transmission schemes in telecommunication applications [216, 217]. One RF signal is applied for the modulation in each MZI and accompanied by a DC signal for adjusting the phase between both interferometer arms. A third DC signal can be used to control the phase between the two MZI outputs before recombining the signal. This device is used to generate a single sideband with suppressed carrier (SSB-SC), essentially introducing the requested frequency shift to the carrier before generating the second comb in one of the arms of the setup. Figure 5.18 presents an

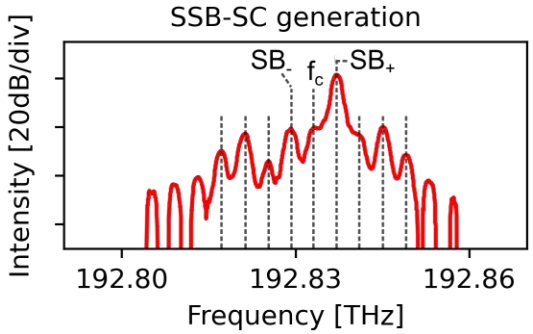

Figure 5.18: Optical spectrum of a single sideband (SB_+) with suppressed carrier (f_c) generated by an IQ modulator driven at 4 GHz. Measured with an optical spectrum analyser.

example of such a frequency shift. A modulation frequency f_m of 4 GHz generates an upper sideband ($SB_+ = f_c + f_m$), while the carrier (f_c) and all other frequency components are suppressed by ∼20 dB. Shifting the phase between both MZIs by π (i.e. adjusting the DC3 bias) changes the scenario to the lower frequency side ($SB_- = f_c - f_m$).

In Figure 5.19 (a) the spectrum of a NIR dual comb DFC (red) is presented together with the spectra of the individual combs FC1 (grey) and FC2 (black), generated with the setup described above and measured with an optical spectrum analyser. The PMs generating FC1 and FC2 are driven with modulation frequencies of 15 GHz and 15.7 GHz, respectively. For the frequency shift of FC2, the IQ modulator is driven at 4 GHz offsetting the central frequency of both combs

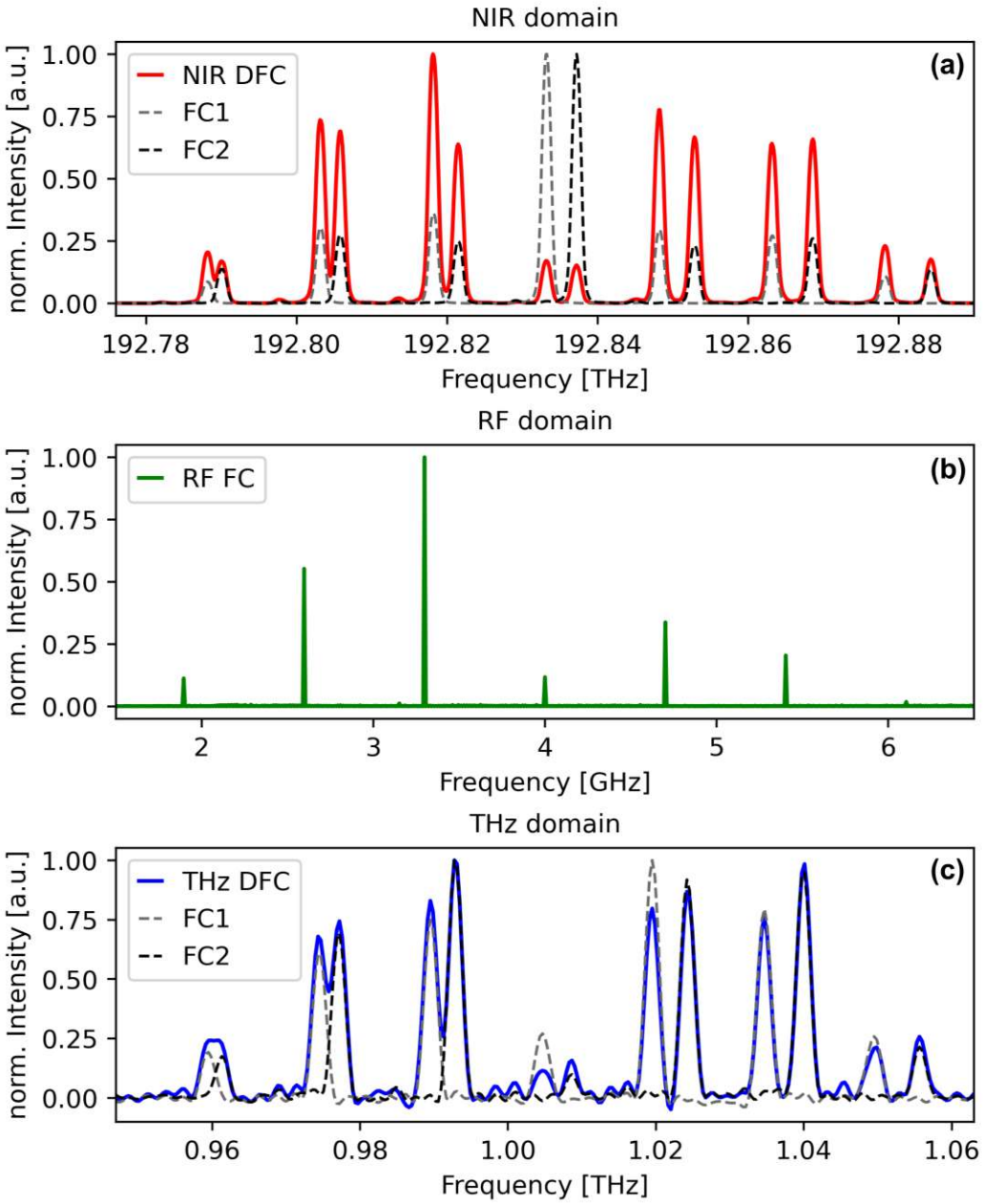

Figure 5.19: Dual frequency comb (DFC) spectra in the NIR domain (a) measured with an optical spectrum analyser, in the RF domain (b) measured with a photo diode and an electrical spectrum analyser, and in the THz domain (c) measured with a Fourier transform spectrometer. Comb one exhibits a line spacing of 15 GHz (FC1), comb two one of 15.7 GHz (FC2), and consequently the resulting RF comb (RF FC) has a spacing of 700 MHz.

by 4 GHz. The intensity variations develop due to changes in the fiber system, when a comb is turned of to measure the other one. The main impact comes from gain competition in the used optical amplifiers and from reflections in the system influencing the modulation depth of the modulators. The unique feature of dual comb applications is the down-conversion of the two coherent combs (and consequently the spectral response of a sample under investigation) to the RF domain [7]. FC1 and FC2 are mixed and detected by a fast photodiode and can be analysed with an RF spectrum analyser. As a result each pair of comb teeth produces an RF heterodyne signal at a specific frequency as seen in Figure 5.19 (b). This set of RF frequencies forms a comb in the RF domain itself with a spacing corresponding to the difference in line spacing of the original combs, here 700 MHz, and is centered at the introduced frequency offset at 4 GHz. Implementing the NIR DFC setup into the TOFL system enables the generation of THz dual frequency combs as well. The corresponding THz spectra based on the above presented NIR DFC are shown in Figure 5.19 (c) and measured with a Fourier transform spectrometer. For any THz DFC application a fast and sensitive THz detector is required to perform the comb teeth heterodyning and the corresponding down-conversion in the THz domain as well. Nevertheless, Figure 5.19 (c) proofs that the TOFL source shows also the potential for advanced sensing techniques such as dual frequency comb spectroscopy.

5.3.3 Other Near-Infrared Architectures for Spectral Shaping

One great benefit of the TOFL method is that it is based on mature NIR technology, which provides a huge toolbox of spectral shaping approaches. Generally speaking, all available techniques for NIR light generation and manipulation can be utilized to generate the desired spectrum in the NIR domain, which is subsequently down converted to the THz domain by means of photomixing. In the previous section 5.2.3, it was shown that the THz single comb teeth linewidth of the TOFL spectra lies in the range between 1 MHz and 10 MHz, mainly defined by the phase noise of the two independent laser diodes. Ideally, one would derive all NIR frequencies participating in the TOFL process, from a single frequency line. As conclusion for this chapter, another two NIR architectures (purely studied in the NIR domain) are presented and their theoretical impact for the THz generation in a TOFL setup is discussed, especially in the sense of THz linewidth narrowing.

In chapter 4.4.5, an electro-optic FC setup based on a phase modulator in a fiber loop was discussed. Together with the considerations above regarding the increase in modulation depth when the carrier passes through several modulators, it is evident that a signal circulating in a loop with a PM will lead to broad FC generation [187]. Here, a simpler version of the setup

presented in Figure 4.6 (e) is studied. Without an optical seeding CW laser and an optical

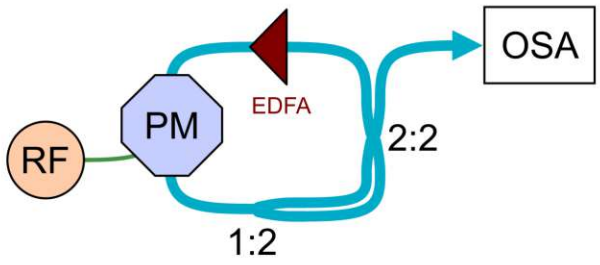

Figure 5.20: Schematic of a fiber loop frequency comb setup consisting of an RF driven phase modulator (PM), an erbium doped fiber amplifier (EDFA), a 1:2 fiber splitter, a 2:2 fiber combiner and an optical spectrum analyser (OSA).

delay line (ODL), the system reduces to a looped erbium-doped fiber amplifier (EDFA) and phase modulator, which builds in principle a fiber laser that will spontaneously start lasing somewhere around the peak of the EDFA gain curve. The free spectral range (FSR) of ∼20 MHz is defined by the fiber loop length (or the corresponding round trip time). Without a mechanism that keeps the PM driving and the loop FSR in resonance, no stable comb can be generated at the output. Also the frequency spacing of the comb is restricted to the MHz range or below. Stabilization of the output and increasing of the line spacing to the GHz range can be done utilizing the Vernier effect [218]. It is implemented by inserting a 1:2 fiber splitter together with a 2:2 fiber combiner in the loop (the additional output of the combiner is used as outcoupler). The resulting setup is depicted in Figure 5.20 and assembles two fiber loops that share most of its optical path. Due to imperfections of the splitter and combiner, the loop lengths (and correspondingly their FSRs) are slightly different. According to the Vernier effect, lasing modes can only develop at frequencies which are matching multiples of both individual loop FSRs, leading to a common new resonance condition. When the PM is driven at that frequency, a broad comb is generated with the corresponding frequency spacing, in this case of ∼13.5 GHz.

Figure 5.21 presents two comb spectra in (a) and (b) measured with different sets of splitter and combiner, respectively, which results in a small change of the resonance condition. The shape of the comb and its position in the frequency window depend on the resonance condition and the RF driving together with the gain curve of the EDFA. When such a fiber loop is implemented in the TOFL setup, one can generate rather broad THz combs as well. For most applications combs that are hundreds of GHz broad are not necessary. For example the linewidths of most absorption features at ambient conditions do not exceed several GHz at all.

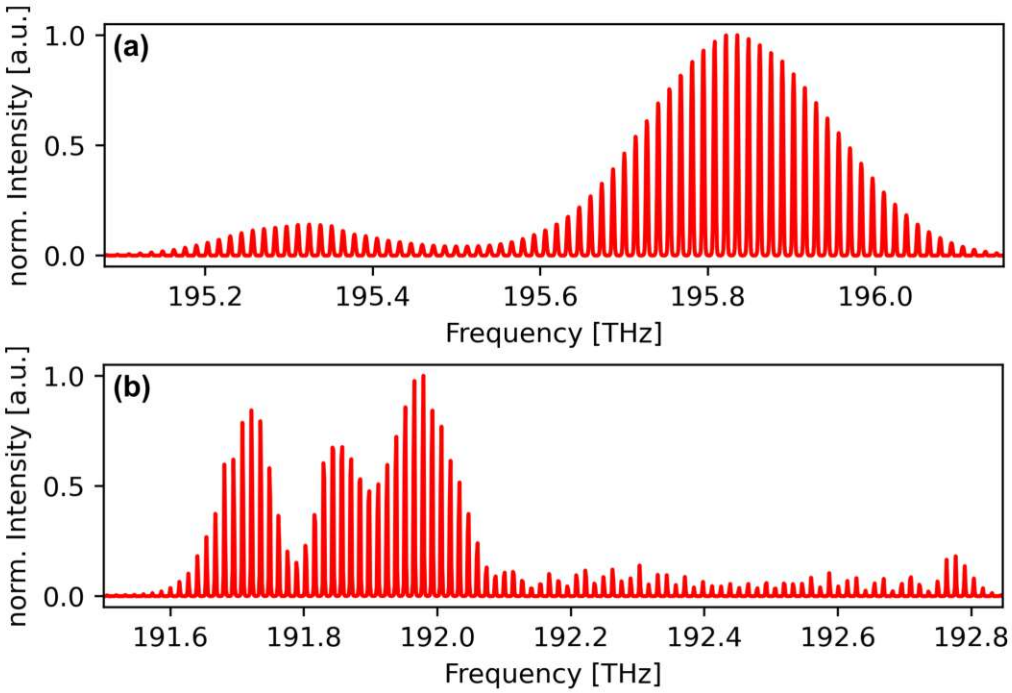

Figure 5.21: Broad NIR frequency combs generated with a phase modulator in a fiber loop setup. Two different sets of fiber splitter and combiner are used in (a) and (b), changing slightly the resonance condition, and thus, the shape and frequency position of the developing comb. The spectra are measured with an optical spectrum analyser with a resolution of 1.2 GHz.

In addition, one needs also to take into account, that the generated THz power is distributed over all comb lines leading to very low power per line values. Nonetheless, a ∼1 THz broad NIR comb is of high interest for TOFL generation with narrow THz linewidths. Optical bandpass filters can be used to pick up single frequency comb lines as input for the TOFL method instead of individual, independent laser diodes. Consequently, the advantageous derivation of all NIR frequencies from a single CW line, that was mentioned at the beginning of this section, becomes possible. In this case, all NIR frequencies share the same phase fluctuations inherited from the single laser source. Since the TOFL technique is based on difference frequency generation of the THz light, this source of noise will be canceled out leading to THz linewidths that reach down to the Hz level.

A similar approach can be realized based on optically pumped microresonator (or Kerr) frequency combs, which have been discussed briefly in chapter 4.3. Their advantage lies in

the large FSR values of hundreds of GHz due to the short roundtrip length compared to fiber loops. The larger the frequency spacing between lines, the easier it will be to pick up single lines with an optical filter. It also becomes simpler to generate modes that cover several THz, necessary to produce TOFL spectra beyond 1 THz that are derived from a single laser source. On the downside, they are hardly tunable regarding the FSR compared to electro-optic combs. For demonstration purposes such a microring resonator is studied in Figure 5.22. An optical microscope picture of the ring with 40 µm radius and coupled waveguides (2.5% coupling ratio) with input, pass, drop and add ports is displayed in (a). A free running (without any input light) erbium doped fiber amplifier (EDFA), acting as white light source due to amplified spontaneous emission (ASE), is used to measure the transmission at the drop port presented in (b). The measurement reveals a FSR of 280 GHz, which enables easy filtering of modes that are more than 1 THz apart, when the microring resonator is driven as Kerr comb.

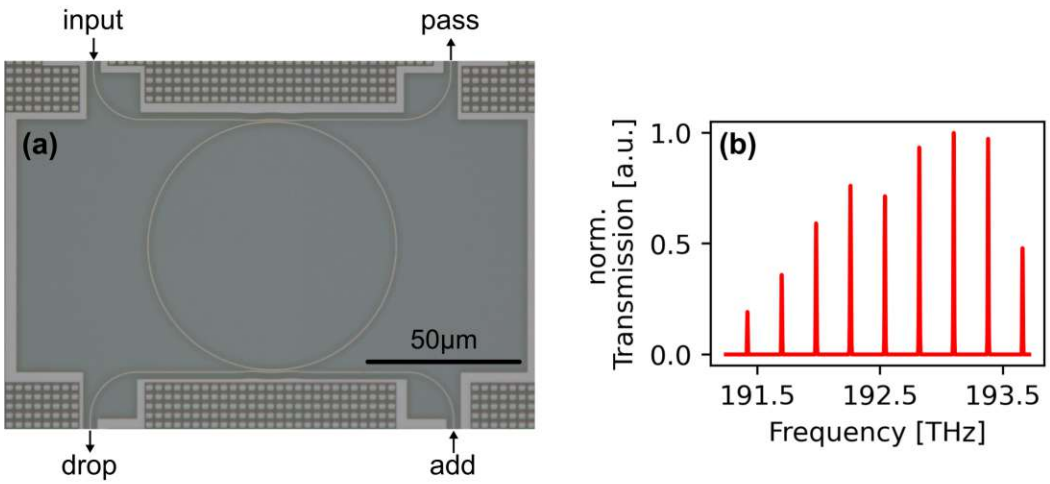

Figure 5.22: (a) Optical microscope picture of a silicon microring resonator coupled to input, pass, drop and add ports. (b) Transmission of an EDFA white light source measured at the drop port with an optical spectrum analyser.

5.4 Conclusion

In conclusion, this chapter presents a novel method for terahertz opto-electronic frequency comb (TOFL) light generation that is very flexible in terms of spectral shaping. It merges two mature technologies, namely the flexible generation of near-infrared electro-optic frequency combs and the efficient difference frequency conversion in photomixing devices. Almost arbitrary comb spectra can be designed via the full electronic control of the number of comb lines, the frequency spacing between the lines and the power distribution between them. The quality of the generated terahertz combs is proven by the sensing of the collision broadening of an ammonia rotational transition line, which reveals a THz linewidth of <10 MHz. Straight-forward handling is guaranteed by the standard fiber-coupled optical components building a robust setup. The presented implementation of this method allows a continuous spectral coverage from 0.5 THz to 3.5 THz, which exceeds other electro-optic based techniques [213, 219] or approaches utilizing the non-linearity of a THz photomixer for comb generation [220] by an order of magnitude. It also compares very well to quantum cascade laser terahertz frequency combs in terms of number of comb lines within a 10 dB intensity variation, power per comb line [158,196,197,221] and also in terms of the frequency resolution for potential spectroscopic applications [8, 222]. The possibilities to further increase the available parametric space are discussed as well and emphasize the flexibility of this method.

6 Hollow Waveguide Gas Cells for Terahertz Sensing

The optimization of terahertz systems for sensing applications is one of the main perspectives of this thesis. Chapter 3.3.4 indicated that, besides the large absorption cross-sections offered by that spectral region, the potential to develop tunable systems is of particular interest to target different application dependent molecules with a single measuring device. In order to realize practical real-world applications, the development of adjustable, rapid systems is necessary, which are reliable and remain compact in size, while keeping the production costs affordable.

The sensitivity of gas sensors based on direct light absorption at certain wavelengths is mainly dependent on the optical path length (OPL), which defines the interaction length of the sample gas molecules and the photons of the sensor's (or external) light source. This relation is described by the Beer-Lambert law and has been discussed in chapter 3.3.3. Standard gas cells become rather inconvenient when it comes to the extension of the optical path length, as the OPL corresponds to the cell length. Multipass gas cells, however, offer a more advanced way of increasing the OPL. As their name suggests, multipass gas cells enable the probing light beam to go through the gas volume in the cell multiple times. The most commonly used types are Herriott and White cells [223, 224], while circular multipass cells represent a more recent approach [225]. However, these cells are often quite bulky, require a precise optical alignment and need a significant amount of gas sample volume reaching up to liters to fill the whole cell. Of that volume only a small fraction is probed during the sensing measurement due to the geometry necessary for multiple beam reflections. An alternate solution might present the integration of optical cavities into a spectroscopic system, which entails an enhancing effect on its sensitivity [226]. There, the demanding fabrication of high-finesse cavities in the THz domain presents an obstacle that has yet to be overcome. THz optical fibers and waveguides have been proposed as a promising alternative for sensing applications as well [227, 228]. Solid core fibers are capable of providing interaction of the molecular sample with the evanescent THz field for sensing [229], but hollow core designs are of particular interest as they can act as miniaturized gas cells with predefined optical absorption paths, while guiding THz radiation inside the hollow core of a fiber or waveguide [230, 231]. By filling the hollow core with only a few milliliters of a gas sample, the analyte is exposed to the guided THz light providing a maximum overlap between the molecules and the THz field. However, conventional

hollow waveguides (HWGs) often struggle when it comes to compactness and flexibility and are susceptible to mechanical vibrations and temperature fluctuations. Therefore, they require careful handling or additional protection and are usually rather demanding in the production process including the application of internal coatings. It should be noted that the development of 3D printing techniques for hollow core THz fibers may provide a solution to some of these issues, streamlining the production process [232]. Recently, Mizaikoff et al. proposed a new type of hollow waveguide, the so called substrate-integrated hollow waveguide (iHWG), that allows for the advantages of a traditional HWG while eliminating its major drawbacks [233]. The potential of iHWGs for advanced sensing systems in the mid-infrared [234–236] and the ultraviolet [237] has already been demonstrated.

This chapter presents the first implementation of substrate-integrated hollow waveguides in a THz sensing system. A compact and highly versatile spectroscopic platform is introduced by combining robust iHWGs with the opto-electronic THz source presented in the previous chapter 5. The source allows for direct electronic control of the adjustable spectral shape as has been established. It is shown that this source enables a sideband tuning technique that is faster, more accurate, and easier to work with than a classical continuous wave single line sweep. The flexible sensing capabilities of this platform are demonstrated by measuring various absorption lines of nitrous oxide (N_2O). The results presented in this chapter have been partially published in the peer-reviewed journal article Theiner *et al.*, "Flexible terahertz gas sensing platform based on substrate-integrated hollow waveguides and an opto-electronic light source," Optics Express **31**, 15983-15993 (2023).

6.1 Substrate-Integrated Hollow Waveguides

A substrate-integrated hollow waveguide (iHWG) presents a miniaturized gas cell, composed of a solid substrate material, such as aluminium, with integrated reflective light-guiding channels and a sealing top plate. Figure 6.1 illustrates a schematic of an iHWG (a) and presents optical pictures of two devices equipped with gallium arsenide (b) and polyethylene windows (c), respectively. With this design, the geometry of the channels can be customised, reaching from simple straight channels (as used in this work), to meandering structures or more advanced concepts as shown in Figure 6.1 (d)-(h) [238]. iHWGs allow for increased optical path lengths while maintaining a compact size and a robust device. Besides the portability that comes with the miniaturization, the use of a smaller absorption cell is also motivated by fast sampling times allowed by a small sample gas volume, which is beneficial for real-time applications.

Thus, the OPL should be seen in relation to the gas cell volume, making the volume-normalized path length δ = OPL/V an important figure of merit [239].

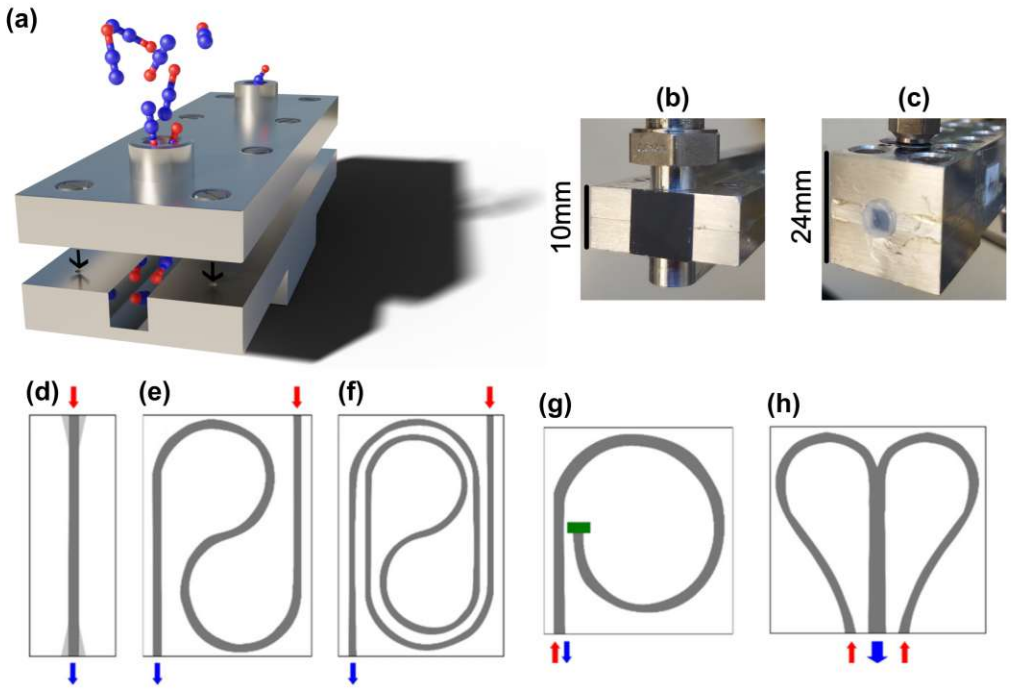

Figure 6.1: (a) Schematic drawing of a substrate-integrated hollow waveguide consisting of a light guiding channel integrated into a solid substrate and a sealing top plate with gas in- and outlet. Optical pictures of two iHWGs equipped with gallium arsenide (b) and polyethylene (c) windows, respectively. (d)-(h) Examples of different possible optical channel geometries (dark gray) adapted from [238]. Red arrows mark incident light, blue arrows output light. (d) Straight channel (used in this work) with/without inlet and/or outlet funnel (light gray), (e) meandring one-turn channel, (f) meandring two-turn channel, (g) coiled channel with reflecting mirror (green), (h) heart-shaped dual channel.

In the following, five iHWGs are studied with varying dimensions and optical path lengths (summarized in Table 6.1). All of them have been fabricated from commercial aluminum alloy (Al-MgO_3) and with integrated straight-line optical channels. Two of them exhibit a waveguide tappering at the very end (here denoted as optical funnel) to facilitate light in- or outcoupling. The light guiding channels have been polished with diamond suspensions to realize mirror-like surfaces. Examination by an atomic force microscope has revealed a surface roughness

of 44 nm [233]. In order to enable gas sensing and THz radiation propagation at the same time, the iHWGs have been equipped either with 1 mm thick polyethylene (PE) windows or with 650 µm thick gallium arsenide (GaAs) windows using a two-component epoxy adhesive. A maximum leak rate of 0.0048 mbar L/min and 0.0029 mbar L/min was found for PE and GaAs windows, respectively. Sensing experiments are done in continuous flow configuration at a gas flow rate of 0.1 L/min to prevent contamination by the ambient air.

Table 6.1: Dimensions of the optical channel and the footprint (length x width x depth) of the iHWG devices used in this work and their calculated cut-off frequencies. The * marks devices fabricated with an optical funnel (i.e. a waveguide tappering at the very end) to facilitate light in- or outcoupling.

Name	Channel [mm]	Footprint [mm]	TE_{10} f_{cut} [GHz]	TE_{11} f_{cut} [GHz]	TE_{20} f_{cut} [GHz]
Al-150-2	150x2x2	150x25x19	74.95	105.99	149.90
Al-75-2*	75x2x2	75x25x24	74.95	105.99	149.90
Al-30-4	30x4x4	30x25x15	37.47	53.00	74.95
Al-75-4*	75x4x4	75x25x22	37.47	53.00	74.95
Al-90-4	90x4x4	90x25x15	37.47	53.00	74.95

As mentioned at the beginning of this chapter, iHWGs have already found applications in mid-infrared and ultraviolet sensing systems. However, they are oversized for those spectral ranges, causing the probing beam to bounce within the reflective light guiding channel. In

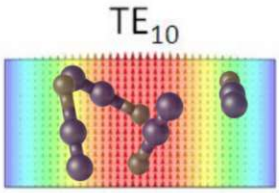

Figure 6.2: Schematic of the fundamental mode in a hollow waveguide filled with some molecules.

contrast, their dimensions are well suited for the terahertz domain and consequently the theory of rectangular metallic hollow waveguides applies, which was discussed in chapter 3.2. The cut-off frequencies of the iHWGs are calculated using equation 3.21 for the modes TE_{mn}

of a waveguide with a cross-section of $a \times b$ and their values are included in Table 6.1. As a consequence, the evolving THz modes fill the entire waveguide cross section, providing the significant advantage that every molecule present in the waveguide interacts with the probing light, and thus, participates in the sensing process. This makes iHWGs extremely efficient gas cells. An illustration of this scenario is given in Figure 6.2 for the fundamental mode TE_{10}.

6.2 Experimental Setup

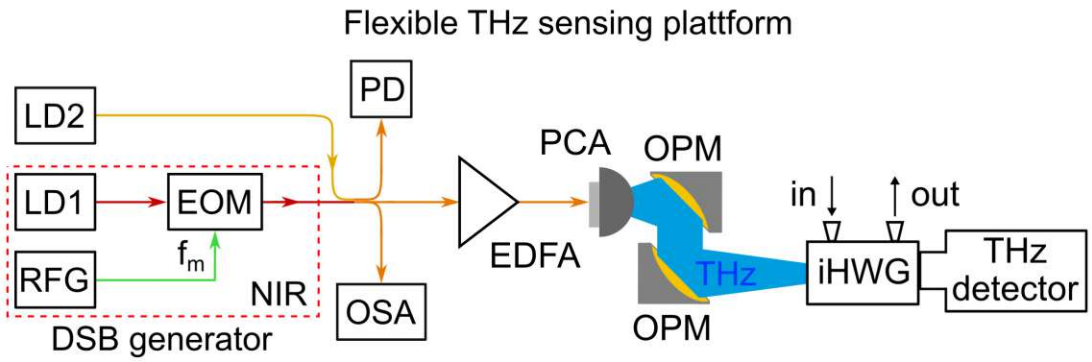

Figure 6.3: Sketch of the THz sensing platform consisting of a near-infrared dual sideband (DSB) generator realized by a fixed-wavelength diode laser (LD1) and an electro-optic intensity modulator (EOM) driven by a RF generator (RFG), a tunable diode laser (LD2), an erbium doped fiber amplifier (EDFA), a photodiode (PD), an optical spectrum analyser (OSA) and a photoconductive antenna (PCA) acting as NIR to THz converter. The generated THz light is coupled via two off-axis parabolic mirrors (OPM) to a substrate-integrated hollow waveguide (iHWG) guiding the beam to a THz power detector.

A schematic of the THz sensing system is represented in Figure 6.3. In general, the light source is based on the THz opto-electronic frequency comb light setup demonstrated in the previous chapter. Thus, the THz spectral components are defined completely in the NIR domain. A 1555 nm, fiber-integrated, temperature-stabilized NIR laser diode (LD1) is modulated by a fiber-coupled electro-optic intensity modulator (EOM) driven by a RF signal generator (RFG) with adjustable modulation frequency f_m. As seen in chapter 4.4.2, the intensity modulator is based on a Mach-Zehnder interferometer, where a static DC bias can introduce a phase shift between both interferometer arms. A phase difference of $\pi/2$ results in a dual sideband generation (DSB) with carrier suppression. Essentially, three spectral components are involved

in the DSB process, namely the lower sideband $SB_- = f_{LD1} - f_m$, the upper sideband $SB_+ = f_{LD1} + f_m$ and the suppressed carrier $f_c = f_{LD1}$ as indicated in Figure 6.4. The spectrum serves as example for the principle of DSB generation and is generated with a modulation signal of ∼10 GHz for good visibility in respect of the 1.2 GHz resolution of the OSA. A carrier suppression of ≥15 dB can be reached. Technically speaking, this spectrum represents a minimalist version of an electro-optic frequency comb as well, since it consists of equidistant modes with a common phase relation. However, its (theoretical) comb character does not play a key role in the following study.

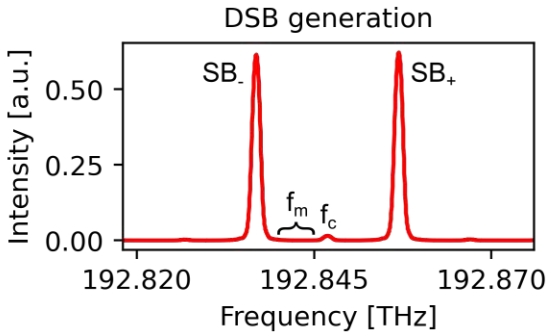

Figure 6.4: Dual sideband generation (SB_-, SB_+) with suppressed carrier (f_c) via intensity modulation at frequency f_m. Spectrum measured with an optical spectrum analyser.

In order to generate THz light, the DSB NIR radiation is combined with a second single-colour NIR laser in a photomixing device, enabling difference frequency mixing. For that purpose, a tunable NIR diode laser (LD2) is installed in the setup. It comes with a frequency monitoring method due to an internal HCN gas cell reference [240]. All the NIR radiation is combined in a 50:50 fiber combiner and amplified to 25 mW by an erbium doped fiber amplifier (EDFA) and coupled to a photoconductive THz antenna acting as photomixer (PCA). The PCA represents an efficient opto-electronic NIR to THz converter based on the optical beating of the NIR spectral lines as discussed in the previous chapter. The resulting THz spectral components are a copy of the NIR DSB spectra translated into the THz domain. Thus, they are uniquely determined by the NIR laser frequency offset defining the central frequency component $f_c = \Delta f = f_{LD2} - f_{LD1}$ and the modulation frequency defining the generation of lower sideband $SB_- = \Delta f - f_m$ and upper sideband $SB_+ = \Delta f + f_m$. Since two completely independent NIR lasers are used with a standard temperature stabilisation, a residual frequency drift between them can

be observed. Within a 10 min time window the drift of Δf lies in the range of $\sim$50 MHz. The use of solely standard fiber-optic components and the electronic control of the synthesized THz spectra lead to a robust light source providing flexible tuning and straightforward handling with a spectral resolution of <10 MHz as has been established in the previous chapter as well. Two off-axis parabolic mirrors (OPM) are used to couple the newly generated THz light from the PCA to an iHWG. With a pressure gauge, the pressure in the gas cell and its variation can be monitored along the gas measurements. During the data acquisition in a 1 min time window, a variation of $\sim$2 mbar is observed. For the detection of the THz radiation a Golay cell acting as room temperature THz power detector is implemented directly at the output of the iHWG eliminating the need of additional coupling optics.

6.3 Waveguide Characteristics

To investigate the suitability of iHWGs for THz applications, the five devices summarized in Table 6.1 with varying dimensions and optical path lengths are studied regarding their transmission properties. When the wavelength of LD2 is tuned without any intensity modulation applied (and without carrier suppression) while LD1 remains at fixed wavelength, a standard continuous wave single THz frequency sweep is realized. The resulting single THz frequency line is tuned via the LD2 wavelength defining the laser diode frequency offset Δf. The transmitted signal through the iHWG is compared to the intensity recorded when the iHWG is removed and the detector is moved to the position of the entry facet of the iHWG acting as reference. This method yields absolute transmission values for each THz frequency. To ensure equal incoupling efficiencies for same dimensions, the two iHWGs with optical funnels were implemented in the setup, so that the tapered end faces the detector.

Transmission data were obtained from 0.2 to 1.6 THz and are shown in Figure 6.5 (a). The discrepancies in the roll-off behaviour at low frequencies for different cross-sections can be attributed to the higher cut-off frequencies f_{cut} for the smaller waveguide dimensions (see Table 6.1) and follow the theory of rectangular metallic hollow waveguides discussed in chapter 3.2. For the sensing experiments, frequencies are used that are >3$\cdot f_{\mathrm{cut}}$ for dimensions 2x2 mm and >8$\cdot f_{\mathrm{cut}}$ for dimensions 4x4 mm, considering the cut-off frequency for the fundamental mode evolving in the waveguide. Additionally, the transmission measurements reveal incoupling losses of $\sim$40% and $\sim$80%, respectively, due to waveguide cross-sections of similar size as the THz focal point at the input facet. However, they remain similar for equal dimensions. Lastly, ic can be noted that the optical funnels do not have a significant impact

on the coupling from the waveguide to the detector.

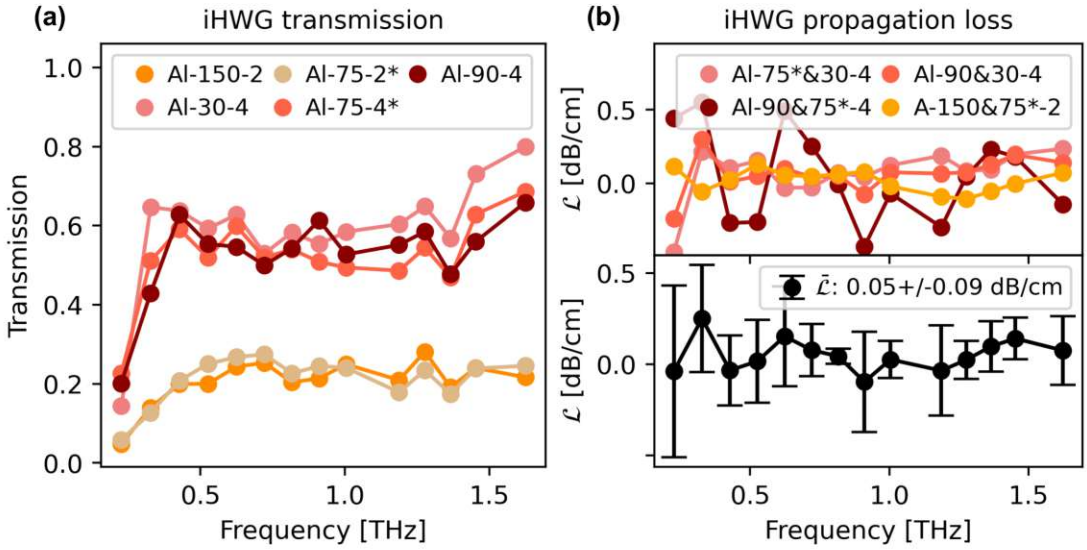

Figure 6.5: (a) Transmission through five different iHWGs without windows and with varying dimensions (summarized in Table 6.1) measured in the range of 0.2 to 1.6 THz. (b) Propagation loss calculated from pairs of the iHWG transmission measurements in (a) in the upper panel and its average values in the lower panel.

THz light traveling through the waveguide experiences the propagation loss $\mathcal{L}$ [dB/cm]. Pairs of the discussed transmission measurements (T_i, T_j) in iHWGs with the same cross-section but different lengths (L_i, L_j) are used to calculate

$$\mathcal{L} = -\frac{10\log_{10}(\frac{T_i}{T_j})}{L_i - L_j}. \tag{6.1}$$

Figure 6.5 (b) displays the calculated propagation loss for all available iHWG pairs in the upper panel and their average values plotted with a confidence interval of 90% in the lower panel. Negative values of $\mathcal{L}$ have no physical meaning, but appear due to noise in the data used for the calculations. Thus, the plot serves mainly as indication that the true nature of the propagation losses is smaller than the error margins of the measurements. An upper bound for the mean propagation loss for the entire frequency range of $\bar{\mathcal{L}}$ <0.14 dB/cm can be defined. This suggests that the propagation losses in the studied iHWGs are low enough to qualify them for proper wave guiding of THz light.

Two types of waveguides, Al-90-4 and Al-30-4, have been chosen for further measurements due to their lower f_{cut} and lower coupling losses when compared to 2x2 mm cross-section iHWGs. The waveguides have been equipped with GaAs and PE windows (Al-90-4 $\rightarrow$ Al-90-GaAs and Al-30-4 $\rightarrow$ Al-30-PE) to allow THz radiation to pass through while also ensuring gas tightness. They provide a volume-normalized path length of $\delta = 6.2 \cdot 10^4$ and require a sample gas volume of 1.44 mL for the 90 mm cell and 0.48 mL for the 30 mm cell.

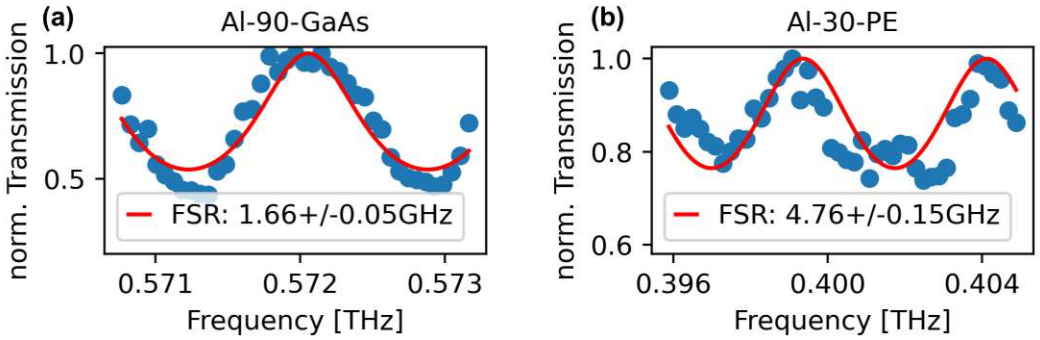

Figure 6.6: Fabry-Pérot resonances measured in Al-90-GaAs (a) and Al-30-PE (b), respectively (blue dots). The free spectral range (FSR) is determined by fitting of the experimental data with equation 6.2 (red lines).

By remeasuring the transmission through these waveguides, Fabry-Pérot resonances can be seen in Figure 6.6(a) and (b). The varying transmission is caused by interference between multiple reflections of the THz light due to the partially reflecting windows building a cavity. The phase difference between successive round trips is $\varphi = 2nkL$, which is dependent on the wavenumber k, the refractive index n and the length L. The transmittance is then defined by

$$T(\varphi) = \frac{1}{1 + F \sin^2(\varphi/2)}, \tag{6.2}$$

where the finesse coefficient F is determined by the reflectivity R of the windows in the form

$$F = \frac{4R}{(1-R)^2}. \tag{6.3}$$

Equation 6.2 can be used to fit the experimental data revealing a free spectral range (FSR) of 1.65 GHz for Al-90-GaAs and 4.76 GHz for Al-30-PE, which is consistent with the FSR calculated from the physical length of the iHWGs. For Al-30-PE one needs to take into account that the 1 mm thick PE windows are part of the effective cavity due to the low Fresnel reflectivity

coefficient of PE. Additionally, it is observed that the GaAs windows induce a higher modulation depth and a lower overall transmission due to the higher reflectivity compared to the PE windows.

6.4 Gas Sensing Techniques

Two different tuning methods for obtaining the frequency dependent transmission during gas sensing measurements are compared. Here, they are denoted as laser diode (LD) tuning and sideband (SB) tuning. The LD tuning is realized by changing the wavelength of LD2 without any intensity modulation, while LD1 remains at fixed wavelength, which is essentially the same configuration used for measuring the propagation losses in the previous section. It represents a typical continuous wave (CW) single frequency sweep, which is commonly used for high resolution spectroscopy with photomixers in the THz range [208]. This produces a single THz frequency, which is tuned through the absorption region under investigation while recording the transmitted intensity. The LD tuning method performs directly a measure of the line shape of the studied molecular transition. Each new frequency that is set at LD2 needs to be referenced to the internal HCN gas cell leading to rather long measurement times of ∼20 min.

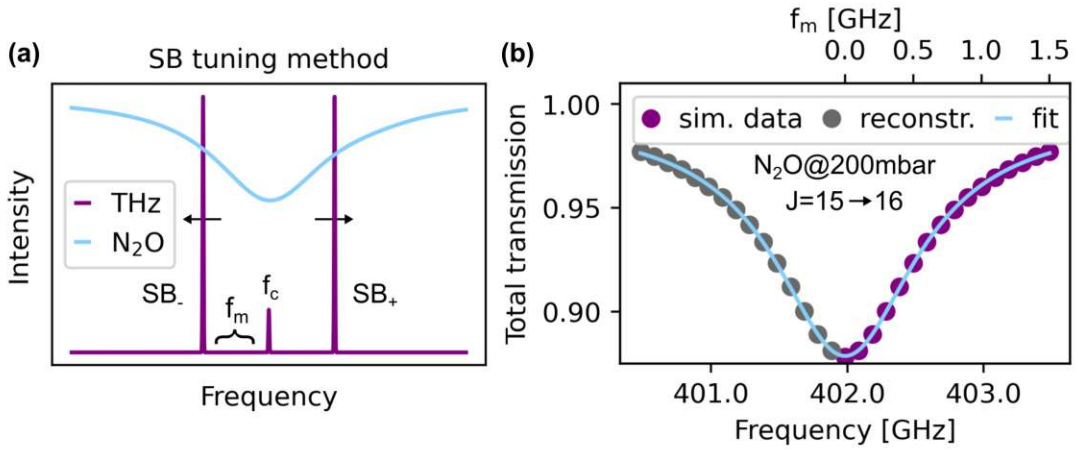

Figure 6.7: (a) Schematic depiction of the SB tuning method. Adjustment of the RF modulation frequency f_m sweeps the sidebands (SB_-, SB_+) simultaneously along both slopes around the center of an absorption line. (b) Simulation of the SB tuning results in a direct measure of the right slope of a symmetric absorption line (purple dots). Reconstruction of the full line shape (grey dots) enables a Lorentzian fit (light blue line).

As an alternative, a SB tuning method is introduced that is similar to other SB based spectroscopic techniques [17,241,242]. It relies solely on the electronic tuning of the RF modulation frequency f_m that drives the EOM controlling the SB offset. Figure 6.7 (a) displays the simultaneous sweep of the generated sidebands (SB_-, SB_+) along both slopes of an absorption line of a gas sample, while the center frequency (f_c) remains fixed in the middle of that line and does not carry any relevant information. The alignment of f_c to the center of that line is guaranteed by LD2 due to its internal available grid of HCN lines acting as frequency reference. LD1 is a free running laser diode, and thus, susceptible to a frequency drift affecting the measurement. To account for that, LD1 is also referenced to the nearest HCN line via optical beating of LD1 and LD2 on a fast photo diode (PD). During a measurement it remains below 50 MHz. For the actual gas measurement the frequency offset between both laser diodes is tuned to the desired THz frequency marking the center of the absorption line under investigation via further adjustment of the LD2 wavelength. This way, all frequencies involved are determined and therefore the actual THz frequency scale can be reconstructed without the need of a spectrometer. With the tunability of the LD2 wavelength comes the flexibility to align f_c to any absorption line in the accessible frequency window up to 3.5 THz limited by the frequency response of the used THz photoconductive antenna [207]. Thus, a huge amount of molecules with transitions lying in that frequency window can be targeted with that method. The RF control of the SB frequency offset is fast, convenient and provides an excellent precision (<10 Hz) allowing for a measurement time of $\sim$1 min (corresponding to a data acquisition time of $\sim$0.6 s per frequency point), mainly restricted by the speed of the slow THz detector. This increase in measurement speed compared to the standard LD tuning method is essential for potential real-world applications such as in situ environmental monitoring or medical screening.

In Figure 6.7 (b), a simulation of a measurement with the SB tuning technique is shown. The total transmission of all three participating THz frequency lines (i.e. the suppressed carrier and the two sidebands) is recorded together at the THz detector, while each is experiencing an absorption strength depending on its position on the frequency scale in relation to the absorption line. This results essentially in a superposition of the right and the left half of the line (purple dots) with a negligible offset introduced by the suppressed carrier, which remains fixed to the center of the absorption line. Due to the symmetric nature of the Lorentzian line shape of a gas sample under ambient condition (where pressure broadening is the dominant broadening mechanism), the recorded data represents the direct measure of the right half of the line under investigation. Thus, the total transmission data can be used to reconstruct the full line shape

(grey dots). It should be noted that in the actual experiment, the reconstruction also includes the noise of the measured data, which is copied to the left half of the line. A blind spot occurs around the center of the line, due to the cut-off frequencies of the used RF equipment that prohibits the utilization of frequencies below ∼300 MHz. The rotational transition properties (i.e. linewidth and absorption coefficient) are extracted by fitting a Lorentzian line (light blue line) to the experimental data.

6.4.1 Performance Comparison

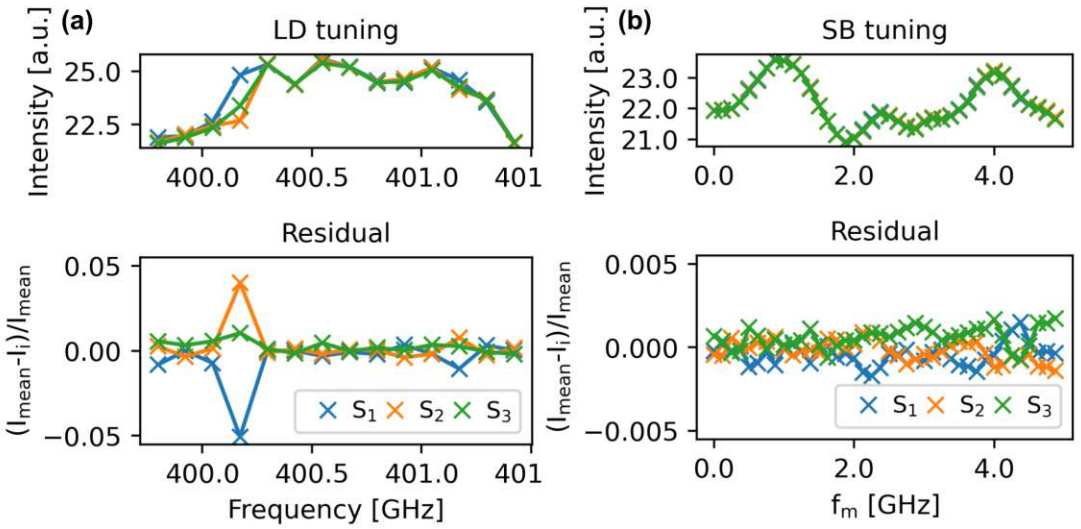

Figure 6.8: In three separate frequency sweeps (S_1, S_2, S_3) with (a) the standard LD tuning method and (b) the SB tuning technique, the total transmitted intensity through the empty Al-30-PE waveguide is recorded (upper panels). The signal residuals (lower panels) for every sweep show that the SB tuning outperforms the LD tuning in terms of photometric accuracy.

To compare the two tuning techniques and their suitability for gas sensing in iHWGs, the accuracy of the tuning mechanisms itself and their corresponding signal fluctuations coming from system instabilities are studied. For that purpose, the total transmitted signal through an empty iHWG is recorded for every frequency. Figure 6.8 presents the data as measured for three separate sweeps (S_1, S_2, S_3) of the LD wavelength (a) and the SBs (b) in the upper panels. The lower panels compare all sweeps to the average intensity measured at each frequency, revealing a difference of up to one order of magnitude in the residual signals. The

LD tuning technique's frequency accuracy is mainly determined by the stability of the laser diodes, which exhibit linewidths of <500 kHz and are affected by temperature drifts, whereas the generation of SBs is conveniently controlled by the RFG with an accuracy on the Hz level. Overall, the photometric accuracy of the SB tuning mechanism exceeds that of the LD tuning mechanism by a multiple. Additionally, the SB tuning technique decreases the measurement times by a factor of 20, making the method robust against slow drifts such as temperature.

6.5 Nitrous Oxide Measurements

The important greenhouse gas nitrous oxide (N_2O) was chosen to demonstrate the molecular sensing capabilities of iHWGs and the potential of the system for spectroscopic applications in the THz domain. Several rotational transitions between 376.777 GHz (12.56792 cm^{-1}) and 702.983 GHz (23.44899 cm^{-1}) are studied in form of transmission measurements through the waveguides Al-90-GaAs and Al-30-PE, which are continuously flushed with N_2O (N5.0 purity) at various pressures ranging from 150 to 300 mbar at an ambient temperature of 296 K.

In Figure 6.9 an individual N_2O absorption line measurement in Al-90-GaAs using the SB tuning method with a frequency step size of 25 MHz is displayed. The total transmission through the iHWG filled with the gas sample is recorded, which represents a direct measure of the right half of the N_2O line (blue dots) as described in the previous section 6.4. From the measured data, the full lineshape is reconstructed (grey dots), which allows the extraction of the linewidth (FWHM) and the absorption coefficient α of the rotational transition via a Lorentzian fit (red line) revealing a FWHM of 1332.92$\pm$54.28 MHz and α=14.0$\pm$1.33e^{-3} cm^{-1}. The deviation of the data from the Lorentzian fit (i.e. the fitting error) determines the error margins of the measurement. In comparison, the value for the absorption coefficient is one order of magnitude smaller than the previously shown propagation losses. Such small values become accessible due to the decreased error margins, realized by the higher photometric accuracy of the SB technique, as well as by the averaging effect coming from the α extraction in form of fitting the whole line shape instead of simply measuring an absolute amplitude value for the absorption strength.

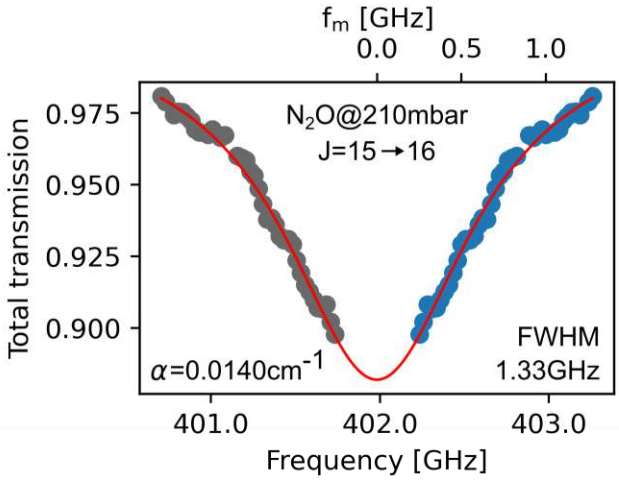

Figure 6.9: Transmission measured (blue dots) at the N_2O line at 401.885 GHz (13.405428 cm^{-1}) with the SB tuning in Al-90-GaAs at a pressure of 210 mbar and a temperature of 296 K. Reconstruction of the full line shape (grey dots) enables the extraction of the linewidth (FWHM) and the absorption coefficient α via a Lorentzian fit (red line).

6.5.1 Absoprtion Coefficients

The flexibility of the proposed sensing platform is demonstrated by the measurement of 9 randomly chosen N_2O lines, which is shown in Figure 6.10 with the corresponding data presented in Table 6.2. The individual measurements can be found in the appendix A.2 of this thesis. The extraction of the absorption coefficients of the measured lines confirm that the SB tuning technique yields a reduction in fitting error σ compared to the LD tuning method. From these measurements, it is possible to estimate the detection limit of the current demonstrator version of the platform to get a feeling for the smallest amount of gas molecules necessary to be observed. In view of the experiments carried out, a signal to noise ratio S/N of $\sim$200 can be assumed, leading to an error of $\sim 1\%$ for the transmission measurements. Therefore, an absorption strength (defined by the absorption path length, the number of molecules and the transition line intensity) >1$\%$ is necessary to be detectable. The strongest N_2O absorption line at 23.448992 cm^{-1}, which has a line intensity S of 3.11e^{-22} cm^{-1}/(molecule cm^{-2}) [133], is considered to be measured in the waveguide Al-90-GaAs with a length L of 90 mm. An absorption strength of 1$\%$ is achieved following $SNL = 0.01$, where N marks the number of

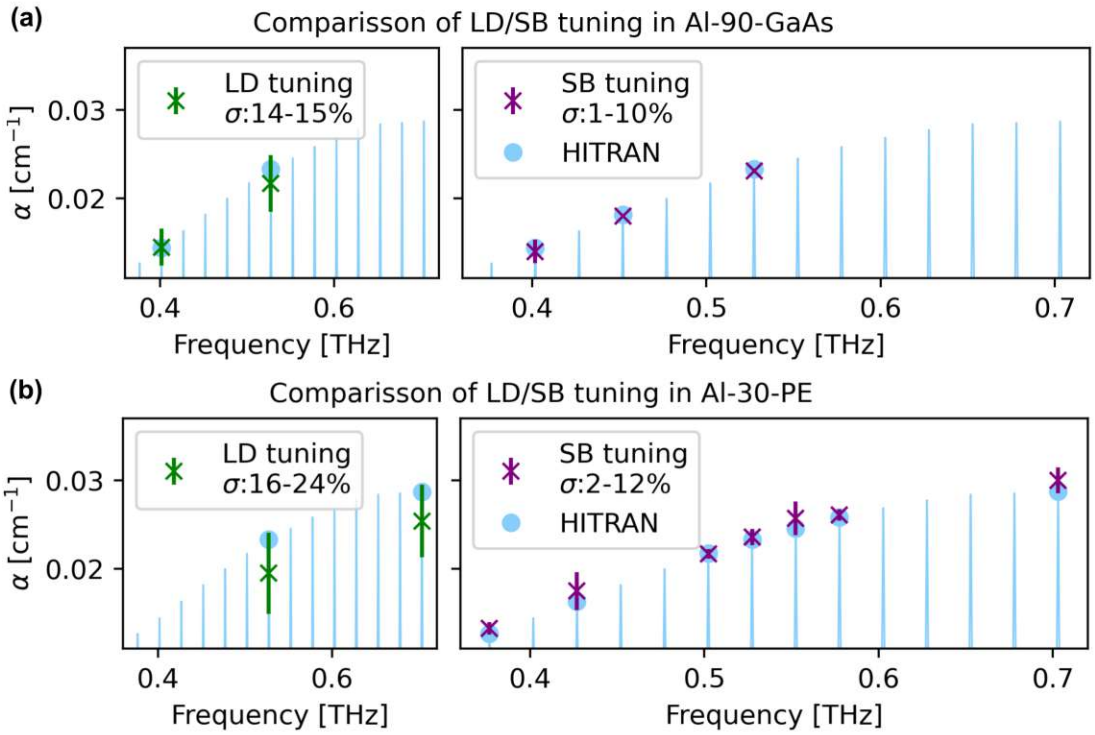

Figure 6.10: Summary of absorption coefficients extracted from several measurements on 9 different N_2O lines in Al-90-GaAs (a) and Al-30-PE (b) with the LD tuning (green crosses) and the SB tuning (purple crosses) compared to the analogous HITRAN data [133] (light blue dots and lines). Corresponding data can be found in Table 6.2.

molecules. Accordingly, it can be estimated that the smallest amount of molecules that could be detected with the presented system is ∼600 nmol of N_2O present in the gas cell.

Table 6.2: Absorption coefficients extracted from measurements on 9 different N_2O lines in Al-30-PE and Al-90-GaAs (marked with *) carried out with the two sensing methods. The data are visualized in Figure 6.10.

Transition	Pressure [mbar]	Absorption coeff. α [cm^{-1}]	HITRAN α [cm^{-1}]	Tuning method
J=20→21	205.0	$19.5\pm4.6e^{-3}$	$23.3e^{-3}$	LD
J=27→28	201.0	$25.4\pm4.1e^{-3}$	$28.7e^{-3}$	LD
J=15→16	205.0	$14.5\pm2.1e^{-3}$	$14.4e^{-3}$	LD*
J=20→21	201.0	$21.7\pm3.2e^{-3}$	$23.3e^{-3}$	LD*
J=15→16	210.0	$14.0\pm1.3e^{-3}$	$14.4e^{-3}$	SB*
J=17→18	202.0	$18.0\pm0.2e^{-3}$	$18.2e^{-3}$	SB*
J=20→21	199.0	$23.1\pm0.3e^{-3}$	$23.3e^{-3}$	SB*
J=14→15	199.0	$13.3\pm0.7e^{-3}$	$12.7e^{-3}$	SB
J=16→17	201.0	$17.8\pm1.9e^{-3}$	$16.3e^{-3}$	SB
J=19→20	208.0	$21.7\pm0.6e^{-3}$	$21.8e^{-3}$	SB
J=20→21	205.0	$23.6\pm0.9e^{-3}$	$23.3e^{-3}$	SB
J=21→22	206.0	$25.7\pm1.9e^{-3}$	$24.6e^{-3}$	SB
J=22→23	207.0	$26.1\pm0.6e^{-3}$	$25.8e^{-3}$	SB
J=27→28	208.0	$30.0\pm1.5e^{-3}$	$28.7e^{-3}$	SB

6.5.2 Linewidth Broadening

A closer examination of the N_2O line at 401.885 GHz is presented in Figure 6.11, which displays the well expected linewidth broadening with increasing N_2O pressure. The individual measurements can be found in the appendix A.3 of this thesis. The experimental data are consistent with the values calculated on the basis of HITRAN [133]. The results obtained with the SB tuning method, reveal a pressure-induced broadening of 6.30 ± 0.20 MHz/mbar, while the LD tuning method yields 5.48 ± 1.11 MHz/mbar. Following the theoretical considerations based on the HITRAN database result in a value of 6.37 MHz/mbar, which lies within the error margins of the experimental data for both methods. Nevertheless, the measurements utilizing the SB tuning exhibit substantially decreased fitting errors σ that are 4-5 times smaller compared to those of the LD tuning, likewise to the previous results on the absorption coefficients.

For the accurate quantification of an unknown gas sample in real-world sensing applica-

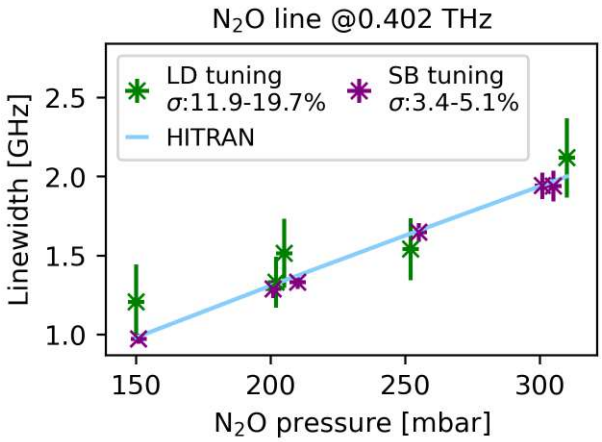

Figure 6.11: Measured pressure broadening of the absorption line at 401.885 GHz (13.405428 cm^{-1}) with the LD tuning (green crosses) and the SB tuning (purple crosses) in Al-90-GaAs compared to the linewidth values (light blue line) obtained from the HITRAN database [133].

tions, it is crucial to identify the absorption coefficient as well as the linewidth of its optically active transitions. The SB method proved to be useful for both tasks and has demonstrated superior performance to the LD tuning technique. In addition, this method offers unprecedented real-time control of the probing frequency, which is another advantage when compared to a wavelength sweeping based approach, making it attractive for in situ applications such as exhaled breath diagnostics [243].

6.6 Conclusion

The results shown in this chapter present the first implementation of substrate-integrated hollow waveguides as miniaturized gas cells in a THz sensing platform. The low propagation losses in these waveguides qualify them for proper THz wave guiding and make them ideal for spectroscopic applications, which is proven by the measurement of absorption coefficients and linewidths, as well as their pressure related broadening, of several rotational transitions of the greenhouse gas nitrous oxide. These results are all in good agreement with HITRAN data. The flexibility of targeting various absorption lines comes with the combination of the electro-optic THz source presented in the previous chapter. Furthermore, its all-electronic control of the THz spectral synthesis enables a sideband tuning technique with superior performance in

comparison with a standard wavelength tuning method leading to decreased measurement times (1 min vs. 20 min), improved photometric accuracy (error margins in the range of 1-12% vs. 12-24%), robustness against slow drifts and provides a straight-forward handling. Additionally, the compact size of the waveguides allows to sample small gas volumes (less than 2 mL) and realizes excellent volume-normalized optical path lengths of $\delta = 6.2 \cdot 10^4$, which is comparable to those of multipass gas cells [225, 239].

Summary and Outlook

Summary

The terahertz spectral region offers a large number of molecular fingerprints that are relevant for several monitoring tasks related to the environment and to the human health. Some of them provide even higher absorption cross-sections compared to the well-established near-infrared domain. A convenient light source presents the key for the investigation of the chemical composition of unknown samples and the frequency comb revolutionized time and frequency metrology in general and specifically established itself as state of the art tool for such tasks.

This thesis was dedicated to exploit the huge spectroscopic potential of the terahertz part of the electromagnetic spectrum by the development of a versatile sensing system. Frequency comb sources in that spectral region are still in their infancy and are typically quite inflexible when it comes to adjusting the comb's spectral shape or require cryogenic cooling. In this work, a novel concept was introduced for terahertz comb generation at room temperature that offers a great degree of freedom in the comb spectral design. It is based on two mature technologies, namely electro-optic modulation for the generation of optical sidebands on a single frequency carrier forming a near-infrared frequency comb and photomixing for the down-conversion of the comb to the terahertz domain by means of difference frequency generation. The combination of both realizes a terahertz comb synthesizer that provides electronic control of the spectral content. Its flexibility was demonstrated by the measurement of numerous comb spectra generated with different modulation schemes that were designed to achieve several goals. On the one hand, to establish the current accessible parametric space that comprises combs with >40 teeth, frequency spacings beyond 20 GHz and continuous tuning over 3.5 THz. On the other hand, they were designed to discuss several potential sensing possibilities including dual comb and comb based Fourier transform spectroscopy and the recreation of molecular fingerprints. Additionally, a rigorous linewidth study was presented to prove the high quality of the generated terahertz combs with single tooth widths <10 MHz and their sensing capability that was demonstrated by the measurement of a rotational transition of ammonia (NH_3).

Besides a matching light source, gas sensors rely on the interaction length of the gas molecules and the probing light (i.e. the optical path length) in terms of sensitivity. Standard gas cells become rather inconvenient when long optical path lengths are required. Among

alternate solutions, the substrate-integrated hollow waveguides (iHWGs) seem to provide the greatest potential for the realization of robust sensing devices. These waveguides are based on reflective light guiding channels that are integrated into a solid substrate, which enables advanced geometries, while maintaining a compact device. Gas sensors based on such miniaturized gas cells have already been utilized in the mid-infrared and in the ultraviolet domain. Their suitability for the terahertz region was proven by the revelation of low propagation losses below 0.14 dB/cm qualifying them for proper wave guiding, which led to the first implementation of substrate-integrated hollow waveguides in the terahertz range in this thesis. Combining them with the novel spectrally flexible opto-electronic terahertz light source forms a versatile gas sensing platform that enables a fast frequency sideband modulation technique, which allows measurements on the $\sim$1 min time scale. This technique outperforms a standard wavelength tuning method in direct comparison, which was shown in several absorption measurements of nitrous oxide (N_2O). The potential of the platform for real-world applications was demonstrated by the accurate determination of absorption coefficients and linewidths of various N_2O transition lines, both crucial parameters for the quantification of unknown samples. The system requires small probing volumes <2 mL, which leads to excellent optical path length to volume ratios of $\delta > 10^4$, and promises already in the current configuration a detection limit of $\sim$600 nmol for N_2O.

Outlook

The version of the terahertz sensing platform that was presented in this thesis served mainly for the purpose of proof-of-principle demonstrations. Several optimization possibilities were already discussed throughout chapter 5 and chapter 6. Especially the technologies offered by the mature near-infrared and telecommunication fields provide a huge toolbox for spectral shaping that can be inherited to implement further degrees of freedom for the terahertz synthesis. Also the stability and accuracy of the system can be increased on this basis, as discussed, by the derivation of all involved spectral lines from a single source or by stabilization in form of referencing to an absorption line. In the long term, the optical fibre infrastructure for the distribution of frequency standards derived from atomic clocks, would allow the local generation of precise custom terahertz spectra on demand.

The accessible frequency window and output powers are defined by the used photomixing device. Progress in the development of efficient photoconductive antennas will push these limitations to higher frequencies and larger power values. Another approach provides the research

on terahertz amplifiers, for example based on quantum cascade heterostructure designs, which can be used to boost the power of the terahertz light subsequently to its generation.

The potential of the flexible terahertz platform opens a manifold of possible future applications and advanced sensing methods. Dual comb spectroscopy has become one of the most exciting techniques in that field recently. The generation of such dual combs has already been demonstrated in this thesis. In combination with a fast and sensitive terahertz detector, this will lead to a powerful spectroscopic system suitable for the investigation of complex gas mixtures due to its flexibility.

Another highly sensitive technique within reach represents cavity ring down spectroscopy, which relies on the enhancing effects of an optical cavity involved in the sensing. There, it is of importance, that the probing spectrum matches the resonances of an optical cavity. The flexible synthesis of terahertz spectra is ideal for this purpose and the all-electronic control makes it easy to keep the cavity and the spectrum in resonance as well. Such a high finesse cavity can be built with the substrate-integrated hollow waveguides, in combination with proper mirrors attached to both ends.

In general, the low propagation losses of these waveguides open many opportunities for application dependent adaptions. Used as miniaturized gas cells, extended optical path lengths become possible with meandring structures instead of straight light channels. Also more advanced geometries can be designed including interferometer architectures or multichannel structures. Their integration possibilities might be fully exploited implementing transmitter and receiver directly into the substrate progressing the development of portable sensing devices. All methods utilized for the terahertz spectral synthesis show the potential for on chip integration. Near-infrared laser diodes, electro-optic modulators and photoconductive antennas have all been realized as on ship solutions already.

Lastly, since this platform merges near-infrared and terahertz technologies, combined sensing in both frequency domains becomes possible. Advanced concepts are thinkable that target several transitions in both spectral regions simultaneously, or pump and probe methods, where a near-infrared pump beam changes the population of states of a vibrational transition that can be studied with a terahertz probe aiming for a rotational transition.

A Appendix

A.1 Ammonia Measurements

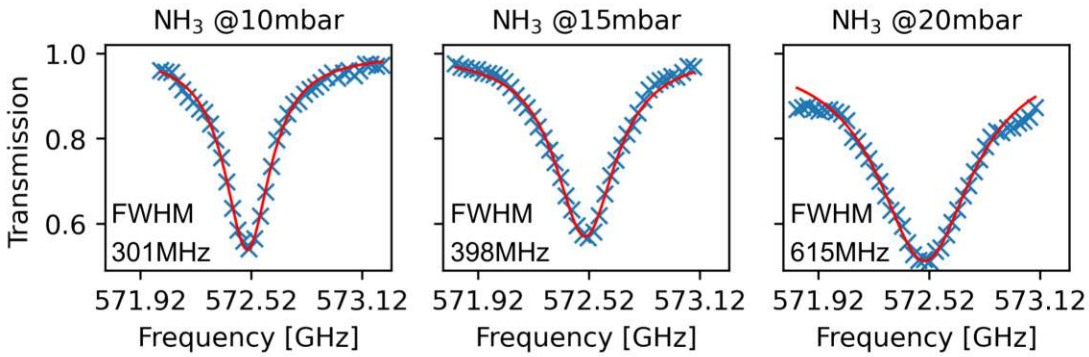

Figure A.1: Transmission measurements of ammonia (NH_3) in a standard gas cell at 296 K at various pressures. Lorentzian fits (red lines) extract the linewidths of the experimental data (blue crosses) and reveal the pressure induced broadening of the NH_3 transition as shown in chapter 5.2.3.

A.2 Nitrous Oxide Absorption Coefficient Measurements

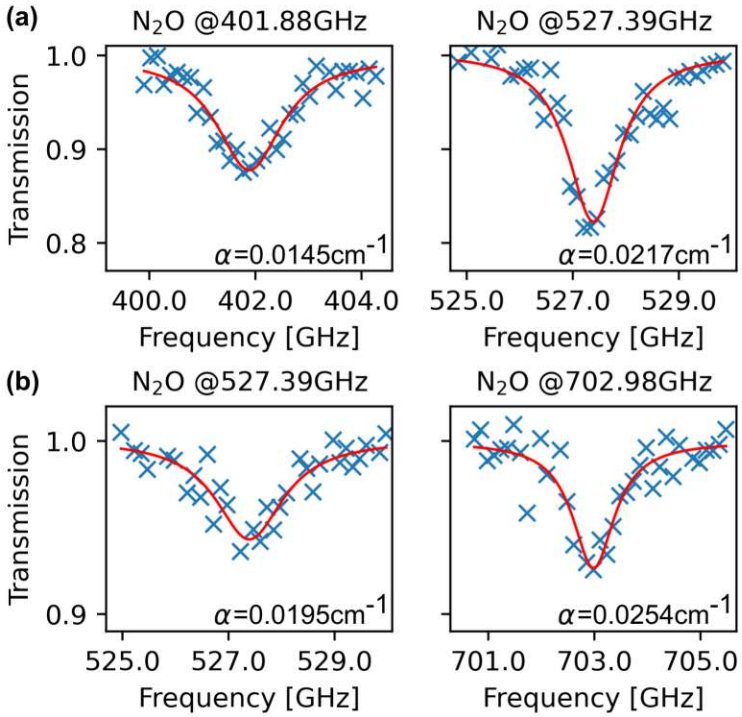

Figure A.2: Transmission measurements of nitrous oxide (N_2O) in the hollow waveguide gas cell Al-90-GaAs (a) and Al-30-PE (b) with the LD tuning method at 296 K at various pressures. Lorentzian fits (red lines) extract the absorption coefficients of the experimental data (blue crosses) and compare their individual transition line strengths as shown in chapter 6.5.1.

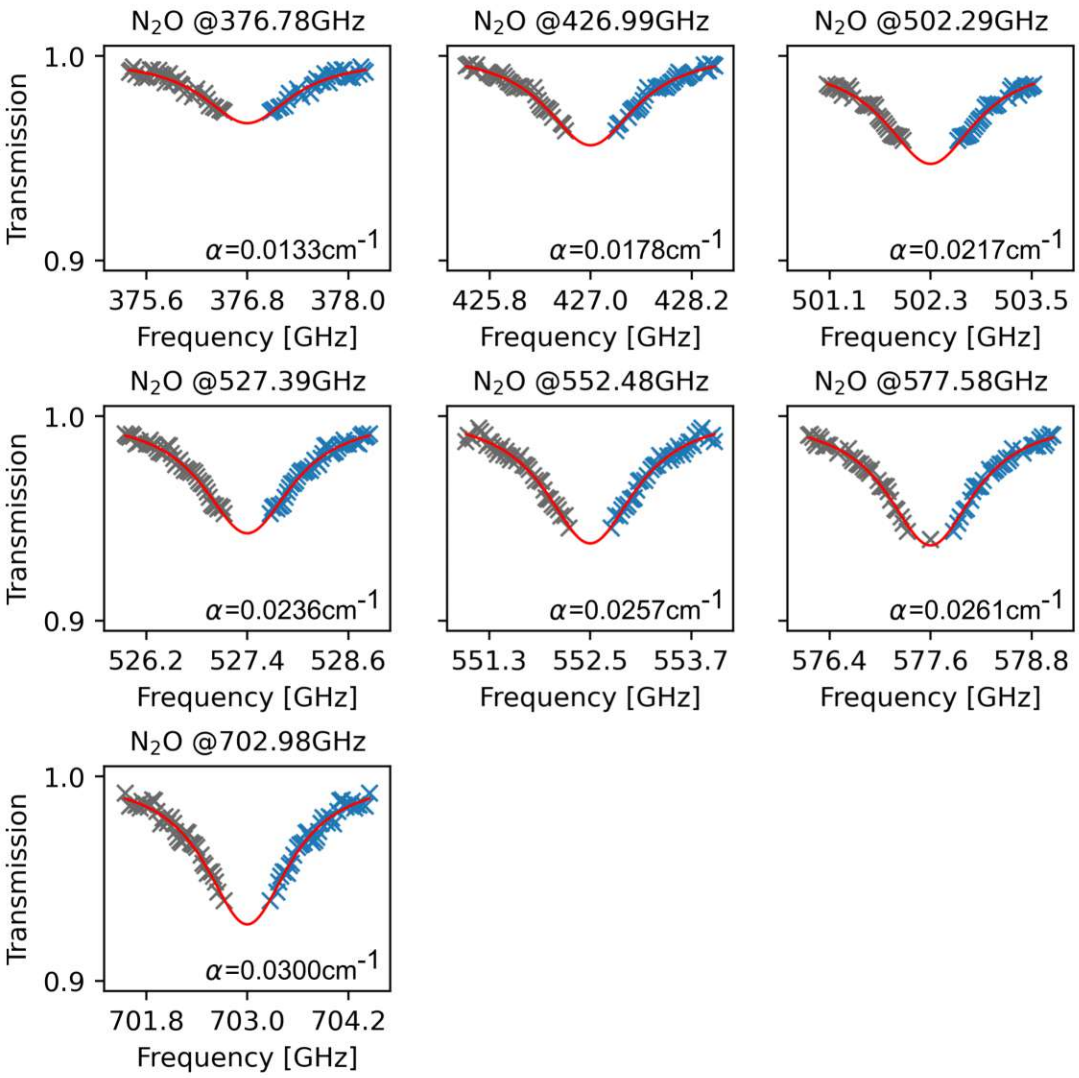

Figure A.3: Transmission measurements of nitrous oxide (N_2O) in the hollow waveguide gas cell Al-30-GaAs with the SB tuning method at 296 K at various pressures. Lorentzian fits (red lines) extract the absorption coefficients of the experimental data (blue crosses) and compare their individual transition line strengths as shown in chapter 6.5.1.

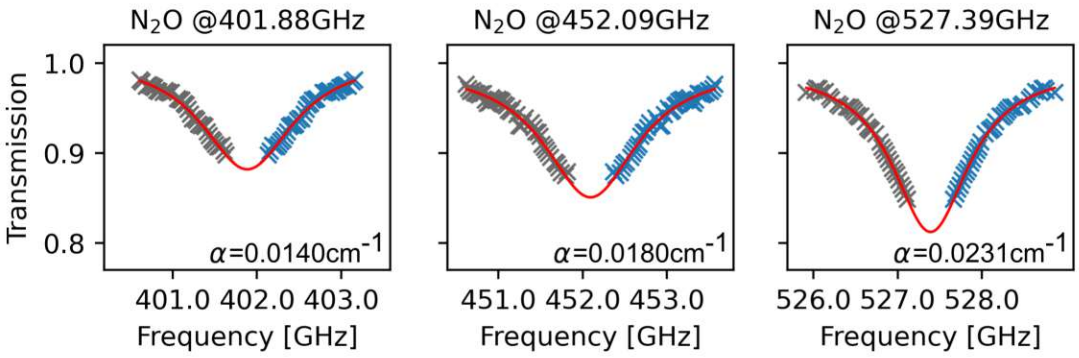

Figure A.4: Transmission measurements of nitrous oxide (N_2O) in the hollow waveguide gas cell Al-90-GaAs with the SB tuning method at 296 K at various pressures. Lorentzian fits (red lines) extract the absorption coefficients of the experimental data (blue crosses) and compare their individual transition line strengths as shown in chapter 6.5.1.

A.3 Nitrous Oxide Linewidth Measurements

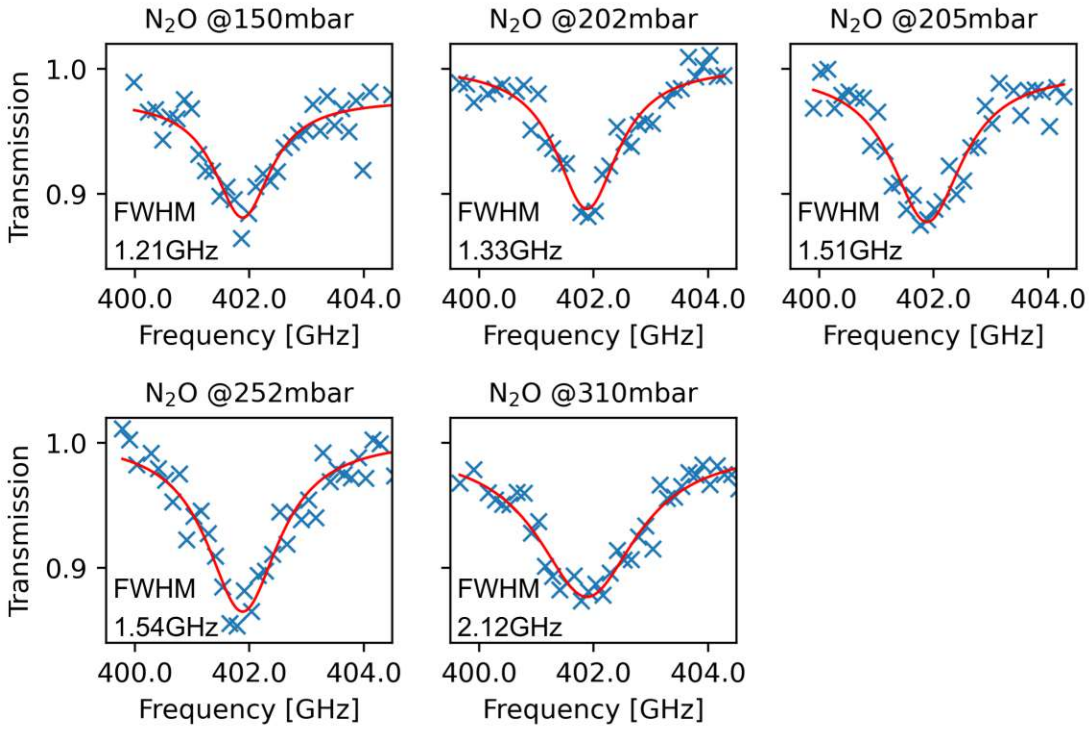

Figure A.5: Transmission measurements of nitrous oxide (N_2O) in the hollow waveguide gas cell Al-90-GaAs with the LD tuning method at 296 K at various pressures. Lorentzian fits (red lines) extract the linewidths of the experimental data (blue crosses) and reveal the pressure induced broadening of the N_2O transition as shown in chapter 6.5.2.

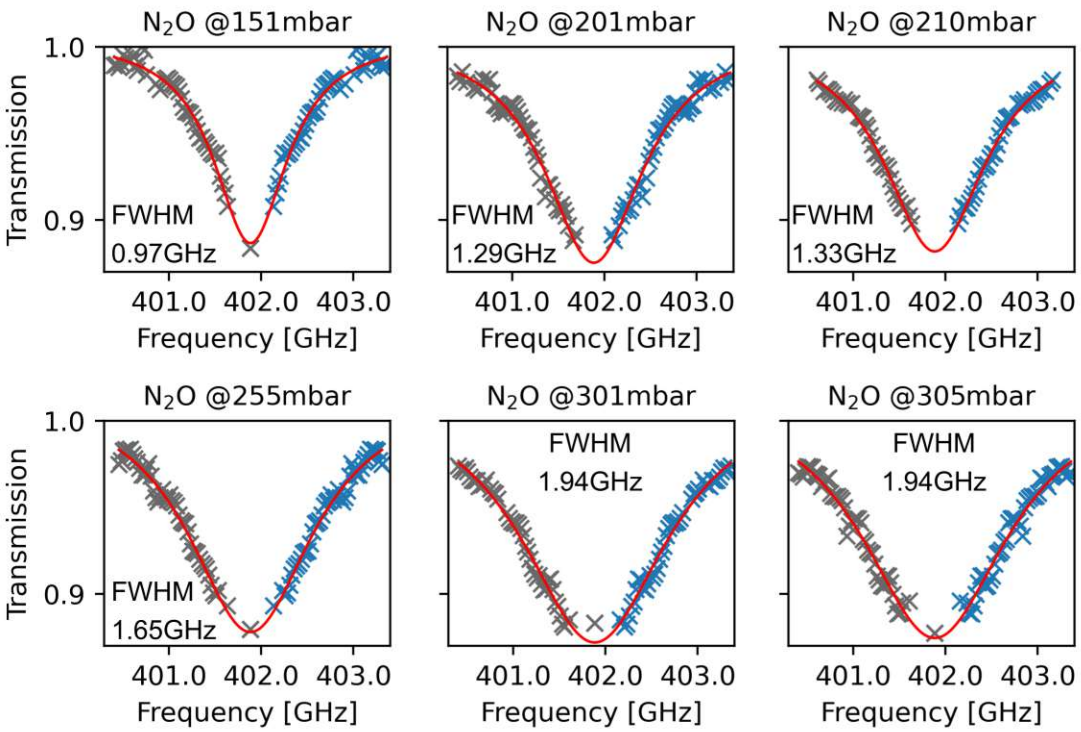

Figure A.6: Transmission measurements of nitrous oxide (N_2O) in the hollow waveguide gas cell Al-90-GaAs with the SB tuning method at 296 K at various pressures. Lorentzian fits (red lines) extract the linewidths of the experimental and reconstructed data (blue and grey crosses) and reveal the pressure induced broadening of the N_2O transition as shown in chapter 6.5.2.

Acknowledgments

In the end, I would like to take the opportunity to express my gratitude to the numerous people that supported me while working on my dissertation. First of all, I want to thank my supervisor Prof. Karl Unterrainer for the possibility to do a PhD in his research group and for his guidance during the last years. Moreover, I am very grateful to Juraj Darmo that I could participate in his scientific projects, for his advice and for his encouragement to think out of the box.

I am also thankful to all my fellow and former group members for the pleasant working atmosphere, their scientific input and their non-scientific company at the lunch breaks and after-work gatherings. I am beholden to Sebastian Schönhuber for introducing me to the terahertz field and to the group at the photonics institute and I thank Martin Kainz for always having an open ear to discuss any matter within his experience (and outside as well). I admire Benedikt Limbacher for his enormous knowledge of Python and his Blender skills, which he never hesitated to share and I would also like to thank him for many shared laughter while playing around with ChatGPT. Thanks also to Christian Derntl for sharing the office with me and to pass on his plants, from which the most still can be considered some kind of alive. Additionally, I like to thank Marie Ertl, Elias Plankenbichler, Lucas Grandits, Dmitry Polyushkin, Thomas Müller, Moritz Wenclawiak, Stefan Wachter, Matthias Paur, Aday Molina-Mendoza, Lukas Mennel, Florian Vogelbacher, Marko Cvejic and Simone Schuller for their welcoming attitude, shared music, football challenges, chess games, cake services, dish duties and general good company.

Furthermore, I am sincerely thankful that Michael Jaidl decided to study physics in the same year I did. It was a relief that you joined the same research group for your PhD after we did almost all exams together. So many hours of studying, raging about lab failures, fooling around, emotional support and choir rehearsals and meetings created a variety of memories in the last decade I will never forget. I would probably not be here writing my PhD thesis without your company. Which is also true for my former physics teacher and meanwhile good friend Mike, who kind of send me on this way during our philosophical discussions in class.

I would also like to thank Boris Mizaikoff and Michael Hlavatsch for providing the hollow waveguides for the sensing experiments and for a fruitful collaboration with many exciting project ideas. Fabian Dona, Andreas Kleinl and Mario Natale I thank for their help with any technical problem and their effort in the workshop. I am also grateful to Melanie Molnar and

Christina Huber for helping with all the administrative obstacles.

Last but not least, I am truly thankful for all my friends and family outside of the university, who accompanied me on my way and are always there for me. You all played a very crucial part in finishing this thesis. Most importantly, I would like to express my deepest gratitude to my parents Thomas and Kathi for their unconditional support and strong belief in all my projects throughout my whole life. Together with my siblings Magdalena, Christian, Veronika, my cousin Lukas (the great brother I ~~never~~ always had) and the whole family clan, you are one of the most important cornerstones in my life.

References

[1] S. S. Dhillon, M. S. Vitiello, E. H. Linfield, A. G. Davies, M. C. Hoffmann, J. Booske, C. Paoloni, M. Gensch, P. Weightman, G. P. Williams, E. Castro-Camus, D. R. S. Cumming, F. Simoens, I. Escorcia-Carranza, J. Grant, S. Lucyszyn, M. Kuwata-Gonokami, K. Konishi, M. Koch, C. A. Schmuttenmaer, T. L. Cocker, R. Huber, A. G. Markelz, Z. D. Taylor, V. P. Wallace, J. Axel Zeitler, J. Sibik, T. M. Korter, B. Ellison, S. Rea, P. Goldsmith, K. B. Cooper, R. Appleby, D. Pardo, P. G. Huggard, V. Krozer, H. Shams, M. Fice, C. Renaud, A. Seeds, A. Stöhr, M. Naftaly, N. Ridler, R. Clarke, J. E. Cunningham, and M. B. Johnston, "The 2017 terahertz science and technology roadmap," *Journal of Physics D: Applied Physics*, vol. 50, p. 043001, Feb. 2017.

[2] J. Lawall and E. Kessler, "Michelson interferometry with 10 pm accuracy," *Review of Scientific Instruments*, vol. 71, pp. 2669–2676, July 2000.

[3] M. Pisani, "A homodyne Michelson interferometer with sub-picometer resolution," *Measurement Science and Technology*, vol. 20, p. 084008, June 2009.

[4] J. Mandon, G. Guelachvili, and N. Picqué, "Fourier transform spectroscopy with a laser frequency comb," *Nature Photonics*, vol. 3, pp. 99–102, Feb. 2009.

[5] S. Bartalini, L. Consolino, P. Cancio, P. De Natale, P. Bartolini, A. Taschin, M. De Pas, H. Beere, D. Ritchie, M. Vitiello, and R. Torre, "Frequency-Comb-Assisted Terahertz Quantum Cascade Laser Spectroscopy," *Physical Review X*, vol. 4, p. 021006, Apr. 2014.

[6] S. Schiller, "Spectrometry with frequency combs," *Optics Letters*, vol. 27, pp. 766–768, May 2002.

[7] I. Coddington, N. Newbury, and W. Swann, "Dual-comb spectroscopy," *Optica*, vol. 3, pp. 414–426, Apr. 2016.

[8] L. A. Sterczewski, J. Westberg, Y. Yang, D. Burghoff, J. Reno, Q. Hu, and G. Wysocki, "Terahertz Spectroscopy of Gas Mixtures with Dual Quantum Cascade Laser Frequency Combs," *ACS Photonics*, vol. 7, pp. 1082–1087, May 2020.

[9] J. Fellinger, A. S. Mayer, G. Winkler, W. Grosinger, G.-W. Truong, S. Droste, C. Li, C. M. Heyl, I. Hartl, and O. H. Heckl, "Tunable dual-comb from an all-polarization-maintaining

single-cavity dual-color Yb:fiber laser," *Optics Express*, vol. 27, pp. 28062–28074, Sept. 2019.

[10] P. Jepsen, D. Cooke, and M. Koch, "Terahertz spectroscopy and imaging – Modern techniques and applications," *Laser & Photonics Reviews*, vol. 5, no. 1, pp. 124–166, 2011.

[11] R. Ulbricht, E. Hendry, J. Shan, T. F. Heinz, and M. Bonn, "Carrier dynamics in semiconductors studied with time-resolved terahertz spectroscopy," *Reviews of Modern Physics*, vol. 83, pp. 543–586, June 2011.

[12] J. Kröll, J. Darmo, S. S. Dhillon, X. Marcadet, M. Calligaro, C. Sirtori, and K. Unterrainer, "Phase-resolved measurements of stimulated emission in a laser," *Nature*, vol. 449, pp. 698–701, Oct. 2007.

[13] M. C. Hoffmann and J. A. Fülöp, "Intense ultrashort terahertz pulses: generation and applications," *Journal of Physics D: Applied Physics*, vol. 44, p. 083001, Feb. 2011.

[14] M. Theuer, S. S. Harsha, D. Molter, G. Torosyan, and R. Beigang, "Terahertz Time-Domain Spectroscopy of Gases, Liquids, and Solids," *ChemPhysChem*, vol. 12, no. 15, pp. 2695–2705, 2011.

[15] T. Kleine-Ostmann, P. Knobloch, M. Koch, S. Hoffmann, M. Breede, M. Hofmann, G. Hein, K. Pierz, M. Sperling, and K. Donhuijsen, "Continuous-wave THz imaging," *Electronics Letters*, vol. 37, pp. 1461–1463, Nov. 2001.

[16] C. Brenner, M. Hofmann, M. Scheller, M. K. Shakfa, M. Koch, I. C. Mayorga, A. Klehr, G. Erbert, and G. Tränkle, "Compact diode-laser-based system for continuous-wave and quasi-time-domain terahertz spectroscopy," *Optics Letters*, vol. 35, pp. 3859–3861, Dec. 2010.

[17] P. Verhoeve, E. Zwart, M. Versluis, M. Drabbels, J. J. ter Meulen, W. L. Meerts, A. Dymanus, and D. B. McLay, "A far infrared laser sideband spectrometer in the frequency region 550–2700 GHz," *Review of Scientific Instruments*, vol. 61, pp. 1612–1625, June 1990.

[18] K. M. Evenson, D. A. Jennings, and F. R. Petersen, "Tunable far-infrared spectroscopy," *Applied Physics Letters*, vol. 44, pp. 576–578, Mar. 1984.

[19] S. Matsuura, M. Tani, H. Abe, K. Sakai, H. Ozeki, and S. Saito, "High-Resolution Terahertz Spectroscopy by a Compact Radiation Source Based on Photomixing with Diode Lasers

in a Photoconductive Antenna," *Journal of Molecular Spectroscopy*, vol. 187, pp. 97–101, Jan. 1998.

[20] J. Waters, L. Froidevaux, R. Harwood, R. Jarnot, H. Pickett, W. Read, P. Siegel, R. Cofield, M. Filipiak, D. Flower, J. Holden, G. Lau, N. Livesey, G. Manney, H. Pumphrey, M. Santee, D. Wu, D. Cuddy, R. Lay, M. Loo, V. Perun, M. Schwartz, P. Stek, R. Thurstans, M. Boyles, K. Chandra, M. Chavez, G.-S. Chen, B. Chudasama, R. Dodge, R. Fuller, M. Girard, J. Jiang, Y. Jiang, B. Knosp, R. LaBelle, J. Lam, K. Lee, D. Miller, J. Oswald, N. Patel, D. Pukala, O. Quintero, D. Scaff, W. Van Snyder, M. Tope, P. Wagner, and M. Walch, "The Earth observing system microwave limb sounder (EOS MLS) on the aura Satellite," *IEEE Transactions on Geoscience and Remote Sensing*, vol. 44, pp. 1075–1092, May 2006.

[21] T. d. Graauw, F. P. Helmich, T. G. Phillips, J. Stutzki, E. Caux, N. D. Whyborn, P. Dieleman, P. R. Roelfsema, H. Aarts, R. Assendorp, R. Bachiller, W. Baechtold, A. Barcia, D. A. Beintema, V. Belitsky, A. O. Benz, R. Bieber, A. Boogert, C. Borys, B. Bumble, P. Caïs, M. Caris, P. Cerulli-Irelli, G. Chattopadhyay, S. Cherednichenko, M. Ciechanowicz, O. Coeur-Joly, C. Comito, A. Cros, A. d. Jonge, G. d. Lange, B. Delforges, Y. Delorme, T. d. Boggende, J.-M. Desbat, C. Diez-González, A. M. D. Giorgio, L. Dubbeldam, K. Edwards, M. Eggens, N. Erickson, J. Evers, M. Fich, T. Finn, B. Franke, T. Gaier, C. Gal, J. R. Gao, J.-D. Gallego, S. Gauffre, J. J. Gill, S. Glenz, H. Golstein, H. Goulooze, T. Gunsing, R. Güsten, P. Hartogh, W. A. Hatch, R. Higgins, E. C. Honingh, R. Huisman, B. D. Jackson, H. Jacobs, K. Jacobs, C. Jarchow, H. Javadi, W. Jellema, M. Justen, A. Karpov, C. Kasemann, J. Kawamura, G. Keizer, D. Kester, T. M. Klapwijk, T. Klein, E. Kollberg, J. Kooi, P.-P. Kooiman, B. Kopf, M. Krause, J.-M. Krieg, C. Kramer, B. Kruizenga, T. Kuhn, W. Laauwen, R. Lai, B. Larsson, H. G. Leduc, C. Leinz, R. H. Lin, R. Liseau, G. S. Liu, A. Loose, I. López-Fernandez, S. Lord, W. Luinge, A. Marston, J. Martín-Pintado, A. Maestrini, F. W. Maiwald, C. McCoey, I. Mehdi, A. Megej, M. Melchior, L. Meinsma, H. Merkel, M. Michalska, C. Monstein, D. Moratschke, P. Morris, H. Muller, J. A. Murphy, A. Naber, E. Natale, W. Nowosielski, F. Nuzzolo, M. Olberg, M. Olbrich, R. Orfei, P. Orleanski, V. Ossenkopf, T. Peacock, J. C. Pearson, I. Peron, S. Phillip-May, L. Piazzo, P. Planesas, M. Rataj, L. Ravera, C. Risacher, M. Salez, L. A. Samoska, P. Saraceno, R. Schieder, E. Schlecht, F. Schlöder, F. Schmülling, M. Schultz, K. Schuster, O. Siebertz, H. Smit, R. Szczerba, R. Shipman, E. Steinmetz, J. A. Stern, M. Stokroos, R. Teipen, D. Teyssier, T. Tils, N. Trappe, C. v. Baaren, B.-J. v. Leeuwen, H. v. d. Stadt, H. Visser, K. J. Wildeman, C. K. Wafelbakker, J. S. Ward, P. Wesselius, W. Wild, S. Wulff, H.-J. Wunsch, X. Tielens, P. Zaal, H. Zirath, J. Zmuidzinas, and

F. Zwart, "The Herschel-Heterodyne Instrument for the Far-Infrared (HIFI)," *Astronomy & Astrophysics*, vol. 518, p. L6, July 2010.

[22] U. U. Graf, S. Heyminck, R. Güsten, P. Hartogh, H.-W. Hübers, J. Stutzki, J. Faist, M. Fischer, K. Jacobs, M. Philipp, D. Rabanus, A. Semenov, P. v. d. Wal, A. Wagner-Gentner, C. Walther, and M. Wiedner, "GREAT: the German first light heterodyne instrument for SOFIA," in *Infrared Spaceborne Remote Sensing and Instrumentation XV*, vol. 6678, pp. 144–151, Sept. 2007.

[23] A. J. Seeds, H. Shams, M. J. Fice, and C. C. Renaud, "TeraHertz Photonics for Wireless Communications," *Journal of Lightwave Technology*, vol. 33, pp. 579–587, Feb. 2015.

[24] W. Saad, M. Bennis, and M. Chen, "A Vision of 6G Wireless Systems: Applications, Trends, Technologies, and Open Research Problems," *IEEE Network*, vol. 34, pp. 134–142, May 2020.

[25] M. J. Rosker and H. B. Wallace, "Imaging Through the Atmosphere at Terahertz Frequencies," in *2007 IEEE/MTT-S International Microwave Symposium*, pp. 773–776, June 2007.

[26] W. Idler, F. Buchali, L. Schmalen, E. Lach, R.-P. Braun, G. Böcherer, P. Schulte, and F. Steiner, "Field Trial of a 1 Tb/s Super-Channel Network Using Probabilistically Shaped Constellations," *Journal of Lightwave Technology*, vol. 35, pp. 1399–1406, Apr. 2017.

[27] C. Chaccour, M. N. Soorki, W. Saad, M. Bennis, P. Popovski, and M. Debbah, "Seven Defining Features of Terahertz (THz) Wireless Systems: A Fellowship of Communication and Sensing," *IEEE Communications Surveys & Tutorials*, vol. 24, no. 2, pp. 967–993, 2022.

[28] D. M. Mittleman, "Twenty years of terahertz imaging," *Optics Express*, vol. 26, pp. 9417–9431, Apr. 2018.

[29] G. J. Stacey, "THz Low Resolution Spectroscopy for Astronomy," *IEEE Transactions on Terahertz Science and Technology*, vol. 1, pp. 241–255, Sept. 2011.

[30] J. J. Lynch, P. A. Macdonald, H. P. Moyer, and R. G. Nagele, "Passive millimeter wave imaging sensors for commercial markets," *Applied Optics*, vol. 49, pp. E7–E12, July 2010.

[31] S. Augustin and H.-W. Hübers, "Phase-Sensitive Passive Terahertz Imaging at 5-m Stand-Off Distance," *IEEE Transactions on Terahertz Science and Technology*, vol. 4, pp. 418–424, July 2014.

[32] Y. H. Tao, A. J. Fitzgerald, and V. P. Wallace, "Non-Contact, Non-Destructive Testing in Various Industrial Sectors with Terahertz Technology," *Sensors*, vol. 20, p. 712, Jan. 2020.

[33] B. Borg, M. Dunn, A. Ang, and C. Villis, "The application of state-of-the-art technologies to support artwork conservation: Literature review," *Journal of Cultural Heritage*, vol. 44, pp. 239–259, July 2020.

[34] E. Abraham and K. Fukunaga, "Terahertz imaging applied to the examination of artistic objects," *Studies in Conservation*, vol. 60, pp. 343–352, Nov. 2015.

[35] K. Krügener, J. Ornik, L. M. Schneider, A. Jäckel, C. L. Koch-Dandolo, E. Castro-Camus, N. Riedl-Siedow, M. Koch, and W. Viöl, "Terahertz Inspection of Buildings and Architectural Art," *Applied Sciences*, vol. 10, p. 5166, Jan. 2020.

[36] B. M. Fischer, S. Wietzke, M. Reuter, O. Peters, R. Gente, C. Jansen, N. Vieweg, and M. Koch, "Investigating Material Characteristics and Morphology of Polymers Using Terahertz Technologies," *IEEE Transactions on Terahertz Science and Technology*, vol. 3, pp. 259–268, May 2013.

[37] N. Karpowicz, H. Zhong, C. Zhang, K.-I. Lin, J.-S. Hwang, J. Xu, and X.-C. Zhang, "Compact continuous-wave subterahertz system for inspection applications," *Applied Physics Letters*, vol. 86, p. 054105, Jan. 2005.

[38] S. Krimi, J. Klier, J. Jonuscheit, G. von Freymann, R. Urbansky, and R. Beigang, "Highly accurate thickness measurement of multi-layered automotive paints using terahertz technology," *Applied Physics Letters*, vol. 109, p. 021105, July 2016.

[39] K. Ahi, S. Shahbazmohamadi, and N. Asadizanjani, "Quality control and authentication of packaged integrated circuits using enhanced-spatial-resolution terahertz time-domain spectroscopy and imaging," *Optics and Lasers in Engineering*, vol. 104, pp. 274–284, May 2018.

[40] R. Appleby and H. B. Wallace, "Standoff Detection of Weapons and Contraband in the 100 GHz to 1 THz Region," *IEEE Transactions on Antennas and Propagation*, vol. 55, pp. 2944–2956, Nov. 2007.

[41] K. B. Cooper, R. J. Dengler, N. Llombart, B. Thomas, G. Chattopadhyay, and P. H. Siegel, "THz Imaging Radar for Standoff Personnel Screening," *IEEE Transactions on Terahertz Science and Technology*, vol. 1, pp. 169–182, Sept. 2011.

[42] A. G. Davies, A. D. Burnett, W. Fan, E. H. Linfield, and J. E. Cunningham, "Terahertz spectroscopy of explosives and drugs," *Materials Today*, vol. 11, pp. 18–26, Mar. 2008.

[43] W. Zhang, Y. Tang, A. Shi, L. Bao, Y. Shen, R. Shen, and Y. Ye, "Recent Developments in Spectroscopic Techniques for the Detection of Explosives," *Materials*, vol. 11, p. 1364, Aug. 2018.

[44] Q. Sun, Y. He, K. Liu, S. Fan, E. P. J. Parrott, and E. Pickwell-MacPherson, "Recent advances in terahertz technology for biomedical applications," *Quantitative Imaging in Medicine and Surgery*, vol. 7, pp. 34555–34355, June 2017.

[45] J.-H. Son, S. J. Oh, and H. Cheon, "Potential clinical applications of terahertz radiation," *Journal of Applied Physics*, vol. 125, p. 190901, May 2019.

[46] A. D'Arco, M. Di Fabrizio, V. Dolci, M. Petrarca, and S. Lupi, "THz Pulsed Imaging in Biomedical Applications," *Condensed Matter*, vol. 5, p. 25, June 2020.

[47] L. Afsah-Hejri, E. Akbari, A. Toudeshki, T. Homayouni, A. Alizadeh, and R. Ehsani, "Terahertz spectroscopy and imaging: A review on agricultural applications," *Computers and Electronics in Agriculture*, vol. 177, p. 105628, Oct. 2020.

[48] L. Afsah-Hejri, P. Hajeb, P. Ara, and R. J. Ehsani, "A Comprehensive Review on Food Applications of Terahertz Spectroscopy and Imaging," *Comprehensive Reviews in Food Science and Food Safety*, vol. 18, no. 5, pp. 1563–1621, 2019.

[49] C. Thacker, A. Cooray, J. Smidt, F. De Bernardis, K. Mitchell-Wynne, A. Amblard, R. Auld, M. Baes, D. L. Clements, A. Dariush, G. De Zotti, L. Dunne, S. Eales, R. Hopwood, C. Hoyos, E. Ibar, M. Jarvis, S. Maddox, M. J. Michałowski, E. Pascale, D. Scott, S. Serjeant, M. W. L. Smith, E. Valiante, and P. van der Werf, "H-ATLAS: THE COSMIC ABUNDANCE OF DUST FROM THE FAR-INFRARED BACKGROUND POWER SPECTRUM," *The Astrophysical Journal*, vol. 768, p. 58, Apr. 2013.

[50] E. Bründermann, H.-W. Hubers, and M. F. Kimmitt, *Terahertz techniques*. No. 151 in Springer series in optical sciences, Springer, 2010.

[51] H. Rubens and R. Wood, "XXVII. *Focal isolation of long heat-waves*," *The London, Edinburgh, and Dublin Philosophical Magazine and Journal of Science*, vol. 21, pp. 249–261, Feb. 1911.

[52] J. H. Booske, R. J. Dobbs, C. D. Joye, C. L. Kory, G. R. Neil, G.-S. Park, J. Park, and R. J. Temkin, "Vacuum Electronic High Power Terahertz Sources," *IEEE Transactions on Terahertz Science and Technology*, vol. 1, pp. 54–75, Sept. 2011.

[53] R. Kompfner and N. Williams, "Backward-Wave Tubes," *Proceedings of the IRE*, vol. 41, pp. 1602–1611, Nov. 1953.

[54] B. Gorshunov, A. Volkov, I. Spektor, A. Prokhorov, A. Mukhin, M. Dressel, S. Uchida, and A. Loidl, "Terahertz BWO-Spectrosopy," *International Journal of Infrared and Millimeter Waves*, vol. 26, pp. 1217–1240, Sept. 2005.

[55] G. P. Williams, "Filling the THz gap—high power sources and applications," *Reports on Progress in Physics*, vol. 69, pp. 301–326, Feb. 2006.

[56] T. Nakazato, M. Oyamada, N. Niimura, S. Urasawa, O. Konno, A. Kagaya, R. Kato, T. Kamiyama, Y. Torizuka, T. Nanba, Y. Kondo, Y. Shibata, K. Ishi, T. Ohsaka, and M. Ikezawa, "Observation of coherent synchrotron radiation," *Physical Review Letters*, vol. 63, pp. 1245–1248, Sept. 1989.

[57] H. Freund and G. Neil, "Free-electron lasers: vacuum electronic generators of coherent radiation," *Proceedings of the IEEE*, vol. 87, pp. 782–803, May 1999.

[58] P. Emma, R. Akre, J. Arthur, R. Bionta, C. Bostedt, J. Bozek, A. Brachmann, P. Bucksbaum, R. Coffee, F.-J. Decker, Y. Ding, D. Dowell, S. Edstrom, A. Fisher, J. Frisch, S. Gilevich, J. Hastings, G. Hays, P. Hering, Z. Huang, R. Iverson, H. Loos, M. Messerschmidt, A. Miahnahri, S. Moeller, H.-D. Nuhn, G. Pile, D. Ratner, J. Rzepiela, D. Schultz, T. Smith, P. Stefan, H. Tompkins, J. Turner, J. Welch, W. White, J. Wu, G. Yocky, and J. Galayda, "First lasing and operation of an ångstrom-wavelength free-electron laser," *Nature Photonics*, vol. 4, pp. 641–647, Sept. 2010.

[59] R. Lai, X. B. Mei, W. R. Deal, W. Yoshida, Y. M. Kim, P. H. Liu, J. Lee, J. Uyeda, V. Radisic, M. Lange, T. Gaier, L. Samoska, and A. Fung, "Sub 50 nm InP HEMT Device with Fmax Greater than 1 THz," in *2007 IEEE International Electron Devices Meeting*, pp. 609–611, 2007.

[60] Y. Tang, K. Shinohara, D. Regan, A. Corrion, D. Brown, J. Wong, A. Schmitz, H. Fung, S. Kim, and M. Micovic, "Ultrahigh-Speed GaN High-Electron-Mobility Transistors With f_T/f_{max} of 454/444 GHz," *IEEE Electron Device Letters*, vol. 36, pp. 549–551, June 2015.

[61] W. Deal, X. B. Mei, K. M. K. H. Leong, V. Radisic, S. Sarkozy, and R. Lai, "THz Monolithic Integrated Circuits Using InP High Electron Mobility Transistors," *IEEE Transactions on Terahertz Science and Technology*, vol. 1, pp. 25–32, Sept. 2011.

[62] A. Maestrini, J. S. Ward, J. J. Gill, C. Lee, B. Thomas, R. H. Lin, G. Chattopadhyay, and I. Mehdi, "A Frequency-Multiplied Source With More Than 1 mW of Power Across the 840–900-GHz Band," *IEEE Transactions on Microwave Theory and Techniques*, vol. 58, pp. 1925–1932, July 2010.

[63] A. Maestrini, I. Mehdi, J. V. Siles, J. S. Ward, R. Lin, B. Thomas, C. Lee, J. Gill, G. Chattopadhyay, E. Schlecht, J. Pearson, and P. Siegel, "Design and Characterization of a Room Temperature All-Solid-State Electronic Source Tunable From 2.48 to 2.75 THz," *IEEE Transactions on Terahertz Science and Technology*, vol. 2, pp. 177–185, Mar. 2012.

[64] B. J. Drouin, F. W. Maiwald, and J. C. Pearson, "Application of cascaded frequency multiplication to molecular spectroscopy," *Review of Scientific Instruments*, vol. 76, p. 093113, Sept. 2005.

[65] T. Maekawa, H. Kanaya, S. Suzuki, and M. Asada, "Oscillation up to 1.92 THz in resonant tunneling diode by reduced conduction loss," *Applied Physics Express*, vol. 9, p. 024101, Feb. 2016.

[66] K. Kasagi, S. Suzuki, and M. Asada, "Large-scale array of resonant-tunneling-diode terahertz oscillators for high output power at 1 THz," *Journal of Applied Physics*, vol. 125, p. 151601, Apr. 2019.

[67] E. Alekseev and D. Pavlidis, "GaN Gunn diodes for THz signal generation," in *2000 IEEE MTT-S International Microwave Symposium Digest*, vol. 3, pp. 1905–1908, 2000.

[68] A. Acharyya and J. P. Banerjee, "Prospects of IMPATT devices based on wide bandgap semiconductors as potential terahertz sources," *Applied Nanoscience*, vol. 4, pp. 1–14, Jan. 2014.

[69] J. Nishizawa, P. Płotka, T. Kurabayashi, and H. Makabe, "706-GHz GaAs CW fundamental-mode TUNNETT diodes fabricated with molecular layer epitaxy," *physica status solidi c*, vol. 5, no. 9, pp. 2802–2804, 2008.

[70] G. Dodel, "On the history of far-infrared (FIR) gas lasers: Thirty-five years of research and application," *Infrared Physics & Technology*, vol. 40, pp. 127–139, June 1999.

[71] P. Chevalier, A. Amirzhan, F. Wang, M. Piccardo, S. G. Johnson, F. Capasso, and H. O. Everitt, "Widely tunable compact terahertz gas lasers," *Science*, vol. 366, pp. 856–860, Nov. 2019.

[72] H. Maeda and T. Kurosawa, "Hot Electron Population Inversion in Crossed Electric and Magnetic Fields," *Journal of the Physical Society of Japan*, vol. 33, pp. 562–562, Aug. 1972.

[73] E. Bründermann, "Widely Tunable Far-Infrared Hot-Hole Semiconductor Lasers," in *Long-Wavelength Infrared Semiconductor Lasers*, pp. 279–350, John Wiley & Sons, Ltd, 2004.

[74] J. Faist, F. Capasso, D. L. Sivco, C. Sirtori, A. L. Hutchinson, and A. Y. Cho, "Quantum Cascade Laser," *Science*, vol. 264, pp. 553–556, Apr. 1994.

[75] R. Köhler, A. Tredicucci, F. Beltram, H. E. Beere, E. H. Linfield, A. G. Davies, D. A. Ritchie, R. C. Iotti, and F. Rossi, "Terahertz semiconductor-heterostructure laser," *Nature*, vol. 417, pp. 156–159, May 2002.

[76] G. Scalari, C. Walther, M. Fischer, R. Terazzi, H. Beere, D. Ritchie, and J. Faist, "THz and sub-THz quantum cascade lasers," *Laser & Photonics Reviews*, vol. 3, no. 1-2, pp. 45–66, 2009.

[77] M. Wienold, B. Röben, X. Lü, G. Rozas, L. Schrottke, K. Biermann, and H. T. Grahn, "Frequency dependence of the maximum operating temperature for quantum-cascade lasers up to 5.4 THz," *Applied Physics Letters*, vol. 107, p. 202101, Nov. 2015.

[78] L. Li, L. Chen, J. Freeman, M. Salih, P. Dean, A. Davies, and E. Linfield, "Multi-Watt high-power THz frequency quantum cascade lasers," *Electronics Letters*, vol. 53, no. 12, pp. 799–800, 2017.

[79] A. Khalatpour, A. K. Paulsen, C. Deimert, Z. R. Wasilewski, and Q. Hu, "High-power portable terahertz laser systems," *Nature Photonics*, vol. 15, pp. 16–20, Jan. 2021.

[80] H.-W. Hübers, S. G. Pavlov, H. Richter, A. D. Semenov, L. Mahler, A. Tredicucci, H. E. Beere, and D. A. Ritchie, "High-resolution gas phase spectroscopy with a distributed feedback terahertz quantum cascade laser," *Applied Physics Letters*, vol. 89, p. 061115, Aug. 2006.

[81] F. Zernike and P. R. Berman, "Generation of Far Infrared as a Difference Frequency," *Physical Review Letters*, vol. 15, pp. 999–1001, Dec. 1965.

[82] Y. J. Ding, "Progress in terahertz sources based on difference-frequency generation," *JOSA B*, vol. 31, pp. 2696–2711, Nov. 2014.

[83] M. A. Belkin, F. Capasso, A. Belyanin, D. L. Sivco, A. Y. Cho, D. C. Oakley, C. J. Vineis, and G. W. Turner, "Terahertz quantum-cascade-laser source based on intracavity difference-frequency generation," *Nature Photonics*, vol. 1, pp. 288–292, May 2007.

[84] K. Fujita, S. Jung, Y. Jiang, J. H. Kim, A. Nakanishi, A. Ito, M. Hitaka, T. Edamura, and M. A. Belkin, "Recent progress in terahertz difference-frequency quantum cascade laser sources," *Nanophotonics*, vol. 7, pp. 1795–1817, Nov. 2018.

[85] T. Nagatsuma, H. Ito, and T. Ishibashi, "High-power RF photodiodes and their applications," *Laser & Photonics Reviews*, vol. 3, no. 1-2, pp. 123–137, 2009.

[86] E. R. Brown, F. W. Smith, and K. A. McIntosh, "Coherent millimeter-wave generation by heterodyne conversion in low-temperature-grown GaAs photoconductors," *Journal of Applied Physics*, vol. 73, pp. 1480–1484, Feb. 1993.

[87] E. R. Brown, K. A. McIntosh, K. B. Nichols, and C. L. Dennis, "Photomixing up to 3.8 THz in low-temperature-grown GaAs," *Applied Physics Letters*, vol. 66, pp. 285–287, Jan. 1995.

[88] S. Preu, S. Malzer, G. H. Döhler, J. Zhang, Z. H. Lu, and L. J. Wang, "Highly collimated and directional continous-wave Terahertz emission by photomixing in semiconductor device arrays," in *Millimeter-Wave and Terahertz Photonics*, vol. 6194, pp. 111–119, SPIE, Apr. 2006.

[89] M. Musha, A. Ueda, M. Horikoshi, K. Nakagawa, M. Ishiguro, K.-i. Ueda, and H. Ito, "A highly stable mm-wave synthesizer realized by mixing two lasers locked to an optical frequency comb generator," *Optics Communications*, vol. 240, pp. 201–208, Oct. 2004.

[90] C.-S. Friedrich, C. Brenner, S. Hoffmann, A. Schmitz, I. C. Mayorga, A. Klehr, G. Erbert, and M. R. Hofmann, "New Two-Color Laser Concepts for THz Generation," *IEEE Journal of Selected Topics in Quantum Electronics*, vol. 14, pp. 270–276, Mar. 2008.

[91] S. Hoffmann and M. Hofmann, "Generation of Terahertz radiation with two color semiconductor lasers," *Laser & Photonics Reviews*, vol. 1, no. 1, pp. 44–56, 2007.

[92] S. Preu, G. H. Döhler, S. Malzer, L. J. Wang, and A. C. Gossard, "Tunable, continuous-wave Terahertz photomixer sources and applications," *Journal of Applied Physics*, vol. 109, p. 061301, Mar. 2011.

[93] R. Safian, G. Ghazi, and N. Mohammadian, "Review of photomixing continuous-wave terahertz systems and current application trends in terahertz domain," *Optical Engineering*, vol. 58, p. 110901, Nov. 2019.

[94] R. A. Lewis, "A review of terahertz detectors," *Journal of Physics D: Applied Physics*, vol. 52, p. 433001, Aug. 2019.

[95] F. J. Low, "Low-Temperature Germanium Bolometer," *JOSA*, vol. 51, pp. 1300–1304, Nov. 1961.

[96] M. A. Kinch, "Compensated Silicon-Impurity Conduction Bolometer," *Journal of Applied Physics*, vol. 42, pp. 5861–5863, Dec. 1971.

[97] G. N. Gol'tsman, A. D. Semenov, Y. P. Gousev, M. A. Zorin, I. G. Godidze, E. M. Gershenzon, P. T. Lang, W. J. Knott, and K. F. Renk, "Sensitive picosecond NbN detector for radiation from millimetre wavelengths to visible light," *Superconductor Science and Technology*, vol. 4, p. 453, Sept. 1991.

[98] A. Hossain and M. Rashid, "Pyroelectric detectors and their applications," *IEEE Transactions on Industry Applications*, vol. 27, pp. 824–829, Sept. 1991.

[99] M. J. E. Golay, "A Pneumatic Infra-Red Detector," *Review of Scientific Instruments*, vol. 18, pp. 357–362, May 1947.

[100] G. Chen, "Thermoelectric Energy Conversion: Materials, Devices, and Systems," *Journal of Physics: Conference Series*, vol. 660, p. 012066, Nov. 2015.

[101] S. J. Fray and J. F. C. Oliver, "Photoconductive detector of radiation of wavelength greater than 50 ," *Journal of Scientific Instruments*, vol. 36, p. 195, Apr. 1959.

[102] W. J. Moore and H. Shenker, "A high-detectivity gallium-doped germanium detector for the 40–120 region," *Infrared Physics*, vol. 5, pp. 99–106, Sept. 1965.

[103] F. A. Hegmann, J. B. Williams, B. Cole, M. S. Sherwin, J. W. Beeman, and E. E. Haller, "Time-resolved photoresponse of a gallium-doped germanium photoconductor using a variable pulse-width terahertz source," *Applied Physics Letters*, vol. 76, pp. 262–264, Jan. 2000.

[104] N. M. Haegel, E. E. Haller, and P. N. Luke, "Performance and materials aspects of Ge:Be photoconductors," *International Journal of Infrared and Millimeter Waves*, vol. 4, pp. 945–954, Nov. 1983.

[105] G. D. Peskett and B. V. Rollin, "Energy Exchange between Hot Carriers and the Lattice in Indium Antimonide," *Proceedings of the Physical Society*, vol. 82, p. 467, Sept. 1963.

[106] G. Strasser, K. Bochter, M. Witzany, and E. Gornik, "Improved tunable InSb FIR detectors," *Infrared Physics*, vol. 32, pp. 439–442, Jan. 1991.

[107] L. Liu, J. L. Hesler, H. Xu, A. W. Lichtenberger, and R. M. Weikle, "A Broadband Quasi-Optical Terahertz Detector Utilizing a Zero Bias Schottky Diode," *IEEE Microwave and Wireless Components Letters*, vol. 20, pp. 504–506, Sept. 2010.

[108] F. Rettich, N. Vieweg, O. Cojocari, and A. Deninger, "Field Intensity Detection of Individual Terahertz Pulses at 80 MHz Repetition Rate," *Journal of Infrared, Millimeter, and Terahertz Waves*, vol. 36, pp. 607–612, July 2015.

[109] M. Feiginov, "Frequency Limitations of Resonant-Tunnelling Diodes in Sub-THz and THz Oscillators and Detectors," *Journal of Infrared, Millimeter, and Terahertz Waves*, vol. 40, pp. 365–394, Apr. 2019.

[110] X. G. Guo, J. C. Cao, R. Zhang, Z. Y. Tan, and H. C. Liu, "Recent Progress in Terahertz Quantum-Well Photodetectors," *IEEE Journal of Selected Topics in Quantum Electronics*, vol. 19, pp. 8500508–8500508, Jan. 2013.

[111] F. R. Giorgetta, E. Baumann, M. Graf, Q. Yang, C. Manz, K. Kohler, H. E. Beere, D. A. Ritchie, E. Linfield, A. G. Davies, Y. Fedoryshyn, H. Jackel, M. Fischer, J. Faist, and D. Hofstetter, "Quantum Cascade Detectors," *IEEE Journal of Quantum Electronics*, vol. 45, pp. 1039–1052, Aug. 2009.

[112] H. Li, W.-J. Wan, Z.-Y. Tan, Z.-L. Fu, H.-X. Wang, T. Zhou, Z.-P. Li, C. Wang, X.-G. Guo, and J.-C. Cao, "6.2-GHz modulated terahertz light detection using fast terahertz quantum well photodetectors," *Scientific Reports*, vol. 7, p. 3452, June 2017.

[113] W. Knap, F. Teppe, Y. Meziani, N. Dyakonova, J. Lusakowski, F. Boeuf, T. Skotnicki, D. Maude, S. Rumyantsev, and M. S. Shur, "Plasma wave detection of sub-terahertz and terahertz radiation by silicon field-effect transistors," *Applied Physics Letters*, vol. 85, pp. 675–677, July 2004.

[114] S. Kim, D.-W. Park, K.-Y. Choi, and S.-G. Lee, "MOSFET Characteristics for Terahertz Detector Application From On-Wafer Measurement," *IEEE Transactions on Terahertz Science and Technology*, vol. 5, pp. 1068–1077, Nov. 2015.

[115] E. Javadi, A. Lisauskas, M. Shahabadi, N. Masoumi, J. Zhang, J. Matukas, and H. G. Roskos, "Terahertz Detection With a Low-Cost Packaged GaAs High-Electron-Mobility Transistor," *IEEE Transactions on Terahertz Science and Technology*, vol. 9, pp. 27–37, Jan. 2019.

[116] S. Suzuki, T. Nukariya, Y. Ueda, T. Otsuka, and M. Asada, "High Current Responsivity and Wide Modulation Bandwidth Terahertz Detector Using High-Electron-Mobility Transistor for Wireless Communication," *Journal of Infrared, Millimeter, and Terahertz Waves*, vol. 37, pp. 658–667, July 2016.

[117] L. Vicarelli, M. S. Vitiello, D. Coquillat, A. Lombardo, A. C. Ferrari, W. Knap, M. Polini, V. Pellegrini, and A. Tredicucci, "Graphene field-effect transistors as room-temperature terahertz detectors," *Nature Materials*, vol. 11, pp. 865–871, Oct. 2012.

[118] M. S. Vitiello, D. Coquillat, L. Viti, D. Ercolani, F. Teppe, A. Pitanti, F. Beltram, L. Sorba, W. Knap, and A. Tredicucci, "Room-Temperature Terahertz Detectors Based on Semiconductor Nanowire Field-Effect Transistors," *Nano Letters*, vol. 12, pp. 96–101, Jan. 2012.

[119] H. P. Röser, H. W. Hübers, T. W. Crowe, and W. C. B. Peatman, "Nanostructure GaAS Schottky diodes for far-infrared heterodyne receivers," *Infrared Physics & Technology*, vol. 35, pp. 451–462, Mar. 1994.

[120] P. L. Richards, T. M. Shen, R. E. Harris, and F. L. Lloyd, "Quasiparticle heterodyne mixing in SIS tunnel junctions," *Applied Physics Letters*, vol. 34, pp. 345–347, Mar. 1979.

[121] G. Gol'tsman, B. Karasik, O. Okunev, A. Dzardanov, E. Gershenzon, H. Ekstrom, S. Jacobsson, and E. Kollberg, "NbN hot electron superconducting mixers for 100 GHz operation," *IEEE Transactions on Applied Superconductivity*, vol. 5, pp. 3065–3068, June 1995.

[122] A. D. Semenov, H.-W. Hübers, H. Richter, M. Birk, M. Krocka, U. Mair, K. Smirnov, G. N. Gol'tsman, and B. M. Voronov, "2.5 THz heterodyne receiver with NbN hot-electron-bolometer mixer," *Physica C: Superconductivity*, vol. 372-376, pp. 448–453, Aug. 2002.

[123] S. M. Duffy, S. Verghese, and K. A. McIntosh, "Photomixers for Continuous-Wave Terahertz Radiation," in *Sensing with Terahertz Radiation* (D. Mittleman, ed.), Springer Series in Optical Sciences, pp. 193–236, Springer, 2003.

[124] S. Verghese, K. McIntosh, and E. Brown, "Highly tunable fiber-coupled photomixers with coherent terahertz output power," *IEEE Transactions on Microwave Theory and Techniques*, vol. 45, pp. 1301–1309, Aug. 1997.

[125] M. Tani, O. Morikawa, S. Matsuura, and M. Hangyo, "Generation of terahertz radiation by photomixing with dual- and multiple-mode lasers," *Semiconductor Science and Technology*, vol. 20, p. S151, June 2005.

[126] S. Preu, G. H. Döhler, S. Malzer, A. Stöhr, V. Rymanov, T. Göbel, E. R. Brown, M. Feiginov, R. Gonzalo, M. Beruete, and M. Navarro-Cía, "Principles of THz Generation," in *Semiconductor Terahertz Technology*, pp. 3–68, John Wiley & Sons, Ltd, 2015.

[127] F. L. Constantin, "Phase-Coherent Heterodyne Detection in the Terahertz Regime With a Photomixer," *IEEE Journal of Quantum Electronics*, vol. 47, pp. 1458–1462, Nov. 2011.

[128] L. Nickelson, "Rectangular Hollow Metallic Waveguides and Resonators," in *Electromagnetic Theory and Plasmonics for Engineers* (L. Nickelson, ed.), pp. 425–543, Springer, 2019.

[129] E. Jensen, "Cavity basics," Jan. 2012. arXiv:1201.3202.

[130] P. R. Griffiths and J. A. de Haseth, "Introduction to Vibrational Spectroscopy," in *Fourier Transform Infrared Spectrometry*, pp. 1–18, John Wiley & Sons, Ltd, 2007.

[131] C. Banwell, *Fundamentals of Molecular Spectroscopy*. McGraw-Hill Education, 4th edition ed., 1994.

[132] J. M. Hollas, *Modern spectroscopy*. J. Wiley, 4th ed ed., 2004.

[133] I. E. Gordon, L. S. Rothman, R. J. Hargreaves, R. Hashemi, E. V. Karlovets, F. M. Skinner, E. K. Conway, C. Hill, R. V. Kochanov, Y. Tan, P. Wcisło, A. A. Finenko, K. Nelson, P. F. Bernath, M. Birk, V. Boudon, A. Campargue, K. V. Chance, A. Coustenis, B. J. Drouin, J.-M. Flaud, R. R. Gamache, J. T. Hodges, D. Jacquemart, E. J. Mlawer, A. V. Nikitin, V. I. Perevalov, M. Rotger, J. Tennyson, G. C. Toon, H. Tran, V. G. Tyuterev, E. M. Adkins, A. Baker, A. Barbe, E. Canè, A. G. Császár, A. Dudaryonok, O. Egorov, A. J. Fleisher, H. Fleurbaey, A. Foltynowicz, T. Furtenbacher, J. J. Harrison, J.-M. Hartmann, V.-M. Horneman, X. Huang, T. Karman, J. Karns, S. Kassi, I. Kleiner, V. Kofman, F. Kwabia–Tchana, N. N. Lavrentieva, T. J. Lee, D. A. Long, A. A. Lukashevskaya, O. M. Lyulin, V. Y. Makhnev, W. Matt, S. T. Massie, M. Melosso, S. N. Mikhailenko, D. Mondelain, H. S. P. Müller, O. V. Naumenko, A. Perrin, O. L. Polyansky, E. Raddaoui, P. L. Raston, Z. D. Reed, M. Rey, C. Richard, R. Tóbiás, I. Sadiek, D. W. Schwenke, E. Starikova, K. Sung, F. Tamassia, S. A. Tashkun, J. Vander Auwera, I. A. Vasilenko, A. A. Vigasin, G. L. Villanueva, B. Vispoel, G. Wagner, A. Yachmenev, and S. N. Yurchenko, "The HITRAN2020 molecular spectroscopic database," *Journal of Quantitative Spectroscopy and Radiative Transfer*, vol. 277, p. 107949, Jan. 2022.

[134] I. Azuri, A. Hirsch, A. M. Reilly, A. Tkatchenko, S. Kendler, O. Hod, and L. Kronik, "Terahertz spectroscopy of 2,4,6-trinitrotoluene molecular solids from first principles," *Beilstein Journal of Organic Chemistry*, vol. 14, pp. 381–388, Feb. 2018.

[135] U. Pöschl, "Atmospheric Aerosols: Composition, Transformation, Climate and Health Effects," *Angewandte Chemie International Edition*, vol. 44, no. 46, pp. 7520–7540, 2005.

[136] A. Cuisset, F. Hindle, G. Mouret, R. Bocquet, J. Bruckhuisen, J. Decker, A. Pienkina, C. Bray, Fertein, and V. Boudon, "Terahertz Rotational Spectroscopy of Greenhouse Gases Using Long Interaction Path-Lengths," *Applied Sciences*, vol. 11, p. 1229, Jan. 2021.

[137] N. Rothbart, O. Holz, R. Koczulla, K. Schmalz, and H.-W. Hübers, "Analysis of Human Breath by Millimeter-Wave/Terahertz Spectroscopy," *Sensors*, vol. 19, p. 2719, Jan. 2019.

[138] M. Hlavatsch, S. Klingler, and B. Mizaikoff, "Infrared Sensing Strategies: Toward Smart Diagnostics for Exhaled Breath Analysis," in *Breath Analysis : An Approach for Smart Diagnostics* (S. Weigl, ed.), Bioanalytical Reviews, pp. 73–100, Springer International Publishing, 2023.

[139] L. E. Hargrove, R. L. Fork, and M. A. Pollack, "LOCKING OF He–Ne LASER MODES INDUCED BY SYNCHRONOUS INTRACAVITY MODULATION," *Applied Physics Letters*, vol. 5, pp. 4–5, July 1964.

[140] T. Udem, R. Holzwarth, and T. W. Hänsch, "Optical frequency metrology," *Nature*, vol. 416, pp. 233–237, Mar. 2002.

[141] T. Fortier and E. Baumann, "20 years of developments in optical frequency comb technology and applications," *Communications Physics*, vol. 2, pp. 1–16, Dec. 2019.

[142] S. A. Diddams, K. Vahala, and T. Udem, "Optical frequency combs: Coherently uniting the electromagnetic spectrum," *Science*, vol. 369, p. eaay3676, July 2020.

[143] T. W. Hänsch, "Nobel Lecture: Passion for precision," *Reviews of Modern Physics*, vol. 78, pp. 1297–1309, Nov. 2006.

[144] J. L. Hall, "Nobel Lecture: Defining and measuring optical frequencies," *Reviews of Modern Physics*, vol. 78, pp. 1279–1295, Nov. 2006.

[145] N. Picqué and T. W. Hänsch, "Frequency comb spectroscopy," *Nature Photonics*, vol. 13, pp. 146–157, Mar. 2019.

[146] S. A. Diddams, "The evolving optical frequency comb," *JOSA B*, vol. 27, pp. B51–B62, Nov. 2010.

[147] J. Reichert, R. Holzwarth, T. Udem, and T. W. Hänsch, "Measuring the frequency of light with mode-locked lasers," *Optics Communications*, vol. 172, pp. 59–68, Dec. 1999.

[148] H. Telle, G. Steinmeyer, A. Dunlop, J. Stenger, D. Sutter, and U. Keller, "Carrier-envelope offset phase control: A novel concept for absolute optical frequency measurement and ultrashort pulse generation," *Applied Physics B*, vol. 69, pp. 327–332, Oct. 1999.

[149] S. T. Cundiff and J. Ye, "Colloquium: Femtosecond optical frequency combs," *Reviews of Modern Physics*, vol. 75, pp. 325–342, Mar. 2003.

[150] D. E. Spence, P. N. Kean, and W. Sibbett, "60-fsec pulse generation from a self-mode-locked Ti:sapphire laser," *Optics Letters*, vol. 16, pp. 42–44, Jan. 1991.

[151] S. Droste, G. Ycas, B. R. Washburn, I. Coddington, and N. R. Newbury, "Optical Frequency Comb Generation based on Erbium Fiber Lasers," *Nanophotonics*, vol. 5, pp. 196–213, June 2016.

[152] A. S. Mayer, W. Grosinger, J. Fellinger, G. Winkler, L. W. Perner, S. Droste, S. H. Salman, C. Li, C. M. Heyl, I. Hartl, and O. H. Heckl, "Flexible all-PM NALM Yb:fiber laser design for frequency comb applications: operation regimes and their noise properties," *Optics Express*, vol. 28, pp. 18946–18968, June 2020. Publisher: Optica Publishing Group.

[153] T. Udem, R. Holzwarth, and T. Hänsch, "Femtosecond optical frequency combs," *The European Physical Journal Special Topics*, vol. 172, pp. 69–79, June 2009.

[154] J. Kim and Y. Song, "Ultralow-noise mode-locked fiber lasers and frequency combs: principles, status, and applications," *Advances in Optics and Photonics*, vol. 8, pp. 465–540, Sept. 2016.

[155] D. Maas, A.-R. Bellancourt, B. Rudin, M. Golling, H. Unold, T. Südmeyer, and U. Keller, "Vertical integration of ultrafast semiconductor lasers," *Applied Physics B*, vol. 88, pp. 493–497, Sept. 2007.

[156] M. A. Gaafar, A. Rahimi-Iman, K. A. Fedorova, W. Stolz, E. U. Rafailov, and M. Koch, "Mode-locked semiconductor disk lasers," *Advances in Optics and Photonics*, vol. 8, pp. 370–400, Sept. 2016.

[157] A. Hugi, G. Villares, S. Blaser, H. C. Liu, and J. Faist, "Mid-infrared frequency comb based on a quantum cascade laser," *Nature*, vol. 492, pp. 229–233, Dec. 2012.

[158] J. Faist, G. Villares, G. Scalari, M. Rösch, C. Bonzon, A. Hugi, and M. Beck, "Quantum Cascade Laser Frequency Combs," *Nanophotonics*, vol. 5, pp. 272–291, June 2016.

[159] P. Del'Haye, A. Schliesser, O. Arcizet, T. Wilken, R. Holzwarth, and T. J. Kippenberg, "Optical frequency comb generation from a monolithic microresonator," *Nature*, vol. 450, pp. 1214–1217, Dec. 2007.

[160] A. L. Gaeta, M. Lipson, and T. J. Kippenberg, "Photonic-chip-based frequency combs," *Nature Photonics*, vol. 13, pp. 158–169, Mar. 2019.

[161] M. Kourogi, K. Nakagawa, and M. Ohtsu, "Wide-span optical frequency comb generator for accurate optical frequency difference measurement," *IEEE Journal of Quantum Electronics*, vol. 29, pp. 2693–2701, Oct. 1993.

[162] T. Kobayashi, T. Sueta, Y. Cho, and Y. Matsuo, "High-repetition-rate optical pulse generator using a Fabry-Perot electro-optic modulator," *Applied Physics Letters*, vol. 21, pp. 341–343, Oct. 1972.

[163] I. Morohashi, T. Sakamoto, H. Sotobayashi, T. Kawanishi, I. Hosako, and M. Tsuchiya, "Widely repetition-tunable 200 fs pulse source using a Mach–Zehnder-modulator-based flat comb generator and dispersion-flattened dispersion-decreasing fiber," *Optics Letters*, vol. 33, pp. 1192–1194, June 2008.

[164] A. Ishizawa, T. Nishikawa, A. Mizutori, H. Takara, H. Nakano, T. Sogawa, A. Takada, and M. Koga, "Generation of 120-fs laser pulses at 1-GHz repetition rate derived from continuous wave laser diode," *Optics Express*, vol. 19, pp. 22402–22409, Nov. 2011.

[165] A. J. Metcalf, V. Torres-Company, D. E. Leaird, and A. M. Weiner, "High-Power Broadly Tunable Electrooptic Frequency Comb Generator," *IEEE Journal of Selected Topics in Quantum Electronics*, vol. 19, pp. 231–236, Nov. 2013.

[166] F. Pockels, "Ueber den Einfluss elastischer Deformationen, speciell einseitigen Druckes, auf das optische Verhalten krystallinischer Körper," *Annalen der Physik*, vol. 273, no. 5, pp. 144–172, 1889.

[167] A. Parriaux, K. Hammani, and G. Millot, "Electro-optic frequency combs," *Advances in Optics and Photonics*, vol. 12, pp. 223–287, Mar. 2020.

[168] S. Nakano, K. Akiyama, and I. Shoji, "Accurate measurement of electro-optic coefficients of undoped and MgO-doped stoichiometric $LiNbO_3$," *Optical Materials Express*, vol. 7, pp. 939–944, Mar. 2017.

[169] R. S. Weis and T. K. Gaylord, "Lithium niobate: Summary of physical properties and crystal structure," *Applied Physics A*, vol. 37, pp. 191–203, Aug. 1985.

[170] V. Torres-Company and A. M. Weiner, "Optical frequency comb technology for ultra-broadband radio-frequency photonics," *Laser & Photonics Reviews*, vol. 8, no. 3, pp. 368–393, 2014.

[171] L. Zehnder, "Ein neuer Interferenzrefraktor," *Zeitschrift für Instrumentenkunde*, vol. 11, pp. 275–285, 1891.

[172] W. Steier, "A push-pull optical amplitude modulator," *IEEE Journal of Quantum Electronics*, vol. 3, pp. 664–667, Dec. 1967.

[173] M. Seimetz, *High-Order Modulation for Optical Fiber Transmission*, vol. 143. Berlin Heidelberg: Springer-Verlag, 2009.

[174] G. A. Korn and T. M. Korn, *Mathematical Handbook for Scientists and Engineers: Definitions, Theorems, and Formulas for Reference and Review*. Dover Publications, revised edition ed., June 2000.

[175] K. Beha, D. C. Cole, P. Del'Haye, A. Coillet, S. A. Diddams, and S. B. Papp, "Electronic synthesis of light," *Optica*, vol. 4, pp. 406–411, Apr. 2017.

[176] D. R. Carlson, D. D. Hickstein, W. Zhang, A. J. Metcalf, F. Quinlan, S. A. Diddams, and S. B. Papp, "Ultrafast electro-optic light with subcycle control," *Science*, vol. 361, pp. 1358–1363, Sept. 2018.

[177] J. Macario, P. Yao, S. Shi, A. Zablocki, C. Harrity, R. D. Martin, C. A. Schuetz, and D. W. Prather, "Full spectrum millimeter-wave modulation," *Optics Express*, vol. 20, pp. 23623–23629, Oct. 2012.

[178] C. Wang, M. Zhang, X. Chen, M. Bertrand, A. Shams-Ansari, S. Chandrasekhar, P. Winzer, and M. Lonar, "Integrated lithium niobate electro-optic modulators operating at CMOS-compatible voltages," *Nature*, vol. 562, pp. 101–104, Oct. 2018.

[179] D. Chen, H. R. Fetterman, A. Chen, W. H. Steier, L. R. Dalton, W. Wang, and Y. Shi, "Demonstration of 110 GHz electro-optic polymer modulators," *Applied Physics Letters*, vol. 70, pp. 3335–3337, June 1997.

[180] M. Lee, H. E. Katz, C. Erben, D. M. Gill, P. Gopalan, J. D. Heber, and D. J. McGee, "Broadband Modulation of Light by Using an Electro-Optic Polymer," *Science*, vol. 298, pp. 1401–1403, Nov. 2002.

[181] T. Sakamoto, T. Kawanishi, and M. Izutsu, "Widely wavelength-tunable ultra-flat frequency comb generation using conventional dual-drive Mach-Zehnder modulator," *Electronics Letters*, vol. 43, pp. 1039–1040, Sept. 2007.

[182] K. Qu, S. Zhao, X. Li, Z. Zhu, D. Liang, and D. Liang, "Ultra-Flat and Broadband Optical Frequency Comb Generator via a Single Mach–Zehnder Modulator," *IEEE Photonics Technology Letters*, vol. 29, pp. 255–258, Jan. 2017.

[183] M. Fujiwara, M. Teshima, J. Kani, H. Suzuki, N. Takachio, and K. Iwatsuki, "Optical carrier supply module using flattened optical multicarrier generation based on sinusoidal amplitude and phase hybrid modulation," *Journal of Lightwave Technology*, vol. 21, pp. 2705–2714, Nov. 2003.

[184] R. Wu, V. Torres-Company, D. E. Leaird, and A. M. Weiner, "Supercontinuum-based 10-GHz flat-topped optical frequency comb generation," *Optics Express*, vol. 21, pp. 6045–6052, Mar. 2013.

[185] A. Aubourg, J. Lhermite, S. Hocquet, E. Cormier, and G. Santarelli, "Generation of picosecond laser pulses at 1030nm with gigahertz range continuously tunable repetition rate," *Optics Letters*, vol. 40, pp. 5610–5613, Dec. 2015.

[186] K. Kashiwagi, T. Kurokawa, Y. Okuyama, T. Mori, Y. Tanaka, Y. Yamamoto, and M. Hirano, "Direct generation of 12.5-GHz-spaced optical frequency comb with ultrabroad coverage in near-infrared region by cascaded fiber configuration," *Optics Express*, vol. 24, pp. 8120–8131, Apr. 2016.

[187] K.-P. Ho and J. Kahn, "Optical frequency comb generator using phase modulation in amplified circulating loop," *IEEE Photonics Technology Letters*, vol. 5, pp. 721–725, June 1993.

[188] J. Kim, D. J. Richardson, and R. Slavík, "Cavity-induced phase noise suppression in a Fabry–Perot modulator-based optical frequency comb," *Optics Letters*, vol. 42, pp. 1536–1539, Apr. 2017.

[189] A. Rueda, F. Sedlmeir, M. Kumari, G. Leuchs, and H. G. L. Schwefel, "Resonant electro-optic frequency comb," *Nature*, vol. 568, pp. 378–381, Apr. 2019.

[190] M. Zhang, B. Buscaino, C. Wang, A. Shams-Ansari, C. Reimer, R. Zhu, J. M. Kahn, and M. Lonar, "Broadband electro-optic frequency comb generation in a lithium niobate microring resonator," *Nature*, vol. 568, pp. 373–377, Apr. 2019.

[191] I. El Mansouri, J. Fatome, C. Finot, M. Lintz, and S. Pitois, "All-Fibered High-Quality Stable 20- and 40-GHz Picosecond Pulse Generators for 160-Gb/s OTDM Applications," *IEEE Photonics Technology Letters*, vol. 23, pp. 1487–1489, Oct. 2011.

[192] T. Sakamoto and A. Chiba, "Multiple-frequency-spaced flat optical comb generation using a multiple-parallel phase modulator," *Optics Letters*, vol. 42, pp. 4462–4465, Nov. 2017.

[193] T. Yasui, Y. Kabetani, E. Saneyoshi, S. Yokoyama, and T. Araki, "Terahertz frequency comb by multifrequency-heterodyning photoconductive detection for high-accuracy, high-resolution terahertz spectroscopy," *Applied Physics Letters*, vol. 88, p. 241104, June 2006.

[194] K.-L. Yeh, M. C. Hoffmann, J. Hebling, and K. A. Nelson, "Generation of 10J ultrashort terahertz pulses by optical rectification," *Applied Physics Letters*, vol. 90, p. 171121, Apr. 2007.

[195] N. T. Yardimci, S.-H. Yang, C. W. Berry, and M. Jarrahi, "High-Power Terahertz Generation Using Large-Area Plasmonic Photoconductive Emitters," *IEEE Transactions on Terahertz Science and Technology*, vol. 5, pp. 223–229, Mar. 2015.

[196] D. Burghoff, T.-Y. Kao, N. Han, C. W. I. Chan, X. Cai, Y. Yang, D. J. Hayton, J.-R. Gao, J. L. Reno, and Q. Hu, "Terahertz laser frequency combs," *Nature Photonics*, vol. 8, pp. 462–467, June 2014.

[197] M. Jaidl, N. Opacak, M. A. Kainz, S. Schönhuber, D. Theiner, B. Limbacher, M. Beiser, M. Giparakis, A. M. Andrews, G. Strasser, B. Schwarz, J. Darmo, and K. Unterrainer, "Comb operation in terahertz quantum cascade ring lasers," *Optica*, vol. 8, pp. 780–787, June 2021.

[198] M. Rösch, M. Beck, M. J. Süess, D. Bachmann, K. Unterrainer, J. Faist, and G. Scalari, "Heterogeneous terahertz quantum cascade lasers exceeding 1.9 THz spectral bandwidth and featuring dual comb operation," *Nanophotonics*, vol. 7, pp. 237–242, Jan. 2018.

[199] T. Hiraoka, Y. Inose, T. Arikawa, H. Ito, and K. Tanaka, "Passive mode-locking and terahertz frequency comb generation in resonant-tunneling-diode oscillator," *Nature Communications*, vol. 13, p. 3740, June 2022.

[200] C. Wang, B. Perkins, Z. Wang, and R. Han, "Molecular Detection for Unconcentrated Gas With ppm Sensitivity Using 220-to-320-GHz Dual-Frequency-Comb Spectrometer in CMOS," *IEEE Transactions on Biomedical Circuits and Systems*, vol. 12, pp. 709–721, June 2018.

[201] M. M. Assefzadeh and A. Babakhani, "Broadband Oscillator-Free THz Pulse Generation and Radiation Based on Direct Digital-to-Impulse Architecture," *IEEE Journal of Solid-State Circuits*, vol. 52, pp. 2905–2919, Nov. 2017.

[202] S. Tammaro, O. Pirali, P. Roy, J.-F. Lampin, G. Ducournau, A. Cuisset, F. Hindle, and G. Mouret, "High density terahertz frequency comb produced by coherent synchrotron radiation," *Nature Communications*, vol. 6, p. 7733, July 2015.

[203] A. Ishizawa, T. Nishikawa, A. Mizutori, H. Takara, A. Takada, T. Sogawa, and M. Koga, "Phase-noise characteristics of a 25-GHz-spaced optical frequency comb based on a phase- and intensity-modulated laser," *Optics Express*, vol. 21, pp. 29186–29194, Dec. 2013.

[204] T. Okoshi, K. Kikuchi, and A. Nakayama, "Novel method for high resolution measurement of laser output spectrum," *Electronics Letters*, vol. 16, pp. 630–631, July 1980.

[205] N. B. Hébert, V. Michaud-Belleau, J. D. Anstie, J.-D. Deschênes, A. N. Luiten, and J. Genest, "Self-heterodyne interference spectroscopy using a comb generated by pseudo-random modulation," *Optics Express*, vol. 23, pp. 27806–27818, Oct. 2015.

[206] D. A. Long, A. J. Fleisher, D. F. Plusquellic, and J. T. Hodges, "Multiplexed sub-Doppler spectroscopy with an optical frequency comb," *Physical Review A*, vol. 94, p. 061801, Dec. 2016.

[207] T. Göbel, D. Stanze, B. Globisch, R. J. B. Dietz, H. Roehle, and M. Schell, "Telecom technology based continuous wave terahertz photomixing system with 105 decibel signal-to-noise ratio and 3.5 terahertz bandwidth," *Optics Letters*, vol. 38, pp. 4197–4199, Oct. 2013.

[208] A. S. Pine, R. D. Suenram, E. R. Brown, and K. A. McIntosh, "A Terahertz Photomixing Spectrometer: Application to SO2Self Broadening," *Journal of Molecular Spectroscopy*, vol. 175, pp. 37–47, Jan. 1996.

[209] R. W. P. Drever, J. L. Hall, F. V. Kowalski, J. Hough, G. M. Ford, A. J. Munley, and H. Ward, "Laser phase and frequency stabilization using an optical resonator," *Applied Physics B*, vol. 31, pp. 97–105, June 1983.

[210] G. Mouret, F. Hindle, A. Cuisset, C. Yang, R. Bocquet, M. Lours, and D. Rovera, "THz photomixing synthesizer based on a fiber frequency comb," *Optics Express*, vol. 17, p. 22031, Nov. 2009.

[211] T. Yasui, H. Takahashi, K. Kawamoto, Y. Iwamoto, K. Arai, T. Araki, H. Inaba, and K. Minoshima, "Widely and continuously tunable terahertz synthesizer traceable to a microwave frequency standard," *Optics Express*, vol. 19, p. 4428, Feb. 2011.

[212] R. Montgomery and R. DeSalvo, "A novel technique for double sideband suppressed carrier modulation of optical fields," *IEEE Photonics Technology Letters*, vol. 7, pp. 434–436, Apr. 1995.

[213] B. Jerez, F. Walla, A. Betancur, P. Martín-Mateos, C. de Dios, and P. Acedo, "Electro-optic THz dual-comb architecture for high-resolution, absolute spectroscopy," *Optics Letters*, vol. 44, p. 415, Jan. 2019.

[214] F. S. Vieira, F. C. Cruz, D. F. Plusquellic, and S. A. Diddams, "Tunable resolution terahertz dual frequency comb spectrometer," *Optics Express*, vol. 24, p. 30100, Dec. 2016.

[215] I. L. Gheorma and G. K. Gopalakrishnan, "Flat Frequency Comb Generation With an Integrated Dual-Parallel Modulator," *IEEE Photonics Technology Letters*, vol. 19, pp. 1011–1013, July 2007.

[216] X. Chen, S. Chandrasekhar, P. Winzer, P. Pupalaikis, I. Ashiq, A. Khanna, A. Steffan, and A. Umbach, "180-GBaud Nyquist Shaped Optical QPSK Generation Based on a 240-GSa/s 100-GHz Analog Bandwidth DAC," in *Asia Communications and Photonics Conference 2016, paper AS4A.1*, Nov. 2016.

[217] G. Raybon, A. Adamiecki, J. Cho, F. Jorge, A. Konczykowska, M. Riet, B. Duval, J.-Y. Dupuy, N. Fontaine, P. J. Winzer, S. Chandrasekhar, and X. Chen, "180-GBaud All-ETDM Single-Carrier Polarization Multiplexed QPSK Transmission over 4480 km," in *Optical Fiber Communication Conference, paper Th4C.3*, Mar. 2018.

[218] A. D. Gomes, H. Bartelt, and O. Frazão, "Optical Vernier Effect: Recent Advances and Developments," *Laser & Photonics Reviews*, vol. 15, no. 7, p. 2000588, 2021.

[219] P. Martín-Mateos, D. ibiraitė Lukenskienė, R. Barreiro, C. de Dios, A. Lisauskas, V. Krozer, and P. Acedo, "Hyperspectral terahertz imaging with electro-optic dual combs and a FET-based detector," *Scientific Reports*, vol. 10, p. 14429, Dec. 2020.

[220] F. L. Constantin, "Electrically-driven heterodyne detection of a multifrequency THz-wave with a photomixer," in *Terahertz, RF, Millimeter, and Submillimeter-Wave Technology and Applications XIV*, (Online Only, United States), p. 60, Mar. 2021.

[221] M. Rösch, G. Scalari, M. Beck, and J. Faist, "Octave-spanning semiconductor laser," *Nature Photonics*, vol. 9, pp. 42–47, Jan. 2015.

[222] H. Li, Z. Li, W. Wan, K. Zhou, X. Liao, S. Yang, C. Wang, J. C. Cao, and H. Zeng, "Toward Compact and Real-Time Terahertz Dual-Comb Spectroscopy Employing a Self-Detection Scheme," *ACS Photonics*, vol. 7, pp. 49–56, Jan. 2020.

[223] J. D. Cruzan, M. R. Viant, M. G. Brown, D. D. Lucas, K. Liu, and R. J. Saykally, "Terahertz laser vibration–rotation–tunneling spectrum of the water pentamer–d10.: Constraints on the bifurcation tunneling dynamics," *Chemical Physics Letters*, vol. 292, pp. 667–676, Aug. 1998.

[224] C. Hepp, S. Luttjohann, A. Roggenbuck, A. Deninger, S. Nellen, T. Gobel, M. Jorger, and R. Harig, "A cw-terahertz gas analysis system with ppm detection limits," 2016.

[225] N. Rothbart, K. Schmalz, and H.-W. Hübers, "A Compact Circular Multipass Cell for Millimeter-Wave/Terahertz Gas Spectroscopy," *IEEE Transactions on Terahertz Science and Technology*, vol. 10, pp. 9–14, Jan. 2020.

[226] F. Hindle, R. Bocquet, A. Pienkina, A. Cuisset, and G. Mouret, "Terahertz gas phase spectroscopy using a high-finesse Fabry–Pérot cavity," *Optica*, vol. 6, pp. 1449–1454, Dec. 2019.

[227] M. S. Islam, C. M. B. Cordeiro, M. A. R. Franco, J. Sultana, A. L. S. Cruz, and D. Abbott, "Terahertz optical fibers," *Optics Express*, vol. 28, pp. 16089–16117, May 2020.

[228] S. Atakaramians, S. A. V, T. M. Monro, and D. Abbott, "Terahertz dielectric waveguides," *Advances in Optics and Photonics*, vol. 5, pp. 169–215, June 2013.

[229] B. You, T.-A. Liu, J.-L. Peng, C.-L. Pan, and J.-Y. Lu, "A terahertz plastic wire based evanescent field sensor for high sensitivity liquid detection," *Optics Express*, vol. 17, pp. 20675–20683, Nov. 2009.

[230] M. S. Islam, J. Sultana, K. Ahmed, M. R. Islam, A. Dinovitser, B. W.-H. Ng, and D. Abbott, "A Novel Approach for Spectroscopic Chemical Identification Using Photonic Crystal Fiber in the Terahertz Regime," *IEEE Sensors Journal*, vol. 18, pp. 575–582, Jan. 2018.

[231] J. Sultana, M. S. Islam, K. Ahmed, A. Dinovitser, B. W.-H. Ng, and D. Abbott, "Terahertz detection of alcohol using a photonic crystal fiber sensor," *Applied Optics*, vol. 57, pp. 2426–2433, Apr. 2018.

[232] A. L. S. Cruz, C. M. B. Cordeiro, and M. A. R. Franco, "3D Printed Hollow-Core Terahertz Fibers," *Fibers*, vol. 6, p. 43, Sept. 2018.

[233] A. Wilk, J. C. Carter, M. Chrisp, A. M. Manuel, P. Mirkarimi, J. B. Alameda, and B. Mizaikoff, "Substrate-Integrated Hollow Waveguides: A New Level of Integration in Mid-Infrared Gas Sensing," *Analytical Chemistry*, vol. 85, pp. 11205–11210, Dec. 2013.

[234] J. F. d. S. Petruci, P. Regina Fortes, V. Kokoric, A. Wilk, I. Milton Raimundo, A. Alves Cardoso, and B. Mizaikoff, "Monitoring of hydrogen sulfide via substrate-integrated hollow waveguide mid-infrared sensors in real-time," *Analyst*, vol. 139, no. 1, pp. 198–203, 2014.

[235] I. J. G. d. Silva, E. Tütüncü, M. Nägele, P. Fuchs, M. Fischer, I. M. Raimundo, and B. Mizaikoff, "Sensing hydrocarbons with interband cascade lasers and substrate-integrated hollow waveguides," *Analyst*, vol. 141, pp. 4432–4437, July 2016.

[236] J. Glöckler, C. Jaeschke, Y. Kocaöz, V. Kokoric, E. Tütüncü, J. Mitrovics, and B. Mizaikoff, "iHWG-MOX: A Hybrid Breath Analysis System via the Combination of Substrate-Integrated Hollow Waveguide Infrared Spectroscopy with Metal Oxide Gas Sensors," *ACS Sensors*, vol. 5, pp. 1033–1039, Apr. 2020.

[237] D. N. Barreto, W. R. Silva, B. Mizaikoff, and J. F. da Silveira Petruci, "Monitoring Ozone Using Portable Substrate-Integrated Hollow Waveguide-Based Absorbance Sensors in the Ultraviolet Range," *ACS Measurement Science Au*, vol. 2, pp. 39–45, Feb. 2022.

[238] D. N. Barreto, V. Kokoric, J. F. da Silveira Petruci, and B. Mizaikoff, "From Light Pipes to Substrate-Integrated Hollow Waveguides for Gas Sensing: A Review," *ACS Measurement Science Au*, vol. 1, pp. 97–109, Dec. 2021.

[239] M. Graf, L. Emmenegger, and B. Tuzson, "Compact, circular, and optically stable multi-pass cell for mobile laser absorption spectroscopy," *Optics Letters*, vol. 43, pp. 2434–2437, June 2018.

[240] S. L. Gilbert, W. C. Swann, and C.-M. Wang, "Hydrogen Cyanide H13C14N Absorption Reference for 1530 nm to 1560 nm Wavelength Calibration SRM 2519," *NIST*, pp. 37–38, Nov. 1998.

[241] G. C. Bjorklund, "Frequency-modulation spectroscopy: a new method for measuring weak absorptions and dispersions," *Optics Letters*, vol. 5, pp. 15–17, Jan. 1980.

[242] R. Eichholz, H. Richter, M. Wienold, L. Schrottke, R. Hey, H. T. Grahn, and H.-W. Hübers, "Frequency modulation spectroscopy with a THz quantum-cascade laser," *Optics Express*, vol. 21, pp. 32199–32206, Dec. 2013.

[243] I. A. Ratiu, T. Ligor, V. Bocos-Bintintan, C. A. Mayhew, and B. Buszewski, "Volatile Organic Compounds in Exhaled Breath as Fingerprints of Lung Cancer, Asthma and COPD," *Journal of Clinical Medicine*, vol. 10, p. 32, Jan. 2021.

Publications

Peer Reviewed Publications

D. Theiner, B. Limbacher, M. Jaidl, M. Ertl, M. Hlavatsch, K. Unterrainer, B. Mizaikoff, and J. Darmo, "Flexible terahertz gas sensing platform based on substrate-integrated hollow waveguides and an opto-electronic light source," *Optics Express*, vol. 31, pp. 15983–15993, May 2023. Publisher: Optica Publishing Group.

M. Jaidl, M. Beiser, M. Giparakis, M. A. Kainz, D. Theiner, B. Limbacher, M. C. Ertl, A. M. Andrews, G. Strasser, J. Darmo, and K. Unterrainer, "Ultrabroadband Heterogeneous THz Quantum Cascade Laser," *ACS Photonics*, vol. 10, pp. 111–115, Jan. 2023. Publisher: American Chemical Society.

M. Jaidl, N. Opacak, M. A. Kainz, D. Theiner, B. Limbacher, M. Beiser, M. Giparakis, A. M. Andrews, G. Strasser, B. Schwarz, J. Darmo, and K. Unterrainer, "Silicon integrated terahertz quantum cascade ring laser frequency comb," *Applied Physics Letters*, vol. 120, p. 091106, Feb. 2022. Publisher: American Institute of Physics.

D. Theiner, B. Limbacher, M. Jaidl, K. Unterrainer, and J. Darmo, "Flexible terahertz opto-electronic frequency comb light source tunable over 3.5 THz," *Optics Letters*, vol. 46, pp. 5715–5718, Nov. 2021. Publisher: Optica Publishing Group.

M. Jaidl, N. Opacak, M. A. Kainz, S. Schönhuber, D. Theiner, B. Limbacher, M. Beiser, M. Giparakis, A. M. Andrews, G. Strasser, B. Schwarz, J. Darmo, and K. Unterrainer, "Comb operation in terahertz quantum cascade ring lasers," *Optica*, vol. 8, pp. 780–787, June 2021. Publisher: Optica Publishing Group.

W. Steiger, P. Gruber, D. Theiner, A. Dobos, M. Lunzer, J. V. Hoorick, S. V. Vlierberghe, R. Liska, and A. Ovsianikov, "Fully automated z-scan setup based on a tunable fs-oscillator," *Optical Materials Express*, vol. 9, pp. 3567–3581, Sept. 2019. Publisher: Optica Publishing Group.

A. Dobos, W. Steiger, D. Theiner, P. Gruber, M. Lunzer, J. V. Hoorick, S. V. Vlierberghe, and A. Ovsianikov, "Screening of two-photon activated photodynamic therapy sensitizers using a 3D osteosarcoma model," *Analyst*, vol. 144, no. 9, pp. 3056–3063, 2019. Publisher: Royal Society of Chemistry.

Conference Contributions

M. Jaidl, N. Opacak, M. A. Kainz, M. Ertl, D. Theiner, B. Limbacher, M. Beiser, M. Giparakis, M. A. Andrews, G. Strasser, B. Schwarz, J. Darmo, and K. Unterrainer, "Terahertz quantum cascade ring lasers: comb operation and integration on Si-substrates," in *Novel In-Plane Semiconductor Lasers XXII*, vol. PC12440, p. PC124400Q, SPIE, Mar. 2023.

D. Theiner, B. Limbacher, M. Jaidl, M. Ertl, Marie Christine, K. Unterrainer, and J. Darmo, "Tailored Terahertz Frequency Combs for Molecular Sensing," (Mauerndorf, Austria), Feb. 2023.

M. Jaidl, M. Beiser, M. Giparakis, M. A. Kainz, D. Theiner, B. Limbacher, M. C. Ertl, A. M. Andrews, G. Strasser, J. Darmo, and K. Unterrainer, "Ultra-Broadband Heterogeneous Terahertz Quantum Cascade Laser," (Mauerndorf, Austria), Feb. 2023.

D. Theiner, B. Limbacher, K. Unterrainer, and J. Darmo, "Synthetized Terahertz Frequency Combs," in *2021 Conference on Lasers and Electro-Optics Europe and European Quantum Electronics Conference (2021), paper cc_8_4*, p. cc_8_4, Optica Publishing Group, June 2021.

M. A. Kainz, M. Jaidl, B. Limbacher, D. Theiner, M. Giparakis, M. Beiser, A. M. Andrews, G. Strasser, and K. Unterrainer, "Terahertz Amplifier with Optical Threshold," in *2021 Conference on Lasers and Electro-Optics Europe and European Quantum Electronics Conference (2021), paper cc_6_5*, p. cc_6_5, Optica Publishing Group, June 2021.

D. Theiner, B. Limbacher, M. Jaidl, K. Unterrainer, and J. Darmo, "Terahertz Frequency Comb Toolbox for Molecular Sensing," in *2022 47th International Conference on Infrared, Millimeter and Terahertz Waves (IRMMW-THz)*, pp. 1–2, Aug. 2022. ISSN: 2162-2035.

M. A. Kainz, M. Jaidl, B. Limbacher, D. Theiner, M. Giparakis, M. Beiser, A. M. Andrews, G. Strasser, and K. Unterrainer, "Terahertz Quantum Cascade Amplifier with Optical Threshold," in *Conference on Lasers and Electro-Optics (2021), paper ATu2T.5*, p. ATu2T.5, Optica Publishing Group, May 2021.

M. C. Ertl, M. Jaidl, B. Limbacher, D. Theiner, M. Giparakis, M. Beiser, A. M. Andrews, G. Strasser, J. Darmo, and K. Unterrainer, "Episide down bonded terahertz quantum cascade wire laser," (Zürich, Monte Verita, Swizerland), Aug. 2022.

D. Theiner, B. Limbacher, M. Jaidl, K. Unterrainer, and J. Darmo, "Tailoring Terahertz Frequency Combs for Molecular Sensing," (Budapest, Hungary), June 2022.

D. Theiner, B. Limbacher, M. Jaidl, K. Unterrainer, and J. Darmo, "Agile Terahertz Frequency Comb Source for Room Temperature Applications," (Kaiserslautern, Germany), May 2022.

M. Jaidl, D. Theiner, B. Limbacher, M. Beiser, A. M. Andrews, G. Strasser, J. Darmo, and K. Unterrainer, "QCL and fibre laser-driven frequency combs," (Strasbourg, France), Apr. 2022.

M. Jaidl, N. Opacak, M. A. Kainz, S. Schönhuber, D. Theiner, B. Limbacher, M. Beiser, M. Giparakis, A. M. Andrews, G. Strasser, B. Schwarz, J. Darmo, and K. Unterrainer, "Comb Formation In Ultrathin Terahertz Quantum Cascade Ring Lasers," in *Conference on Lasers and Electro-Optics (2021), paper JTh3A.78*, p. JTh3A.78, Optica Publishing Group, May 2021.

D. Theiner, B. Limbacher, K. Unterrainer, and J. Darmo, "Designer Terahertz Frequency Comb Generation," in *2021 Conference on Lasers and Electro-Optics (CLEO)*, pp. 1–2, May 2021. ISSN: 2160-8989.

M. C. Ertl, M. Jaidl, M. A. Kainz, B. Limbacher, D. Theiner, M. Beiser, M. Giparakis, A. M. Andrews, G. Strasser, J. Darmo, and K. Unterrainer, "Epi-down Bonded Quantum Cascade Patch Antenna Array Laser," (Austria), p. 137, Swiss Physical Society, 2021. INIS Reference Number: 53064788.

D. Theiner, B. Limbacher, J. Darmo, M. Jaidl, and K. Unterrainer, "Shaping terahertz frequency combs at room temperature: photomixing reloaded," (Austria), p. 137, Swiss Physical Society, 2021. INIS Reference Number: 53064793.

C. G. Derntl, D. Theiner, M. Beck, G. Scalari, J. Faist, K. Unterrainer, and J. Darmo, "Gain Competition in a Terahertz Quantum Cascade Laser," Sept. 2020.

M. Jaidl, M. A. Kainz, S. Schönhuber, D. Theiner, A. M. Andrews, M. Beiser, G. Strasser, J. Darmo, and K. Unterrainer, "Multi-mode emission from a THz Quantum Cascade Ring Laser," (Mauerndorf, Austria), Feb. 2020.

C. G. Derntl, D. Theiner, G. Scalari, M. Beck, J. Faist, K. Unterrainer, and J. Darmo, "Spectrally Resolved Gain Dynamics in Heterogeneous Terahertz Quantum Cascade Lasers," (Mauterndorf, Austria), Feb. 2020.

M. A. Kainz, M. Jaidl, S. Schönhuber, D. Theiner, M. P. Semtsiv, S. Kurlov, W. T. Masselink, M. Beiser, M. Giparakis, H. Detz, G. Strasser, K. Unterrainer, and A. M. Andrews, "Thermoelectrically Cooled THz Quantum Cascade Lasers," (Mauterndorf, Austria), pp. 1–2, Feb. 2020.

C. G. Derntl, D. Theiner, G. Scalari, M. Beck, J. Faist, K. Unterrainer, and J. Darmo, "Gain dynamics in THz QCLs and its implication for THz comb sources," in *2019 44th International Conference on Infrared, Millimeter, and Terahertz Waves (IRMMW-THz)*, pp. 1–2, Sept. 2019. ISSN: 2162-2035.

M. A. Kainz, A. M. Andrews, S. Schönhuber, B. Limbacher, M. Jaidl, D. Theiner, H. Detz, G. Strasser, G. Bastard, and K. Unterrainer, "Mode Switching of a Dual-color Terahertz Quantum Cascade Laser," (Ojai, California, USA), pp. 20–21, Sept. 2019.

S. Schönhuber, B. Limbacher, M. A. Kainz, D. Theiner, M. Jaidl, A. M. Andrews, H. Detz, G. Strasser, J. Darmo, and K. Unterrainer, "Optical Tuning of Terahertz Quantum Cascade Random Lasers," (Ojai, California, USA), pp. 250–251, Sept. 2019.

C. G. Derntl, D. Theiner, G. Scalari, M. Beck, J. Faist, K. Unterrainer, and J. Darmo, "Spectrally resolved gain dynamics in THz quantum cascade lasers," (Ojai, California, USA), pp. 30–31, Sept. 2019.

J. Darmo, G. Derntl, D. Theiner, G. Scalari, M. Beck, J. Faist, and K. Unterrainer, "Time and spectrally resolved gain dynamics in THz quantum cascade lasers," (Prague, Czech republic), pp. 197–197, Sept. 2019.

S. Schönhuber, B. Limbacher, M. A. Kainz, D. Theiner, M. Jaidl, A. M. Andrews, H. Detz, G. Strasser, J. Darmo, and K. Unterrainer, "Optical Control of Terahertz Quantum Cascade Random Lasers," (Mauterndorf, Austria), Feb. 2018.

D. Theiner, S. Schönhuber, M. A. Kainz, B. Limbacher, A. M. Andrews, H. Detz, G. Strasser, and K. Unterrainer, "Three-Dimensional Terahertz Tomography using Quantum Cascade Lasers," (Mauterndorf, Austria), pp. 124–125, Feb. 2018.